Title	Fano effect in double quantum dot and single electron dynamics studied with radio frequency
Author(s)	則元, 将太
Citation	大阪大学, 2019, 博士論文
Version Type	VoR
URL	https://doi.org/10.18910/72643
rights	
Note	

Fano effect in double quantum dot and single electron dynamics studied with radio frequency

Shota Norimoto

Depertment of Physics, Graduate School of Science, Osaka University

February 21, 2019

Contents

Preface

Our research objects, mesoscopic systems, are small conductors whose dimensions are intermediate between a microscopic system like atoms and a macroscopic system like bulk materials. The mesocopic systems allow us to observe various quantum phenomenon and interactions, and it is possible to control them. Especially, two dimensional electron gas (2DEG) formed at heterojunction of GaAs and AlGaAs has high controllability by using Schottky gate electrodes on the substrate. Local trapping of electrons by the Schottky gates is called quantum dot (QD), which enables us to study the transport in a single discrete level and to manipulate a single electron. The transport of mesoscopic system is measured by conventional conductance measurement based on highly evolved electronics. Thanks to them, high-speed measurement by radio frequency (RF) is available. The combination of the single electron manipulation and high-speed measurement by RF makes it possible to measure the single electron propagation through the single discrete level. Our purpose is to study dynamics in mesoscopic system with a fundamental idea of transmission and reflection of the single electron, where we investigate the non-equilibrium regime of quantum system. Our works serves to establish fundamental technique to study frontier of physics.

The Thesis consists of six Chapters. Chapter 1 gives the basic ideas to understand this thesis. Actual process to fabricate the mesocopic system is shown in Chapter 2. It takes long time for me to establish the fabrication techniques written in this Chapter. The measurement results of the devices fabricated in this Chapter are shown in Chapter 5. Chapter 3 explains observation of one conventional interference effect "Fano effct" in the transport of a lateral series of QDs "double quantum dot (DQD)". This Chapter is based on my paper published in *Physical Review B* [1]. In Chapter 4, the technique to detect that the number of electron in DQD with single electron charge detector (SECD) and how to realize the DQD are shown. Chapter 5 shows the techniques to work single electron sources and the ideas to understand how they work. We summarize the Thesis in Chapter 6

1 Introduction

In this Chapter, we explain three topics to understand our research. Essential information on them are introduced here. Concrete ideas and objects are given in each chapter. First, we introduce the transport phenomena in the mesoscopic system. Next, we explain how an electric current standard is important and the single electron sources to realize it. Finally, we discuss the dynamics of electrons which can be studied by the single electron sources. The latter two topics are the main motivation of the present thesis.

1.1 Mesoscopic system

The electric property is the way to study the mesoscopic system. Here, we review the transport in the macroscopic system to clarify the differences in transport in the mesoscopic system[2, 3]. The electric property of materials is characterized by the conductance G which is defined by the applied voltage V and the current I as follows.

$$G = I/V. \tag{1.1}$$

G is described by the geometry of the macroscopic material, namely the cross-sectional area S, the length L, and the material-specific conductivity σ as

$$G = \sigma \frac{S}{L}. \tag{1.2}$$

This formula can be derived by microscopic aspect based on quantum physics. Landauer formula represents the transport in the material as the scattering problem of the conduction electrons. Figure 1.1 shows the system which is considered in Landauer formula and examples of the system. It is assumed that the system is connected with leads which transmit electron perfectly. The left and right sides of Fig. 1.1 (a) show the distributions of electrons in leads. Due to the temperature, the Fermi level has the energy width of $k_B T$, where k_B is Boltzmann constant. The center in Fig. 1.1 (a) shows that electrons in transverse mode a in left lead move in unoccupied transverse mode b in the right lead. For a finite size conductor connected to ideal leads, the Landauer formula,

$$G = s \frac{e^2}{h} \Sigma_{a,b} T_{ab} \tag{1.3}$$

relates the conductance G to the sum of the transmission coefficient T_{ab} through the system, where s, e, and h are degeneracy freedom of spin, elementary charge, and Planck constant, respectively. The large conductance of normal metal is understood by its many channels due to the large Fermi wave vector k_F. If there is no transition among different modes during

(a)

E

$k_B T$ Transverse mode a   Transverse mode b

E_f

System

Density of States   Density of States

E

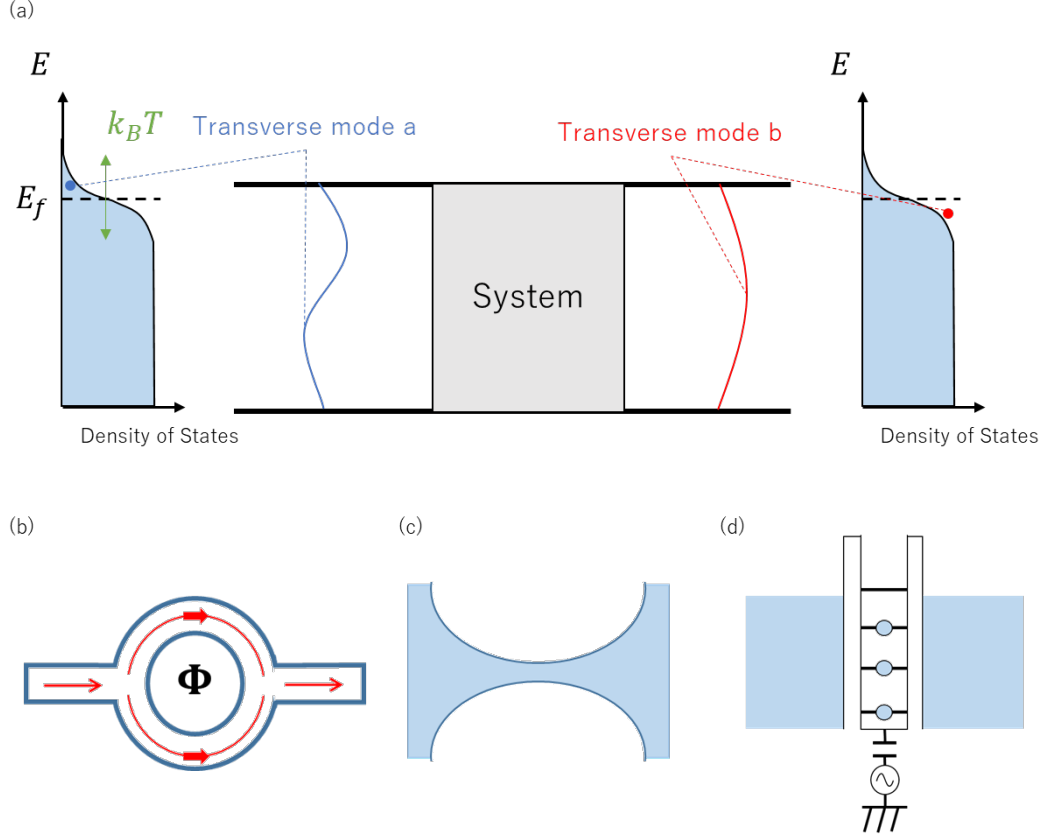(b)   (c)   (d)

Φ

Figure 1.1: (a) Schematics of the situation to which Landauer formula can be applied. The system is connected with ideal leads which transmit electrons perfectly. The electron in the left lead which belongs to transverse mode a moves in unoccupied mode b through the system at temperature T. (b)-(d) Examples of mesoscopic system (b) Aharonov-Bohm ring. (c) Narrow conductor where a few transverse modes can exist. (d) Discrete levels in a potential well.

propagation through the system, Eq. (1.3) can be simplified with channel-index n.

$$G = s\frac{e^2}{h}\Sigma_n T_n \tag{1.4}$$

The Landauer formula might be useless for bulk material, but it is convenient for explanation of the system which has only a few conductance channels. Aharanov-Bohm (AB) ring is a good example to see the benefit of the Landauer formula.

Figure 1.2 shows the magnetoresistance of the AB ring whose diameter and width are $784\,\mathrm{nm}$ and $41\,\mathrm{nm}$ [4]. The oscillation of the resistance is observed as a function of the magnetic field (H) (Fig. 1.2 (a)), which comes from Aharanov-Bohm effect[5]. This oscillation is called AB oscillation. Aharanov and Bohm considered the system which has two paths for electrons to propagate and magnetic flux inside of the two paths by quantum mechanics. They proved that the transmission probability of electron oscillates as a function of the magnetic flux which penetrates the area enclosed by the two paths. The oscillation of Fig. 1.2 clearly proved the validity of this idea by observation of electron interference. The important points of the observation of this interference are
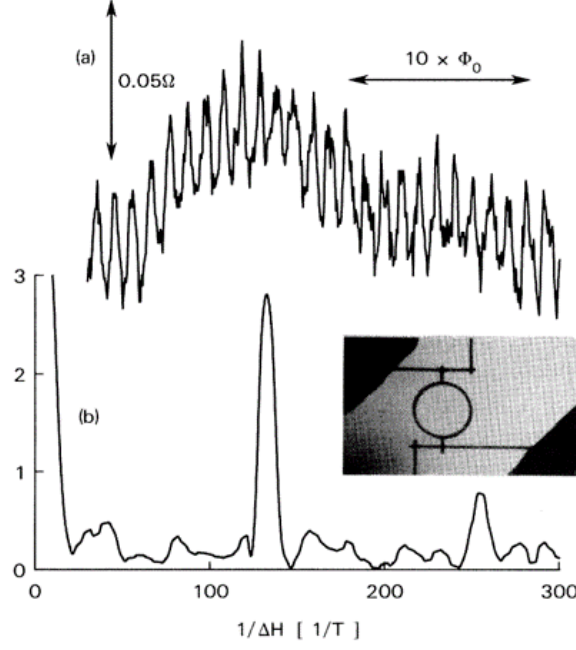
Figure 1.2: (a) Magnetoresistance of the AB ring shown in the inset at $10\,\text{mK}$. (b) Fourier power spectrum of the magnetoresistance. Peaks at h/e (around $1/\Delta H = 130\,\text{T}^{-1}$) and $h/2e$ (around $1/\Delta H = 260\,\text{T}^{-1}$) are observed. This figure is taken from Ref. [4].

- The system is smaller than the coherent length l_ϕ where conduction electrons keep the quantum coherence

- The system is smaller than the thermal length l_T of electrons coming from the energy distribution of the conduction electrons.

Therefore it is essential to fabricate a very small device and to cool the device down. Such small devices are called as "mesoscopic system" to express intermediate length scale between macroscopic system of bulk and microscopic system of an atom, electron, etc.. They are fabricated by lithography technique which has been developed by semiconductor industries. Actual processes to fabricate devices are shown in the next chapter "Nano-fabrication".

Next, let us explain how important temperature is. Figure 1.3 shows the temperature effect on the transport in the mesoscopic system.

First, transport in the AB ring is explained. At finite temperature, the Fermi surface has a width of $k_B T$ (Fig. 1.3 (a)). Therefore the electrons around $k_B T$ of E_F transmit the system, AB ring. Since wavelength of electrons depend on the energy, the result of interference depends on their energy. As shown in Eq. (1.4), the conductance is a summation of the various channels. Broaden Fermi surface due to temperature smears the AB oscillation (Left side of Fig. 1.3 (a) is an exaggerated cartoon.). This is one reason that measurement in mesoscopic system requires low temperature.
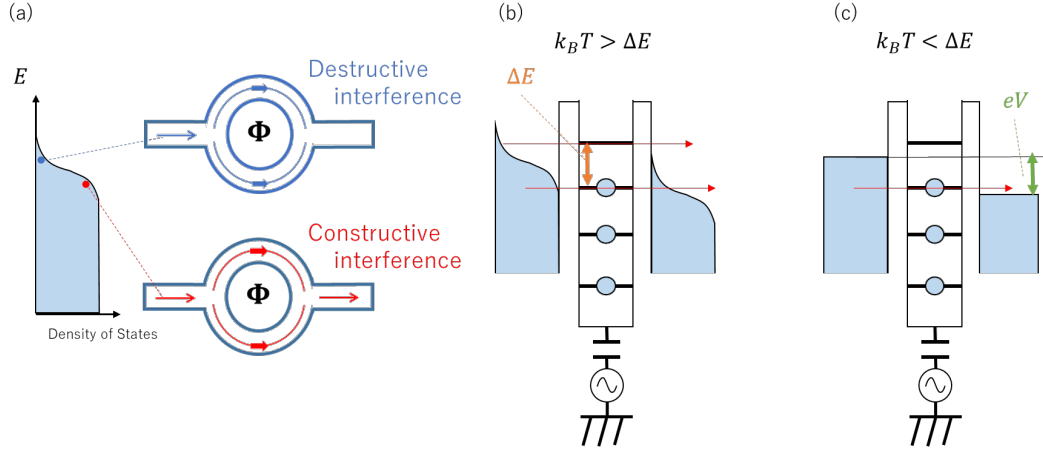
Figure 1.3: (a) Schematic figure of the transport in an AB ring. Blue means high energy electron, which causes destructive interference in the AB ring. Red means low energy electron, which causes constructive interference in the AB ring. (b) Transmission of the electrons at high temperature. (c) Transmission of the electrons at low temperature.

Second, the transport through the discrete levels (Figs. 1.3 (b) and (c)) is considered. As far as adiabatic transport is considered, the electrons whose energy is the same to discrete levels can transmit. When the temperature is larger than the energy separation of ΔE, the electrons can propagate several levels. In such a case, it is impossible to observe the transmission of a single discrete level. On the other hand, when the temperature is smaller than ΔE, the electrons propagate only the single discrete level. In this case, it is possible to observe the transport of the single discrete level and fix the number of electron in the well. The sample cooling is achieved by dilution refrigerator which reaches 10 mK over a year.

One of the main experimental platforms of mesoscopic system is two dimensional-electron gas system (2DEG) formed at heterogeneity of GaAs and AlGaAs which has high controllability with negative gate voltage. 2DEG and nano-fabrication techniques yield the mesoscopic system shown in Figs. 1.1 (c) and (d), a one-dimensional conductor which is called quantum point contact(QPC) and a single discrete level which is called quantum dot (QD). They are formed by the gate voltage control.

The advantage of studying electrons in condensed matter lies in the fact they have rich interactions. Kondo effect occurs in QD when the QD is in special condition[6, 7, 8]. Kondo effect is one of the typical quantum many-body effects, which contributes to the transport[9]. Kondo effect was first observed in nonmagnetic metal which contains magnetic impurities[10]. The localized spins of the magnetic impurities and the electrons on the Fermi surface make unique quantum many-body states so-called Kondo clouds. In the metals, Kondo clouds randomize the direction of conduction electrons. Because Kondo clouds are formed at low temperature, the resistance of metals increases at low temperature. Kondo effect in the QD is special in that "single" Kondo cloud exists around the QD. Mesoscopic systems are suitable to study quantum mechanics because the electric measurement is accurate enough to compare theoretical results with experimental results. Furthermore, the system can be tuned continuously from equilibrium regime to nonequilibrium regime by applying a bias voltage, which enables us to survey the quantum mechanics in nonequilibrium regime.

The research in the mesoscopic system not only receives the benefit of electronics but also promotes improvement of electronic measurement. Quantum Hall effect (QHE) is one of the

most excellent products of mesoscopic research, which is utilized to defines resistance standard by physical constant e and h[11]. Thanks to the research on QHE in 2DEG, the relative uncertainty of resistance reaches sub-ppb orders now[12].

1.2 Measurement standard

In this Thesis, we treat a single electron device, namely a quantum dot. There are two motivations why the QD is important. They are related to the electric current standard and the single electron dynamics. In this subsection, we briefly explain the significance of the current standard. Measurement is a comparison with measurement standard, and so the stability and accuracy of the standard are important. The unit of length "ft" is, for example, used to be defined by the foot of the human body. Even if the standard was defined by the foot of someone, actually the king, the length was unstable and depended on country and era. It is impossible to ensure traceability of measurement, which means the values have no reliability and no universality. Therefore measurement standard must be universal to enable to compare results measured at different time and place. It is important for not only science but also industry and daily life. You will get trouble even in buying daily staffs if the standards have large uncertainty. Almost of all units are based on Système International d'unités (SI) which consist of length m, mass kg, time s, electric current A, temperature K, amount of substance mol and luminous intensity cd[12, 13]. In November 2018, a revision of the SI is decided at Conférence générale des poids et mesures (CGPM) in order to redefine the standards [14]. The revision defines the electric current with a practical method, the mass with Planck constant h to abolish definition by the material whose mass can be changed by oxidization, and the temperature with Boltzmann constant k_{B}.

The world's measurement experts are trying to decide the standards with small uncertainty. The electric current is one of them. The present (on February 2019) definition of Ampere is as follows; "The ampere is that constant current which, if maintained in two straight parallel conductors of infinite length, of negligible circular cross-section, and placed 1 metre apart in vacuum, would produce between these conductors a force equal to 2×10^{7} newton per metre of length."[15]. The SI newly defines the current I with using elementary charge e and the number of charges which transmits the conductor per second f as below

$$I = ef. \tag{1.5}$$

This definition is based on single electron operation developed by mesoscopic research. Since a QD enables to control the electron whose charge is e one by one, radio frequency (RF) operation with frequency f generates the current $I = ef$. The present electric current standard is, however, derived through Ohm's law by the standards of resistance and voltage defined by the quantum phenomenon QHE and AC Josephson effect. The uncertainty of the current generated by the QD is too large to define the current comparing the resistance standard and the voltage standard, whose relative standard uncertainty reach ppb order[12]. The uncertainty stems from loading error of electron into the QD and emission error from the QD. The world's measurement experts try to define the current by various techniques, for example, error detection with single electron transistor (SET), modulation of radio frequency's waveform, integration of single electron sources etc. [16, 17, 18, 19, 20]. Our work is related to establishing the electric current standard with single electron sources.

1.3 Electron dynamics

Here, we discuss the relevance of the study of the electron dynamics by using single electron sources. Single electron sources which are also called "pumping device" are not only tools to define the electric current but also tools to investigate fundamental physics and electron dynamics. Dynamics in quantum mechanics is a frontier where few experiments have been done. Therefore it is important for the development of physics to yield new results on electron dynamics. Because biasing of V generates the current whose energy distribution is E_F to $E_F + eV$ even at zero Kelvin, it is hard to observe how the electrons relax their energy. Here, E_F is Fermi energy. In this sense, single electron sources can generate pure excitation of an electron whose energy distribution is, in principle, a delta function at $E_F + E_{\mathrm{pump}}$, where E_{pump} is the energy of the pumped electron. There are two methods for studying electron dynamics using single electron sources.

- Wave packet measurement with two particle interference.

- Tomography of energy and time with pump-probe measurement.

Here we focus ourselves on the two-particle interference to measure wave packet of electron pumped by single electron sources. The transport in mesoscopic system is the transmission of a single electron through it, which does not depend on quantum statistics. As far as the transmission of a single particle is considered, electron and photon make no fundamental difference. Fundamental differences arise when two or more particles are involved in the transmission with interference. So two-particle interference is the simplest measurement to observe quantum statistics. Detection of the ideal two-particle interference requires

- Beam splitter to entangle two particles when they enter

- Two particle sources under the control of incidence timing and emission energy

- Measurement technique to detect whether or not two-particle interference occurs.

Equipment of two particle interference is two inputs (particle sources), a beam splitter, and two outputs (detectors) as shown in Fig. 1.4.

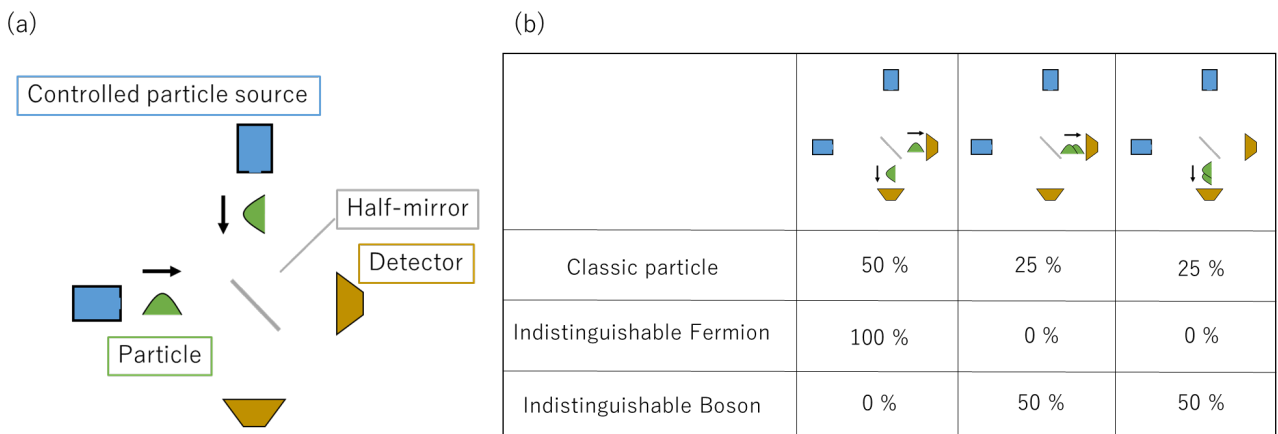|			
Classic particle	50 %	25 %	25 %
Indistinguishable Fermion	100 %	0 %	0 %
Indistinguishable Boson	0 %	50 %	50 %

Figure 1.4: Particle's statistics dependence of two particle interference. Each particle is shown as a wave packet. In case that distinguishable particles come in the beam splitter, the result is the summation of transmission probability. In the case of Boson, particles propagate along the same path. In case of Fermion, each particle goes path to a different path each other.

In the case of Fermion, the two inputs, the beam splitter, and two outputs are an on-demand single electron sources, a QPC, and digitizers through resonant circuits, respectively. Because key points of two particle interference are indispensability of two particles and overlap of two wave packets; in other words the two electrons with the same energy each other should be injected into the QPC at the same time. Quantum statistics of electrons is substantiated by Hong-Ou-Mandel interference which is the measurement technique to observe two-particle interference[5, 21]. Figure 1.5 (a) shows the setup of observation of two electron interference with single electron sources.
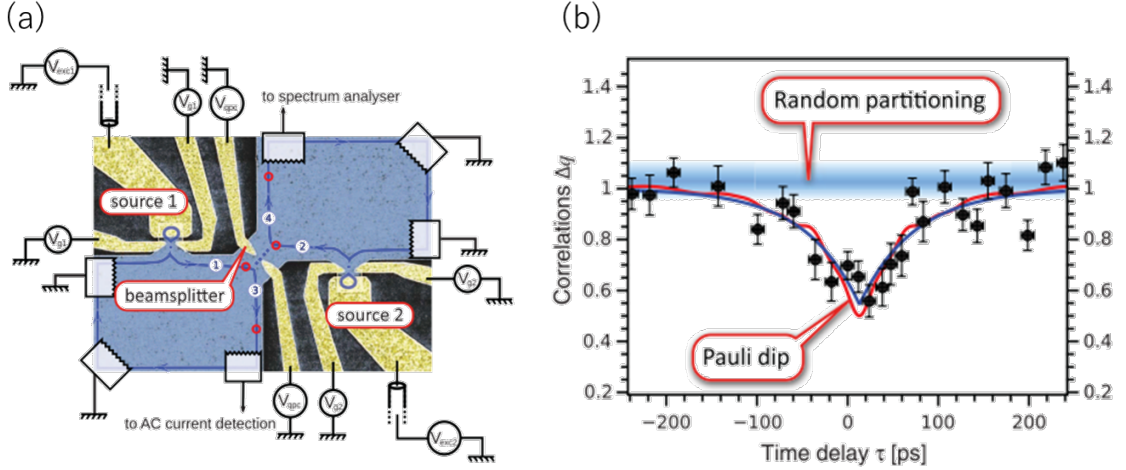

Figure 1.5: The observation of electron interference with single electron sources in 2DEG. (a) The experimental setup of two electron interference. (b) Delay of pumping timing dependence of noise signal. These figures are taken from Ref. [21].

QHE plays great roles on quantum optics with electrons because electrons in the QHE regime has the low possibility to lose their energy and are guided by the edge of 2DEG. Two electrons are injected into the beamsplitter made of a QPC by the on-demand single electron sources (sources 1 and 2 in Fig. 1.5). Since the emission timing is controlled by the RF, the overlap of two electrons' wave packet is controlled by the time delay of RF. When two electrons enter the beamsplitter at the same time, two electrons are entangled and avoid each other due to the Pauli principle. Since electrons are emitted periodically, the noise -variance of the current as a function of time- is suppressed as shown in Pauli dip of Fig. 1.5 (b). When time delay is large, the two electrons are scattered by the beamsplitter independently as shown in random partitioning of Fig. 1.5 (b). Because the width of this dip comes from the width of wave packets of emitted electrons, two electron interference gives the information of electron wave packet.

In the QHE regime, the edge channels co-propagate and interact with each other. Therefore electrons in QHE regime can be regarded as a Tomonaga-Luttinger liquid [22, 23]. Tomonaga-Luttinger liquid shows the spin-charge separation. Figure 1.6 shows the sketch of relaxation of the pumped electron into the charge mode and the spin mode (neutral mode)[24], and the setup which is the same with that of Ref. [21].
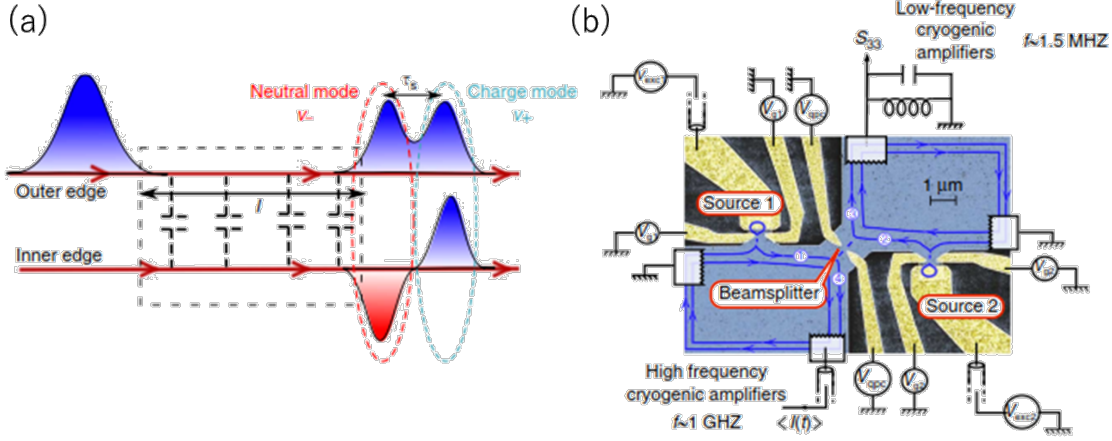
Figure 1.6: (a) Sketch to express that wave packet excited by single electron source relaxes into the charge mode and the charge mode. Blue peaks mean the wave packets of fractional electrons. Red dip means the wave packet of the fractional hole. (b) The setup is the same as that of Ref. [21]. taken from Ref. [24].

The excited electron on the edge channel relaxes into the charge mode and the neutral mode due to the one-way propagation and the interaction between the edge channels. The charge mode consists of two fractional electrons in the outer and inner edge channels. The neutral mode consists of one fractional electron in the outer channel and one fractional hole in the inner channel. In this way, the wave packet measurement with two particle interference is a useful method to reveal electron dynamics.

Since the emission timing of on-demand single electron sources is controlled by RF signal, real-time measurement with pump-probe technique is available[25, 26]. Pump probe measurement yields the information of the emission process and the speed of the pumped electron. It is also possible to spectroscope the pumped electrons, which reveals how the electrons relax their energy. Single electron sources provide the way to survey electron dynamics in condensed matter.

2 Nano-fabrication of 2DEG wafer

Most of all experiments in mesoscopic physics receives the benefits of semiconductor technology. Especially, two-dimensional electron gas system (2DEG) formed at heterostructure between GaAs and $Al_xGa_{1-x}As$ (referred to AlGaAs later) gives us high controllability of the transports enough to perform various experiments. In this Chapter, I first give an overview of 2DEG and nano-fabrication, and then introduce detail of the fabrication[27, 28].

2.1 Overview of 2DEG

Our experiments use GaAs/AlGaAs 2DEG fabricated by Molecular Beam Epitaxial (MBE). MBE system enables us to grow atomic layer on the substrate one layer by one layer. Figure 2.1 shows a schematic figure of how 2DEG is formed.
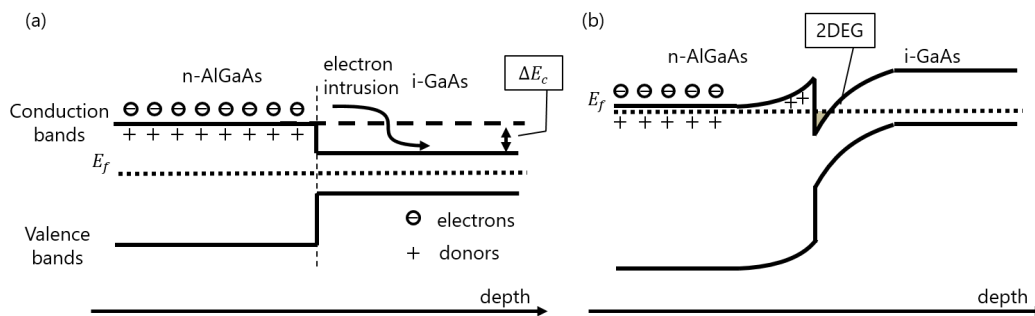

Figure 2.1: Schematic figure of how 2DEG is formed. (a) Schematic figure of bands before free electrons from dopant intrude. (b) Schematic figure of bands after free electrons in $n-$AlGaAs intrude into $i-$GaAs.

The letter before material corresponds to the type of dopant. "n, p, i" indicates electron-doped, hole-doped, and non-doped, respectively. GaAs and AlAs are semiconductors whose bands and gap are $1.4\,\mathrm{eV}$ and $2.1\,\mathrm{eV}$, respectively. Because they have almost the same lattice constant, mixed crystal of GaAs and AlAs (AlGaAs) is possible. The band gap of AlGaAs is modulated by mixing ratio between $1.4\,\mathrm{eV}$ and $2.1\,\mathrm{eV}$. Free electrons in $n-$AlGaAs intrude into the conduction band of $i-$GaAs which is lower than that of AlGaAs by E_C [Fig. 2.1]. Free electrons supplied by the donors intrude into $i-$GaAs, but free electrons cannot go back to $n-$AlGaAs due to the potential barrier stemming from the energy gap ΔE_C [Fig. 2.1 (b)], which forms 2DEG.

The advantage of 2DEG is a long mean free path of electrons because the place of electrons propagates in $i-$GaAs layer which has a small number of impurities, and is far from impurities (donors) which work as potential disorder spatially. Furthermore, $i-$AlGaAs can be introduced between $n-$AlGaAs and $i-$GaAs, which separates donors and electrons. Such a layer is called "spacer", which makes impurity scattering rate lower. A few groups can fabricate 2DEG wafer

whose mobility is so high that electrons can propagate $100\,\mu$m without losing energy. Not only mean free path but also Fermi length of 2DEG is longer than that of electrons in conventional metal. Quantum phenomena occur remarkably if the size of the conductor is of the same order as the characteristic length, for example, Fermi wavelength, mean free path, and coherence length of electrons. Whereas Fermi wavelength of typical metal is a few angstroms, Fermi wavelength of electrons in 2DEG is around tens nm. Tens nm is large enough to be fabricated with a lithography technique. Another advantage of 2DEG lies in its high controllability by using the Schottky gate electrodes deposited on the 2DEG wafer. Applying a negative voltage, it is possible to control the spatial distribution of electrons, and trap electrons in a box as treated in quantum mechanics textbook (quantum dot).

Because of the two-dimensionality, quantum Hall effect occurs under strong magnetic field. Quantum Hall effect plays an important role in quantum optics with Fermion, i. e. electron, because backscattering of conduction electron is suppressed in the edge transport. Using edge transport, we can design the propagation path of conduction electron with gate voltage. These features of AlGaAs/GaAs based 2DEG are convenient for Fermion quantum optics. In Fig. 2.2, I show the actual design of wafers used in our experiment.
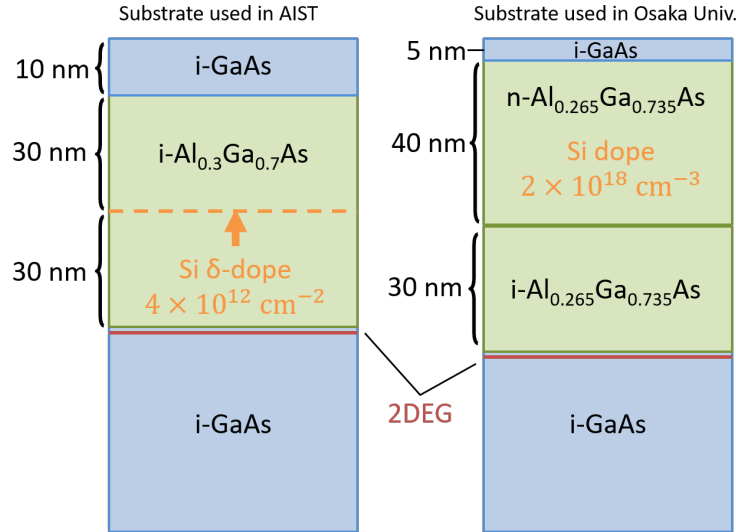
Figure 2.2: Structures of 2DEG substrate in this study. The substrate used in National Metrology Institute Japan (NMIJ), National Institute of Advanced Industrial Science and Technology (AIST) was developed in NTT Basic Research Laboratories. The substrate used in Osaka university was developed in Sumitomo Electric Industries, Ltd.

2.2 Overview of nano-fabrication

The mesoscopic system is fabricated by the nano-fabrication process based on lithography techniques. Figure 2.3 shows schematics of the nano-fabrication process. Thin polymer film called "resist" is essential to fabricate nano-structures. There are various kinds of resist. Some of them are easily resolved. Some have strong resistance against acid. Some guarantees high resolution and/or high sensitivity etc. Thin film is obtained by spin coating of polymer solvent on the substrate and baking it. The positive resist is changed into low molecular chemicals easy to be developed by exposure of light or accelerated electrons. On the other hands, negative
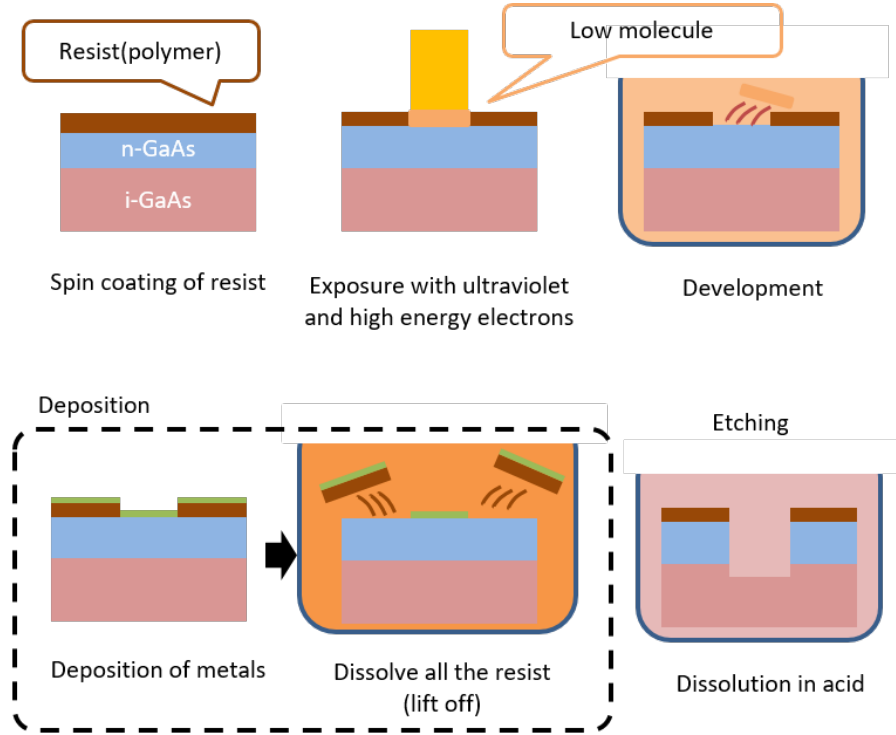
Figure 2.3: Schematic figure of the nano-fabrication process. In this figure, the resist is a positive type.

resist becomes hard to be solved. The fine patterns are developed by putting exposed substrate into developer. The fineness of the developed patterns depend on how light and accelerated electrons are concentrated. The line width of lithography with light (photolithography) is limited by fineness of the photomask and wavelength of light. Conventional light source has around 300 nm wavelength, which is good enough to fabricate down to a few tens μm order structures. On the other hand, lithography with the accelerated electrons is called electron beam (EB) lithography. Wavelengths of electrons accelerated by 10 kV and 100 kV are around 40 pm and 4 pm, respectively. In principle, EB lithography can lithograph structure finer than photolithography. Lithography speed of EB lithography is, however, much slower than photolithography. Fine structures should be made by EB lithography and coarse structures should be better patterned by photolithography. Nano-fabrication is completed by deposition of material, dissolution with acid or milling with ion after developing pattern. Figure 2.4 shows a schematic figure of 2DEG sample with a Schottky gate electrode.

Figure 2.4: Schematic figure of 2DEG sample.

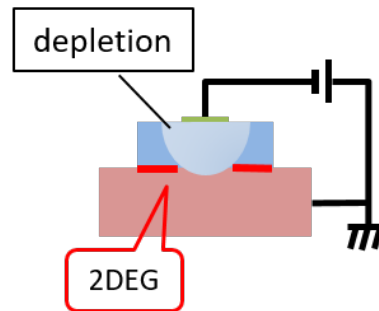Since 2DEG is formed by electrons originally in $n-$AlGaAs, 2DEG under etched $n-$AlGaAs is killed. As mentioned before, the negative voltage applied to gate electrode defines spatial distribution of 2DEG. By fabricating a wire-shaped conductor whose width is of the order of Fermi wavelength, the sub-bands with discretized energy (quantum point contact, QPC) can be formed. Even energy levels can be discrete in a box designed by gate electrodes, which is called quantum dot (QD). QD enables us to control a single electron and investigate transport across single energy levels. Actual samples which realize QPC and QD are shown in Chapter 3, 4 and 5.

2.3 Processes to fabricate 2DEG sample

Now, I introduce the detail of my nano-fabrication process. Most of the description here is related to the fabrication of the tunable barrier tunneling devices on a narrow 2DEG wire (see Fig. 2.14). Quality of the sample depends on various parameters, resist, dose, etchant etc, and so it is important to integrate knowledge on how to fabricate good samples. Because the sample made in National Metrology Institute Japan (NMIJ), National Institute of Advanced Industrial Science and Technology (AIST) is fabricated by a conventional process without narrow 2DEG electrodes, I will detail below the process of single electron source on $1\,\mu$m width 2DEG nano-wire fabricated in Osaka University. The narrow 2DEG wire is desired in order to prevent unintended QDs from forming and to perform a real-time measurement. The velocity of electrons in quantum Hall edge channel is measured [26]. They propagated $5\,\mu$m in 100 ps. It is impossible to study dynamics in shorter than 100 ps if the width of 2DEG is $5\,\mu$m. Therefore techniques to fabricate 2DEG nano-wire must be established.

First, the substrate should be cleaned to remove covering methyl methacrylate (MMA) or polymethyl methacrylate (PMMA), and particles. The substrate is put into "Remover PG" and
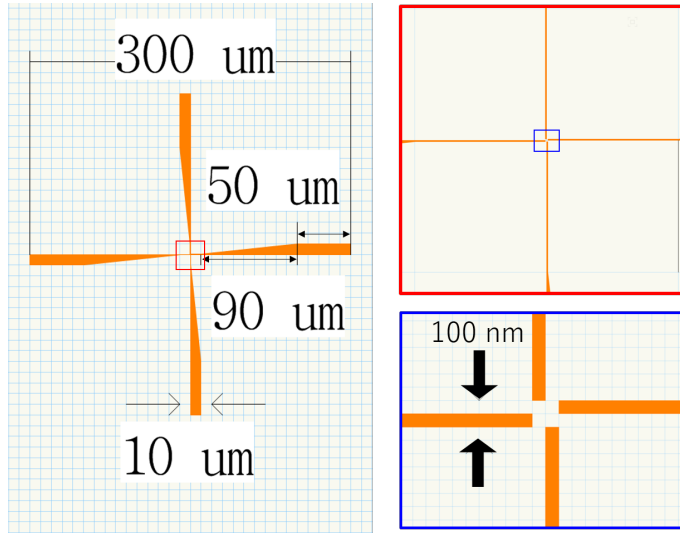

Figure 2.5: Mark design for EB lithography. The right top figure is enlarged figure indicated with a red square in the left figure. The right bottom figure shows the region enclosed by blue lines in the right top figure. A 100 nm wire is lithographed at $950\,\mu$C, and the others are lithographed at $800\,\mu$C.

is washed with ultrasonic washing machine. Hot Remover PG ($< 90\,^\circ$C) is the best solvent. In that case, it is recommended to lid the container to prevent evaporation. This may be the final chance to clean the substrate with ultrasonic washing machine. Because the solvent which has already solved resist is poor to solve organic materials, the new solvent should be used. Remover PG is rinsed off with acetone and 2-propanol. When the substrate is in some solvent, the cup should be stirred in order for it to be exposed to fresh solvent. After the substrate is transferred from Remover PG into acetone, the tweezer should be rinsed with acetone, too. Otherwise Remover PG on the tweezer drops on the substrate at blowing with dry nitrogen gas. The cleaning process is followed by the ashing process with ultraviolet ozone cleaner. Its condition is 5 min at $180\,^\circ$C with $1\,$L/min O_2 flow. After cleaning, coat PMMA with spin coating. Its condition is slope 5 s/ 5000rpm 40 s/ slope 5 s. The substrate is baked at $180\,^\circ$C for 2 min without a lid. After exposing, the patterns are developed. Developing condition is PMMA developer 1 min/ 2-propanol 30 s. This condition is to develop PMMA. First I always deposit mark made of (Substrate/) Ti 5 nm/ Au 100 nm to align EB pattern (Fig. 2.5) and photo-mask ($30 \times 100\,\mu$m$\square$ rectangle). Lift off process is almost the same as the cleaning process. However ultrasonic washing should not be done because electrodes may be destroyed. Instead of ultrasonic washing, stream injected from a syringe is good to remove resist. If resist stays on the substrate, ultrasonic washing in a short time (within 5 sec) might help to solve the problem. The substrate is etched in order to define the area of 2DEG. We use S1813G for etching process which has strong resistance to acid. In order to increase the adhesion, I perform hexamethyldisilazane (HMDS) treatment after the ashing process. Figure 2.6 shows the substrate under HMDS treatment. HMDS treatment is the exposure of the wafer vapor to HMDS. In my case, I put HMDS into a cooper cup made of a copper plate and pipe whose size is $\phi 5 \times 3\,$mm and heat it up at $135\,^\circ$C. Then I put the wafer next to the cup and put a beaker to lid. After HMDS evaporates, the lid are removed and the substrate remains for 5 min to dry them up. After cooling them down, the wafer is spin-coated with S1813G with slope 5 s/ 5000rpm 40 s/ slope 5 s. Baking condition of S1813G is set at $90\,^\circ$C for 10 min. HMDS treatment should be done in a draft chamber because ammonium gas is generated. S1813G

Figure 2.6: The wafer is under HMDS treatment. The copper cup is made of a copper plate and copper pipe. This treatment should be done in a draft chamber because heated HMDS generates ammonium gas.

works as a negative EB resist and a positive photoresist. It is good to combine EB lithography
of fine pattern and photolithography of coarse pattern. The area exposed by EB should be
exposed by ultraviolet. S1813G is developed by MF319. MF319 is a special developer for
S1800 series which contains alkali. Development condition is to sink the substrate into MF319
for 30 s and water for 10 s. Figure 2.7 shows the pattern for etching which has a micron order
pattern. As seen, the photomask is aligned with the rectangle of metals placed at the bottom
left. In order to remove residual resist, the sample is ashed at 90 °C for 1 min. The wafer is
etched by an etchant which consists of H_2SO_4 (96 wt%): H_2O_2 (30-35 wt%): H_2O with a ratio
of 3: 1: 200 (volume) for 1 min under the homemade stirrer. Stirring prevents the reaction
products to stay around the substrate because they inhibit the expected chemical reaction of
etching. It is important to stir the cup to obtain homogeneous etching. The wafer is rinsed
with water stream generated by a syringe immediately because the water turns into etchant if
the wafer is put into the water. Figure 2.8 shows the sample after removal of the resist with
hot Remover PG. Fine structure narrower than 1 μm is successfully fabricated[1].
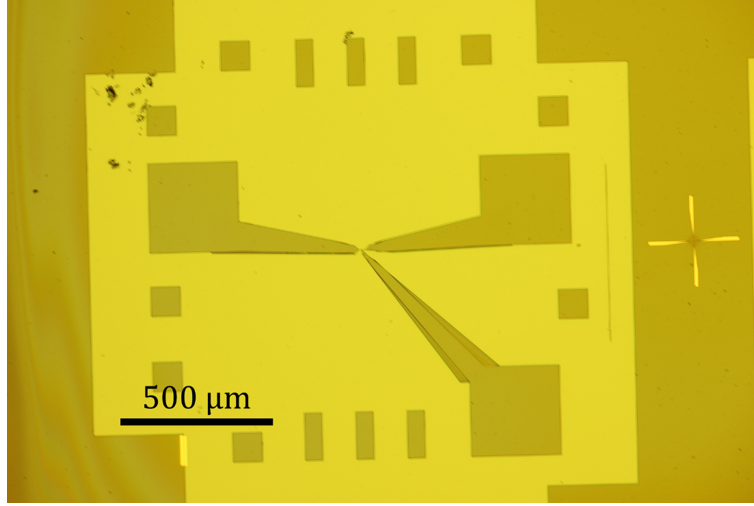

Figure 2.7: The developed sample is aligned with a cross mark and 30 μm × 100 μm rectangle
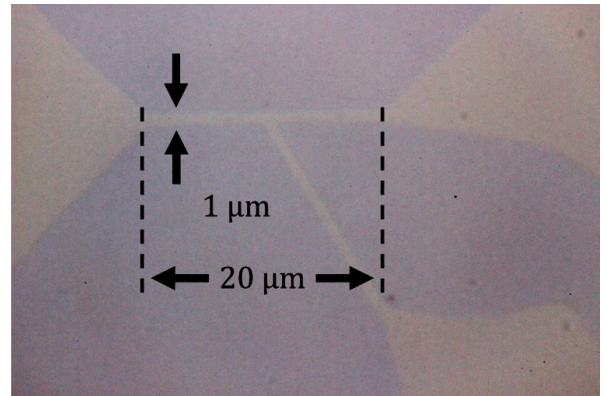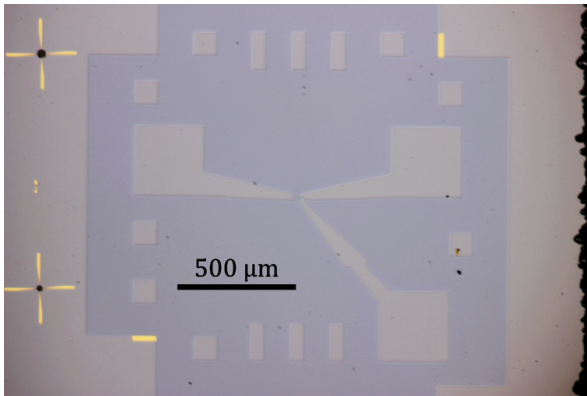mark.

Figure 2.8: The etched sample after removing the resist.

[1]Scanning Electron Microscope (SEM) image will be shown later in Fig. 2.14.

Figure 2.9: How to keep furnace 1 atm. After flushing, the output port is put into oil to keep furnace at 1 atm. Then all ports are closed.

Ohmic contacts are made by photolithography, vacuum deposition system and alloying. In this step, photomask should be aligned with the etched pattern in order to make the edge of the sample alloyed[2]. In order to make the wire bonding easier, pads of the gate electrodes should be alloyed. Alloyed metal is so strong that it is possible to repeat the wire bonding. Otherwise, the bonding pad is easily peeled. After development, the substrate is ashed again with the condition 90 °C for 1 min to remove the residual resist. In order to remove the oxidized layer, the substrate is put into hydrochloride acid (10 wt%) for 30 s and is rinsed with water. Before the substrate is oxidized, it should be settled into the deposition system immediately. An alloy of gold and germanium (AuGe 88:12 wt%) is deposited by resistance heating of a tungsten (W) boat to keep the mixing ratio of the alloy. Molybdenum (Mo) boat is not recommended to deposit AuGe because the boat is contaminated. About 0.3 g of AuGe in total is deposited with monitoring by "Au", which results in the deposition of the thickness between 80 and 110 nm. Nickel (Ni) is deposited by EB deposition system with a one-sixth thickness of the AuGe layer[3]. The deposited substrate should be put into hot Remover PG for one night because the resist after the resistance heating deposition is too hard to remove. After removing the resist, the wafer is ashed as it was treated in the etching process. The resist must be removed completely because burned resist is hard to be removed. Before alloying, the furnace should be flashed several times by nitrogen gas. A pressure in the furnace should be 1 atm at room temperature. The output of the furnace clack valve is connected into an oil as shown in Fig. 2.9. Close input valve with checking bubbles generated in oil, then close output valve to seal the furnace. Figure 2.10 shows temperature control to alloy Ohmic contacts. PID parameters are to be decided to keep the highest temperature, in this case, 440 °C.

---

[2]If edge of 2DEG is not alloyed, the transport property is not properly obtained in the quantum Hall regime.
[3]Because Ni and AuGe are deposited in different chamber, this thickness ratio may not be precise.
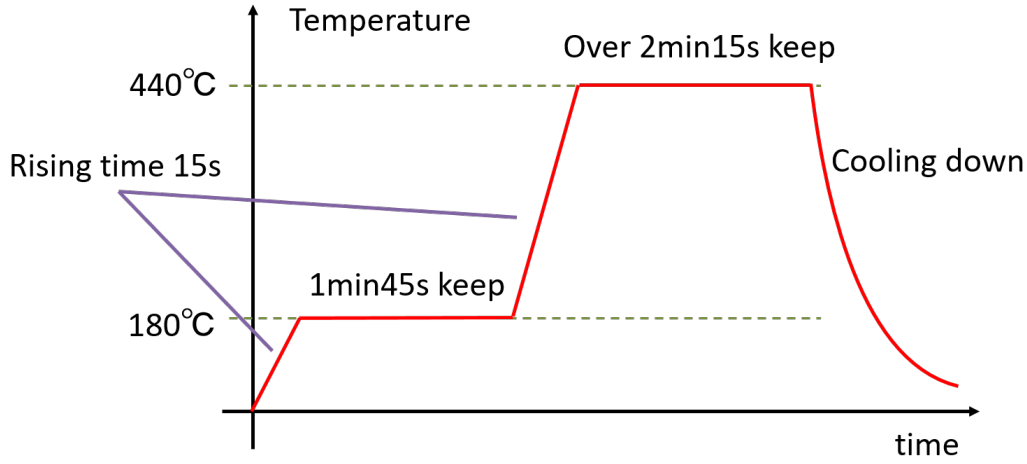
Figure 2.10: Temperature control of the alloying process. The PID parameters set for MILA-500, ULVAC Inc. are P 6.76, I 11.0, and D1.6.

After finishing heating process, the wafer is cooled down by 1 L/min nitrogen flow. After alloying, the Ohmic metals turn from a flat surface to a bumpy one, as shown in Fig. 2.11. If the final temperature of this alloying process is too low, Ohmic metals remain flat, indicating that the alloying process is incomplete. The color of the Ohmic metal sometimes turns from gold into silver, sometimes not. Empirically, however, its color has no relation with the quality, i. e. the contact resistance. After alloying, the electrodes should be deposited immediately. After photolithography, the wafer is ashed for 1 min at 90 °C to remove the residual resist which may harm electric conduction. It is then put into hydrochloride acid (10 wt%) for 30 s and is rinsed with the water stream in order to remove the oxidized layer. Then the coarse electrodes with large areas are deposited. They consist of a sticky layer Ti 5 nm and Au 100 nm on the substrate.
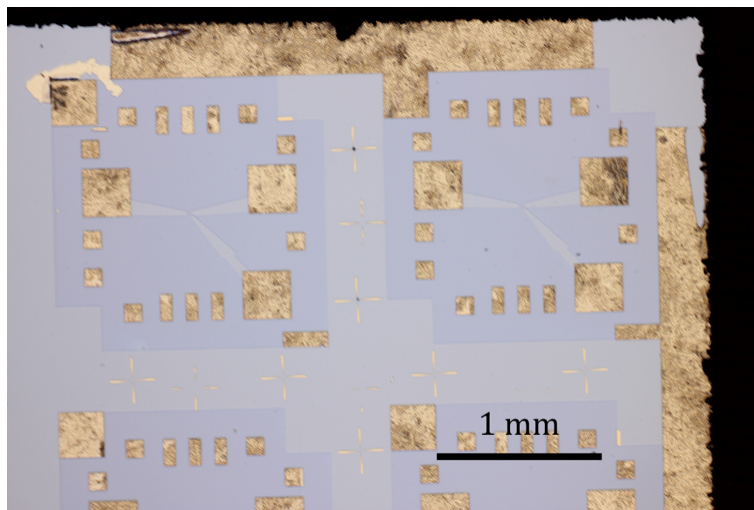
Figure 2.11: The substrate just after the alloying process. The metals turn from a flat surface into a bumpy one.
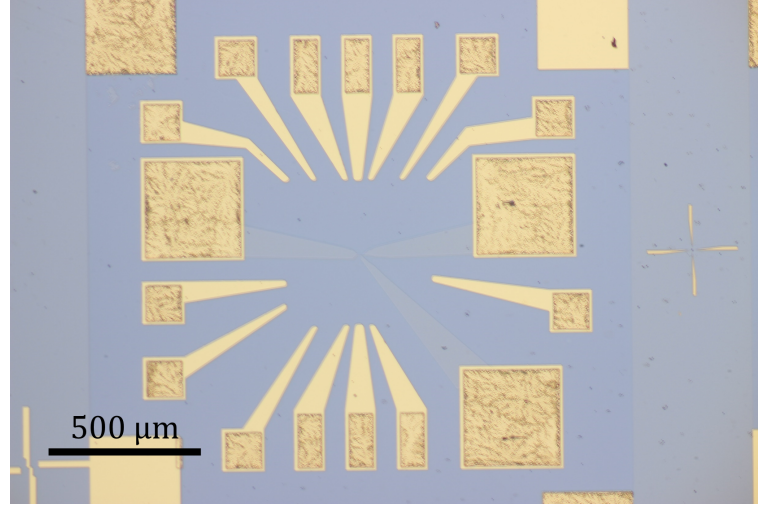
Figure 2.12: An optical photo of the sample after deposition of the large-sized electrodes.

After deposition of the large-sized electrodes, the fine electrodes are fabricated with EB lithography and metal deposition. The deposited material is the same as the large electrodes. Since the pattern size of our EB lithography machine (Elionix ELS7000 100 kV Electron Beam Lithography system) is $600\,\mu\mathrm{m}\square$, all the large gate electrodes reach within $600\,\mu\mathrm{m}\square$ (see Fig. 2.13)[4]. In this way, the tunable barrier tunneling device is fabricated as shown in Fig. 2.13 and 2.14. The property of the device is discussed in Chapter 5.
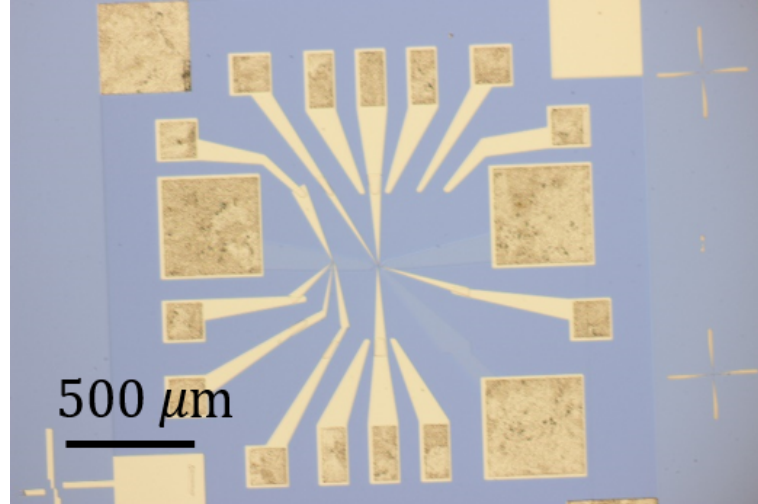
Figure 2.13: an optical photo of the sample after fine electrodes are deposited.

---

[4]Because the acceleration voltage of ELS7500a in AIST is 50 kV, the maximum of exposed area is $1200\,\mu\mathrm{m}\square$. ELS7500a is good enough to fabricate electrodes narrower than 100 nm width (see Fig. 2.17).
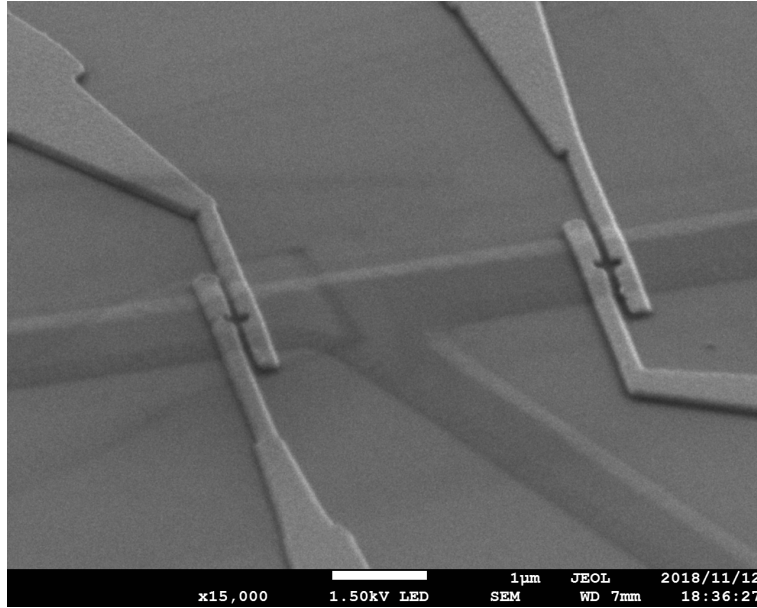
Figure 2.14: A SEM image of the sample. Tunable barrier tunneling devices are fabricated on a narrow 2DEG wire.

2.4 Conclusion

In this Chapter, I have detailed the fabrication process and techniques to fabricate a single electron source -tunable barrier tunneling device. This is an essential tool for Fermion quantum optics and studying dynamics in mesoscopic systems. I show the experimental data of these devices in Chapter 5.

2.5 Appendix

I find it meaningful to describe here all I tried even if some of them are not successful. I list up apparatus and chemicals for fabrication.

2.5.1 List of apparatus and chemicals

Fabrication apparatus

- Ultrasonic cleaning machine works at 28, 45 and 100 kHz.
- Spin coater (MS-A100, MIKASA): It rotates to make thin layers of resist.
- Hotplate (HP-25A, AS ONE): It heats substrates and solvent.
- Mask aligner and exposure system (USHIO): It exposes the substrate to ultraviolet light for optical lithography.
- Ultraviolet ozone asher (UV-1, samco): It removes organic compounds, for example, residual resist.
- Infrared furnace (MILA-500, ULVAC): It is used to make Ohmic contacts by the alloying.
- Vaccum vapor deposition system (Eiko): It equips electron beam heating and resistance heating.

- Electron Beam lithography system (ELS7000, Elionix): It uses a focused beams of electrons to lithograph nano- or micro-sized patterns on substrates. The acceleration voltage of ELS-7000 is $100\,\mathrm{kV}$. I use it in Osaka University.
- Electron Beam lithography system (ELS7500a, Elionix): Its acceleration voltage is $50\,\mathrm{kV}$. I use ELS7500a in AIST, Tsukuba, Ibaraki.
- Scriber (K-604S10, KYOWA RIKEN Co., Ltd.): It is utilized to cut substrate crystals.
- Dish dryer: It dries flasks and measuring cylinder.
- Homemade-stirrer: It stir flasks at $60\,\mathrm{rpm}$ with a radius of $1\,\mathrm{cm}$ to keep the substrate exposed by flesh solvent. This stirrer was made by myself[29].

Chemicals

- Remover PG (Micro Chem): The first solvent to remove resist and organic material. It consists of 4-methyl-2-pentanone and surfactant. The datasheet recommends rinsing the substrate in IPA. However, I recommend rinsing the substrate in acetone and IPA.
- Acetone: Convenient organic solvent. Generally, I rinse Remover PG off.
- 2-propanol (IPA): It is used for the last rinse. It is also used to make the developer of PMMA.
- 4-methyl-2-pentanone (MIBK): It is used to make the developer of PMMA.
- HMDS (AZ AD promoter, AZ Products): It makes adhesion of the resist stronger.
- S1813G (Rohm and Haas Electronic Materials): A positive photoresist and negative EB resist which have strong resistance to acid[30]. Last two digits, namely, 13 in this case, shows ratio of resin to total weight. Last letter G means the color of the solvent.
- MF 319: A developer for S1800 series which contains alkali.
- PMMA A4 (Micro Chem): positive EB resist. The optional letter says that PMMA is solved in "A"nisole with "4" wt%.
- MMA (Micro Chem): Sensitive positive EB resist which is easy to solve.
- SAL-SR7 (used in NMIJ, AIST): Negative EB resist.
- CD-26: developer of SAL-SR7
- Sulfuric acid (96 wt%): It is used to make etching solvent. It might be good to stock diluted one because it generates heat when it is diluted, and diluted sulfuric acid is a convenient acid to stock.
- Hydrogen peroxide (30-35 wt%): It is used to make etching solvent. It must be stored in a fridge to avoid evaporation. Otherwise, concentration will be changed.
- Hydrochloric acid (10 wt%): It removes the oxide layer before deposition of ohmic contacts. Its bottle should be sealed with vinyl tape to prevent evaporation of hydrochloride.
- Developer for PMMA: Combination of 2-propanol and 4-methyl-2-pentanone with a ratio of 3: 1 (volume).
- Etchant: Etching solvent of GaAs. Combination of H_2SO_4 (96 wt%): H_2O_2 (30-35 wt%): H_2O with a ratio of 3: 1: 200 (volume). This chemical should be made just before etching.

It is STRONGLY RECOMMENDED to divide chemicals into small bottles in order to avoid contamination. If the purity of material is important, chemicals should be stocked carefully. Due to contamination, for instance, adhesion of resist is lost. Before using resists stocked in fridges, it should stay at room temperature to warm in order to prevent dew condensation.

2.5.2 Substrate cleaving

The substrate of 2DEG is necessary to be cleaved into small pieces for experiments after the fabrication processes are finished. Special care must be taken in order not to make scars on the front side of the substrate because they create unrepairable damages on the 2DEG. In wafer holder, the back side of the wafer is pushed by star shape plastic. You should not be nervous about holding the wafer with a tweezer because 2DEG does not exist the area of 5 mm from the edge of the wafer. Before scribing on the substrate, the substrate should be covered by resist in order to prevent contamination. Scribing lines on the substrate generates powder of the substrate. MMA, which is easily solved, is coated on the substrate with slow spinning speed to make thicker. The deeper the scratch is, the easier the substrate is cleaved. Cleaving is done by pushing the substrate inserted between two glass plates. It is recommended to clean glass plates with alcohol in order to prevent scratching the substrate.

2.5.3 Lithography

Spin coater is used to get a thin layer of resist on the substrate. The faster the spin coater rotates, the thinner layer of resist is. The homogeneous thickness of the resist is desired. I will show the best condition to obtain homogeneous resist layer in Table 2.1.

Thickness	Conditions
Thin	slope 5 s/ 5000 rpm 40 s/ slope 5 s
Thick	3000 rpm 40 s/ slope 5 s

Table 2.1: Spin coating condition

This recipe is independent of resist and wafer. When one wants to rotate slowly, the slope is not necessary. Baking makes resist hard with the evaporation of the solvent. Photolithography gives a few tens μm structures and electron beam lithography gives one hundred nm structures. The dose condition for electron beam lithography depends on the acceleration voltage and the resist. For example, if the acceleration voltage is higher, the dose will be larger because high energy electrons can penetrate the materials and do not contribute for making patterns (compare Fig. 2.17 and Fig. 2.18). After the exposure process, the wafer is developed. The conditions of baking, developing, and rinse depend on the resist (see Table 2.2).

Resist	Bake	Developer	Rinse
PMMA	2 min at 180 °C	MIBK: IPA =1:3 (volume) 1 min	2-propanol 30 s
SAL-SR7	1 min at 100 °C	CD-26 4 min, distilled water 10 s	acetone 5 s, 2-propanol 5 s
S1813G	10 min at 90 °C	MF319 30 s	distilled water 10 s

Table 2.2: Development conditions for each resist.

The radius of the electron beam depends on the lithography current and so fine patterns should be lithographed by a small current. I show the dose dependence of resists and acceleration voltage in Fig. 2.15, Fig. 2.16, Fig. 2.17 and Fig. 2.18.

| 8000 μC/cm^2 | 10000 μC/cm^2 | 12000 μC/cm^2 | 14000 μC/cm^2 | 16000 μC/cm^2 |
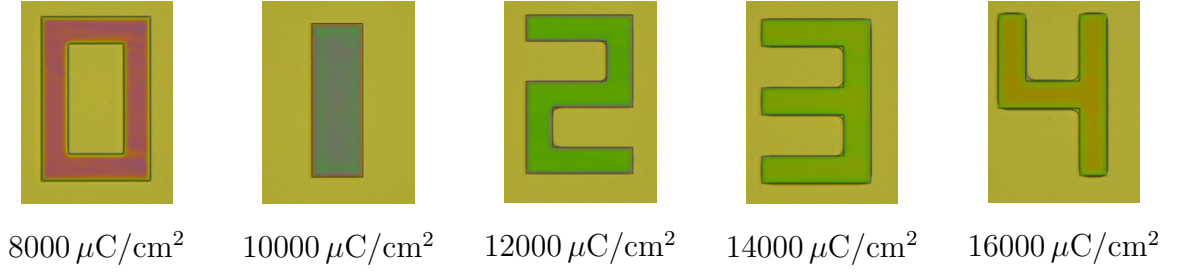
Figure 2.15: Dose dependence of SAL-SR7. Except for "1", the line widths are set 20 μm. EB lithography conditions are set to be 1200 μm□, 120000 dot, 1 nA, and 50 kV.
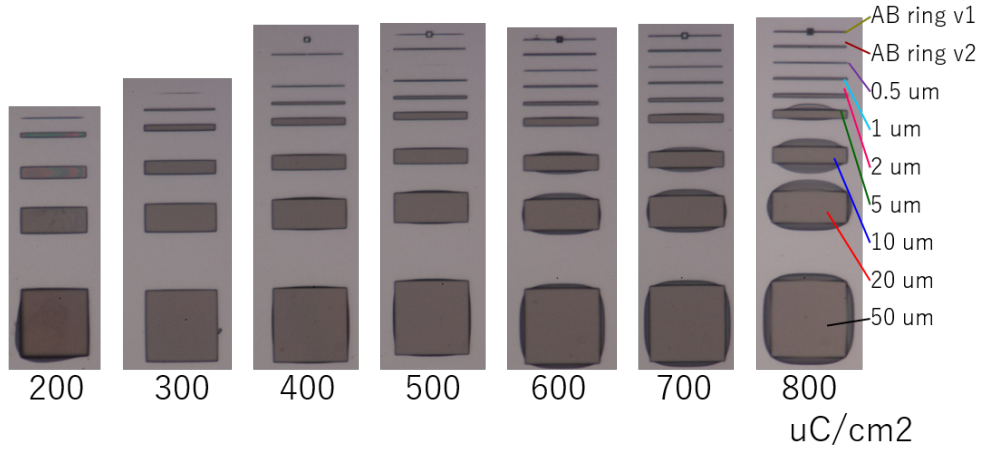
Figure 2.16: Dose dependence of S1813G as a negative EB resist. The right legends indicate the widths or the names of the structures. EB lithography conditions are set to be 600 μm□, 60000 dot, 1 nA, and 100 kV.

| 480 μC/cm^2 | 510 μC/cm^2 | 540 μC/cm^2 |
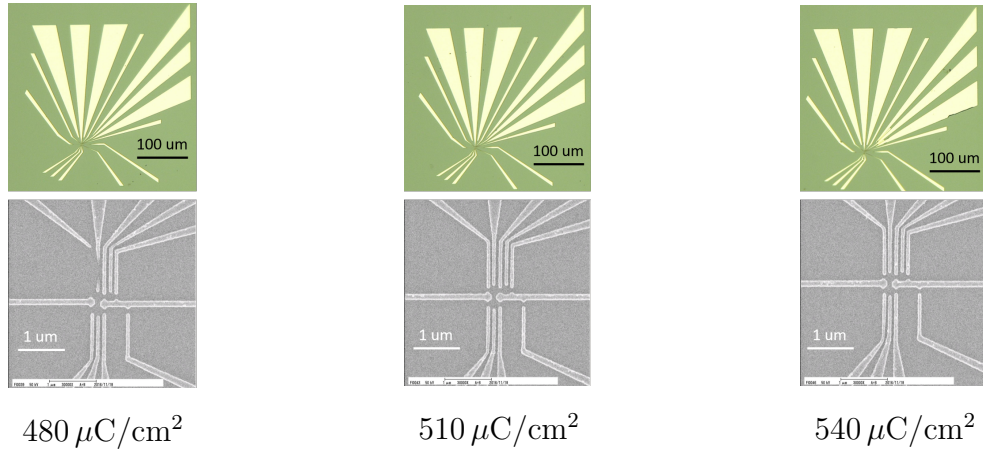
Figure 2.17: Dose dependence of PMMA. Figures show the patterns written by EB lithography with the conditions of 600 μm□, 60000 dot, 100 pA, and 50 kV. The line width of electrodes, except for center splitting gates, whose width is designed as 100 nm, is designed to be 50 nm. Actual line width is around 80 nm.
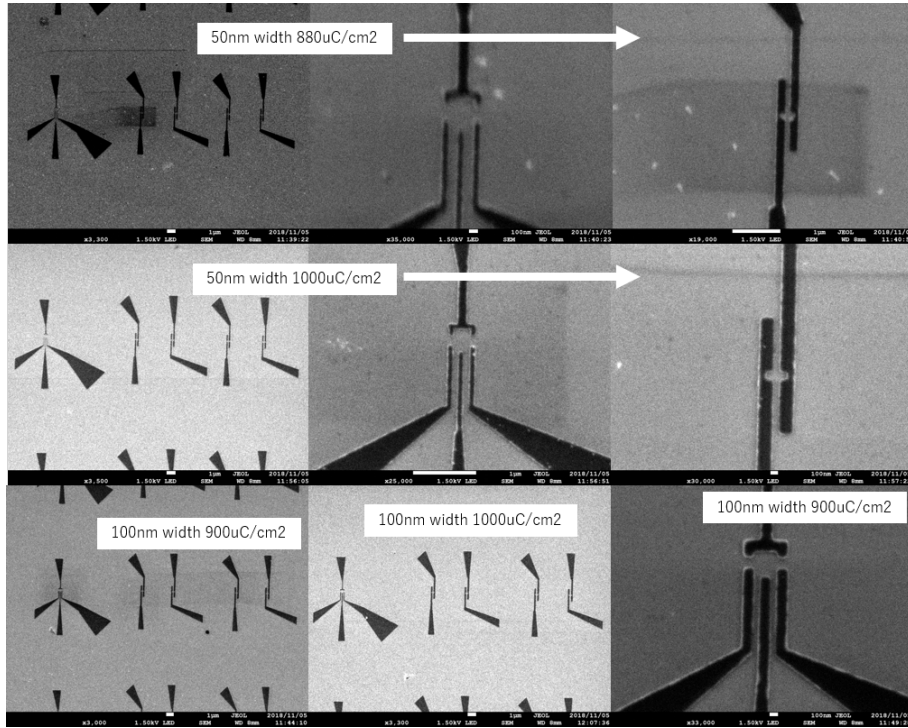
Figure 2.18: Dose dependence of PMMA A4. EB lithography conditions are set to be 600 μm$\square$, 60000 dot, 200 pA, and 100 kV. The line width of the narrowest part in the top and center panels is designed to be 50 nm. The line width of the narrowest part in the bottom panel is designed to be 100 nm.

Silver is useful to check dose condition because it is around a hundred times cheaper than gold. It is, however, hard to see with an optical microscope because thin silver is transparent. Therefore it is not suitable for marks to align the mask for photolithography. If you perform all the process with EB lithography, you can use silver to deposit marks. As shown in Fig. 2.17 and Fig. 2.18, best condition to lithograph pattern depends on acceleration voltage because penetration depth depends on the energy of electrons. High energy electron penetrates material deeper than lower energy electron. For the same reason, we set the acceleration voltage low when we observe the surface with a scanning electron microscope. Since backscattering rate of emission current depends not only on the acceleration voltage but also on the substrate, to check dose condition is important.

2.5.4 Wet etching

Figure 2.19: Checking how HMDS treatment works. At that time, I did digital wet etching (see text). Obviously, adhesion of resist becomes stronger. However, the adhesion is not strong enough to fabricate fine structures.

In the wet etching process, it is important to improve the adhesion of resit because the precision of etched pattern strongly depends on the strength of the adhesion. Generally speaking, cleaning the oxidized layer with acid or alkali is a popular method to make adhesion strong. However they, for example, hydrochloride acid and "semico-clean", destroy 2DEG. HMDS treatment works well to improve adhesion without damaging 2DEG. Figure 2.19 shows how HMDS treatment makes adhesion of resist stronger. After etching one cycle, the resist on the non treated substrate is peeled, but the resist on the HMDS treated substrate remains. Obviously, HMDS treatment makes adhesion of the resist stronger.

Even if HMDS treatment is done, the etching technique needs to be established. As shown in Fig. 2.20, the conventional EB resist (PMMA and ZEP) is weak to acid.
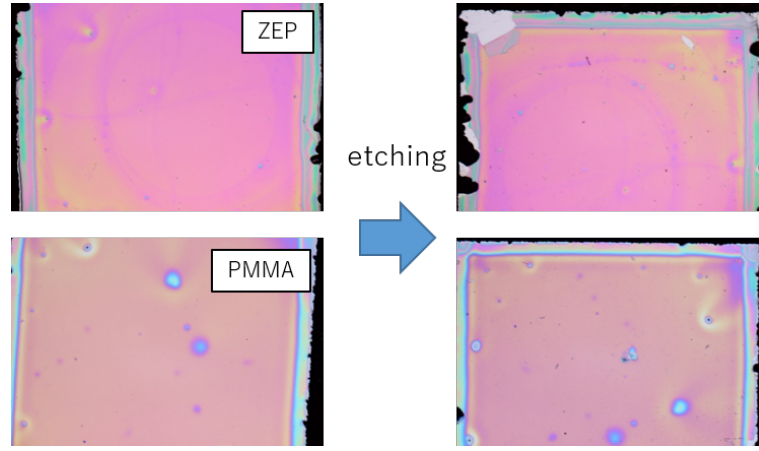
Figure 2.20: Resists without any lithography process are etched. Even though they have been treated with HMDS process, both of them are destroyed.

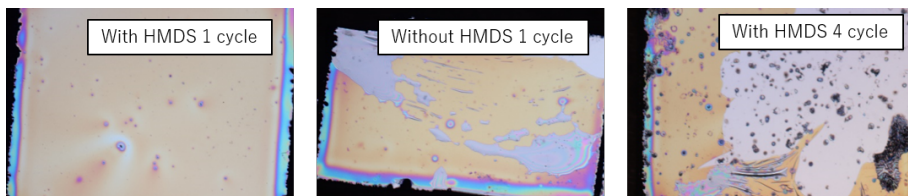I try digital wet etching to get fine structure[31]. I thought that digital wet etching is the best method to fabricate fine structure because the etching process proceeds with oxidization by hydrogen peroxide and removal of the oxidized layer with an acid. Furthermore, we do not need to care about the concentration of acid and hydrogen peroxide. My recipe is (i) putting the sample into acid for 30 s, (ii) then rinsing with water by spin coater method, (iii) putting into hydrogen peroxide for 30 s, and rinsing with water by spin coater method. I repeat this cycle for five times. Figure 2.21 shows atomic force microscope (AFM) image of the fine structures made by this etching process. Figure 2.21 (a) shows an Aharonov-Bohm ring made by the digital wet etching process. Its depth is around 40 nm. Figure 2.21 (b) shows narrow 2DEG wire made by the conventional etching process as introduced in the previous section. Its depth is about 40 nm as shown in Fig. 2.21 (c). Etching depth is almost the same, but its roughness is completely different. In the case of Fig. 2.21 (a), it is estimated that etching solvent intruded between the resist and the substrate since the sample was sunk for a long time (longer than 5 min in total). On the other hands, in case of Fig. 2.21 (b), it is estimated that the etching process had been finished before etchant intruding since the sample was sunk for 1 min.
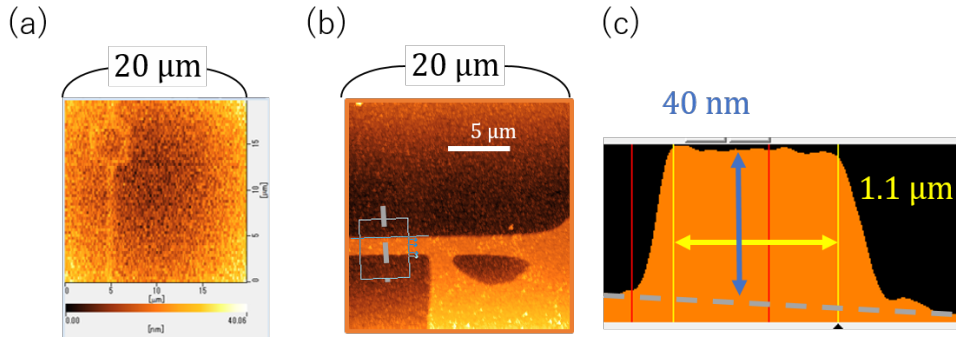
Figure 2.21: AFM image of etched structures. (a)Aharonov-Bohm ring made by digital wet etching. One cycle is to sink a substrate into acid and hydrogen peroxide for 30 sec. For this sample, five cycles are performed. (b) The sample etched by a conventional method with etchant shown the previous section. The fine structure was designed to be "y" shape. Resist between two arms, however, had linked due to overdose. (c) A line profile of (b) across narrow 2DEG wire.

3 Fano effect in transport of double quantum dot

In this Chapter, we describe the Fano effect in a transport of an artificial molecule [1]. We show that the conductance of lateral series double quantum dot (DQD)

3.1 Introduction

Transport in a single discrete energy level in a quantum dot (QD) has been a central subject in mesoscopic physics [32]. QD studies are significant because they allow us to address each energy level in a fully tunable way. It was successfully demonstrated that a QD behaves as an artificial atom, where the shell structure of the energy levels and the associated Hund rule were observed as in a real atom [33]. Several QDs can be coupled in series to realize an artificial molecule [34], which has also been an important subject, especially in qubit research [35].

In addition to the above features, QDs are also important in that they enable us to explore how coherent transport occurs through a single discrete level. The level energies of a QD can be tuned by a nearby gate electrode, and the zero-temperature conductance as a function of the gate voltage exhibits a Lorentzian lineshape as a result of resonant tunneling, as the transmission amplitude through a single level is described by the Breit–Wigner formula [36]. The resulting transmission probability $\mathcal{T}(E)$ is expressed as

$$\mathcal{T}(E) = \frac{A}{(E - E_{\mathrm{res}})^2 + (\Gamma/2)^2}. \tag{3.1}$$

Here, A, E, E_{res}, and Γ are the amplitude of the resonance, the electron energy, the resonance energy, and the energy width of the resonance, respectively. The conductance of QDs has already been established to have a Lorentzian line shape [32]. Note, however, that even if the underlying transport mechanism is coherent, the information on the phase is not immediately obvious in the obtained Lorentzian of Eq. (3.1).

Phase measurement of an electron wave packet through a QD has been an important research topic in mesoscopic physics for more than 20 years [37, 38, 39, 40, 41, 42]; for example, experimentalists have measured the phase in the transport of a QD embedded in an electron interferometer such as an Aharonov–Bohm (AB) ring, which has inspired many theoretical works. As a result of the combination of resonance and interference, the Fano effect was observed in a QD embedded in an AB ring [43, 44]. The Fano lineshape is given as [45, 46].

$$\mathcal{T}(\tilde{\epsilon}) = A\frac{(\tilde{\epsilon} + q)^2}{\tilde{\epsilon}^2 + 1}, \quad \text{where } \tilde{\epsilon} \equiv \frac{E - E_{\mathrm{res}}}{\Gamma/2}. \tag{3.2}$$

Here, q is called the Fano asymmetry parameter. Unlike the Lorentzian curve, this is an asymmetric peak with a dip at $\tilde{\epsilon} = -q$. This occurs through interference resulting from electron

propagation between the discrete level and the continuum, directly reflecting the phase evolution of the electron wave packet.

The Fano effect has been studied in various systems, for example, in atomic photoionization [47], neutron resonance scattering [48], photoemission [48], Raman scattering [49], photo-absorption of a QD [49], infrared spectroscopy [49], photoluminescence [50], and scanning tunneling spectroscopy [51, 52]. After this effect was observed in the transport of QD in the early 2000s [43, 44, 53, 54, 55, 56], it was observed in various mesoscopic systems: crossed carbon nanotubes [56], a side-coupled QD [57, 58], and the Fano-Kondo coexistence regime [58, 59, 60]. Therefore, it is meaningful to explore the electron transport based on this effect in other systems to deepen our understanding of mesoscopic transport. Such a study is also important to further clarify the phase behavior of a QD in multilevel transport [41, 42, 61, 62].

In this Chapter, we investigate the Fano effect in the transport of an artificial molecule. We show that the conductance of lateral double quantum dot coupled in series shows this effect under a wide range of experimental conditions and define the coupling between the DQD and the leads. The role of the state that is strongly coupled to the leads is discussed. Our observation is supported by a numerical calculation including this state. Our numerical calculation indicates that the energy splitting due to the anti-crossing can be modulated by introducing an energy continuum that causes the Fano resonance.

3.2 Experimental setup

We fabricated the DQD from GaAs/AlGaAs based two dimensional electron gas (2DEG) grown in NTT Basic Research Laboratories. Fabrication is done by standard electron beam lithography, vacuum vapor deposition with resistance heating, and wet etching[1]. Figure 3.1 shows a
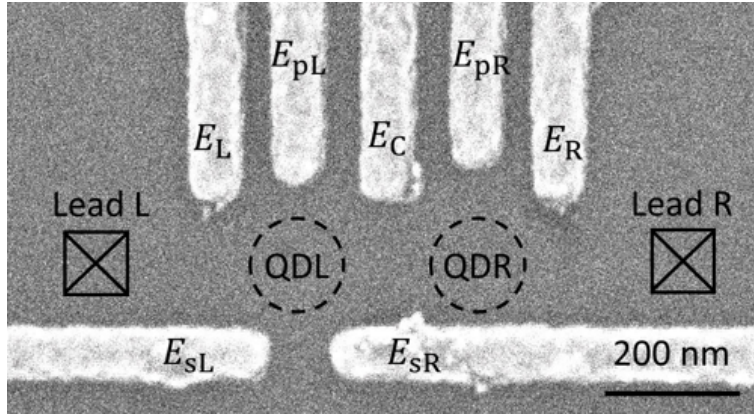
Figure 3.1: SEM image of the DQD device. White regions indicate gate electrodes(E_L, E_pL, E_C, E_pR, E_R, E_sL and E_sR) on 2DEG(Gray region). V_L, V_pL, V_C, V_pR, V_R, V_sL and V_sR say negative voltage applied to E_L, E_pL, E_C, E_pR, E_R, E_sL and E_sR, respectively.

scanning electron microscope (SEM) image of the sample. E_sL and E_sR cut the conductance between top 2DEG and bottom one (we do not discuss the role of the bottom part in this Chapter). In this chapter, V_sL and V_sR were fixed at $-0.90\,\mathrm{V}$, which is strong enough to kill the transmission between top 2DEG and bottom one. The QD on the left (QDL) is defined

---

[1]In this case, phosphoric acid was used.

by E_L, E_{pL}, E_C, E_{sL} and E_{sR}. In the same way, the QD on the right (QDR) is defined by E_C, E_{pR}, E_R, E_{sL} and E_{sR}.

Measurement was done in a mixing chamber of dilution refrigerator BF-LD250, BlueFors Cryogenics Oy with a base temperature of 8-30 mK at zero magnetic field. The conductance was measured by standard lock-in technique with IV converter made by Dr. Shuji Nakamura[2] Its excitation was 10 μV at 19 Hz. All DC lines are filtered by RC low-pass filter at room temperature and powder filter at mixing chamber. We used Lock-in Amplifier SR830, voltage supplier SIM928 (Stanford Research Systems), and voltage supplier GS200 (Yokogawa Test & measurement Corp.). Due to the poor battery, SIM928 can be used to applying gate voltage[3].

3.3 Single quantum dot

In order to discuss Fano effect, I first show the transport in a single QD. Even if QD have no clear continuum, Fano effect in single QD is reported previously [53, 54, 55, 56]. Figure 3.2 shows the transport in QDL when V_L and V_C are fixed at -1.3512 V and -1.1200 V, respectively. Figure 3.2 (a) is V_{pL} dependence of conductance at zero bias. In this chapter, the conductance is
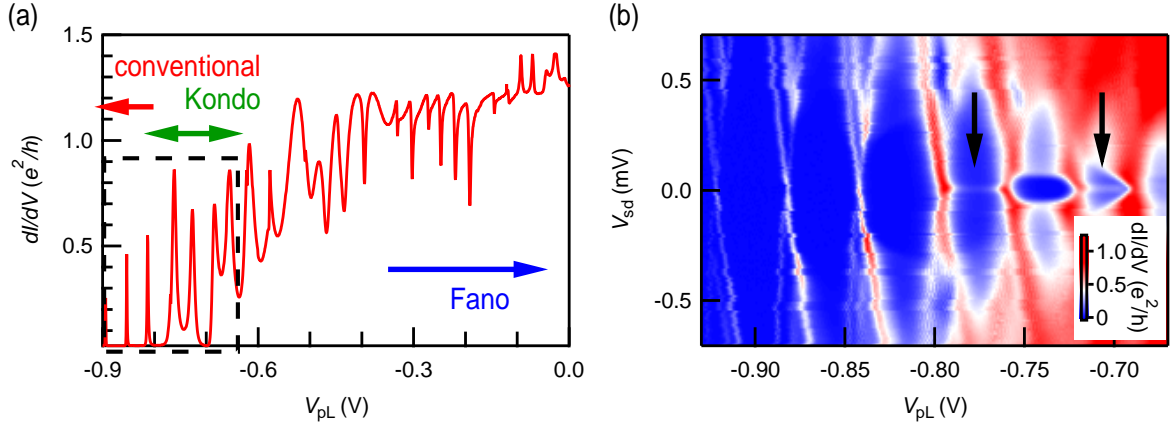
Figure 3.2: Transport of QDL. V_L and V_C are fixed at -1.3512 V and -1.1200 V, respectively. (a) V_{pL} dependence of conductance at zero bias. Continuous transition from conventional quantum dot to Kondo region and Fano region is observed as V_{pL} increases. (b) Intensity plot of the differential conductance as functions of bias voltage V_{SD} and V_{pL} in the range indicated by dashed lines in (a). Coulomb blockade regions were observed. The black arrows indicate Kondo zero bias peaks.

expressed in units of $e^2/h \sim (25.8 \, \text{k}\Omega)^{-1}$. In the strong negative voltage region ($V_{pL} < -0.8$ V), the conductance shows a typical symmetric Coulomb peak between Coulomb blockade. In Coulomb blockade, the number in the QD is fixed. Therefore, the conduction electrons cannot transmit the QD. On the other hand, the number in the QD can change at Coulomb peak. That is the reason why the conductance increases. This is a typical transport of single discrete level

---

[2]His IV converter is consist of three instrumentation amplifiers and one OP amp. Two instrumentation amps are used to combine two signal, for instance, DC signal and AC signal. These outputs are connected to the non-inverting input of the OP amp whose output is connected to inverting input through return resistance. Inputs of last instrumentation amp are connected with non-inverting input and output of the OP amp.

[3]SIM928 has a low capability to recharge.

which has weak dot-lead coupling and proof that the number of the electrons can be controlled one by one. The width of resonant peaks acquired by fitting these lines and lever arm $20 \, \mu\text{eV/V}$ estimated by Fig. 3.2 (b) allows us to estimate that electron temperature is lower than $300 \, \text{mK}$.

The weaker negative voltage applied to V_{pL}, Kondo effect was observed. Kondo effect originates from the localized magnetic moment (spin freedom of the electron in the QD) and electrons in Fermi surface. Kondo effect in a QD is observed as a zero bias conductance peak when the quantum dot has large dot-lead coupling [6, 7]. Figure 3.2 (b) shows clear zero bias conductance peaks. Because localized magnetic momentum is required, Kondo resonances are observed alternately. This result indicates that V_{pL} modulates not only discrete levels but also coupling between discrete level and leads. This behavior that gate electrode affects on the neighboring gate electrode is also observed in transport in the double quantum dot. As the further weaker negative voltage is applied $V_{\text{pL}} > -0.4 \, \text{V}$, the increase of the conductance and asymmetric structures - a feature of Fano resonance- are observed [53, 54, 55, 56]. As mentioned before, V_{pL} modulates dot-lead coupling. In this regime, discrete levels can have strong dot-lead coupling which has a large energy width. Summation of a lot of such states can be regarded as a continuum which leads to conductance increase and Fano resonances. This continuous transition in a single QD from isolated discrete level to Kondo region to Fano region is perfectly consistent with the previous result [56].

3.4 Conventional double quantum dot

Next, we show the transport in double quantum dot. This section is the main result of this Chapter. First, I explain transport in conventional DQD in order to clarify what it is new. Left side of Fig. 3.3 shows transport in conventional DQD. Figure 3.3 (c) shows the intensity plot of conductance as functions of V_{R} and V_{L} when V_{C}, V_{pL} and V_{pR} are fixed at -0.95, -0.50, and -0.2 V, respectively. Fig. 3.3 (b) is the corresponding line profile at $V_{\text{L}} = -1.5 \, \text{V}$. The plot is a so-called charge stability diagram of DQD. As one can see, honeycomb-like lattice with conductive lines "charge transition lines", insulating "Coulomb blockade regions" surrounded by conductive lines and highest conductive points "triple point" are observed. These are features of transport in conventional DQD. If one goes across charge transition line, the number of DQD "charging state" is changed one by one. V_{R} controls not only the energy of discrete levels in QDR but also one in QDL and coupling between QDR and Lead R as plunger gate controls not only the energy of discrete levels but also dot-lead coupling in a single QD. In the same way, V_{L} mainly controls the number of DQL and affect on QDR and dot-lead coupling. This is the reason why charge transition lines tilt against V_{L} and V_{R}. Triple point originates from Coulomb interaction between QDL and QDR. If Coulomb interaction between QDL and QDR is absent, the charge stability diagram should be a tilted checkerboard pattern. If one QD gets an additional electron, the other QD requires the energy to get additional electron due to Coulomb interaction. Additional energy coming from Coulomb interaction between QDs can be controlled by V_{C}, which will be shown later.

In conventional DQD regime, Coulomb peaks show symmetric structures because the transport of each discrete level in QD obeys Breit-Wigner formula. Figure 3.3 (b) clearly show symmetric structures. These transport proves that our device works as a conventional DQD.
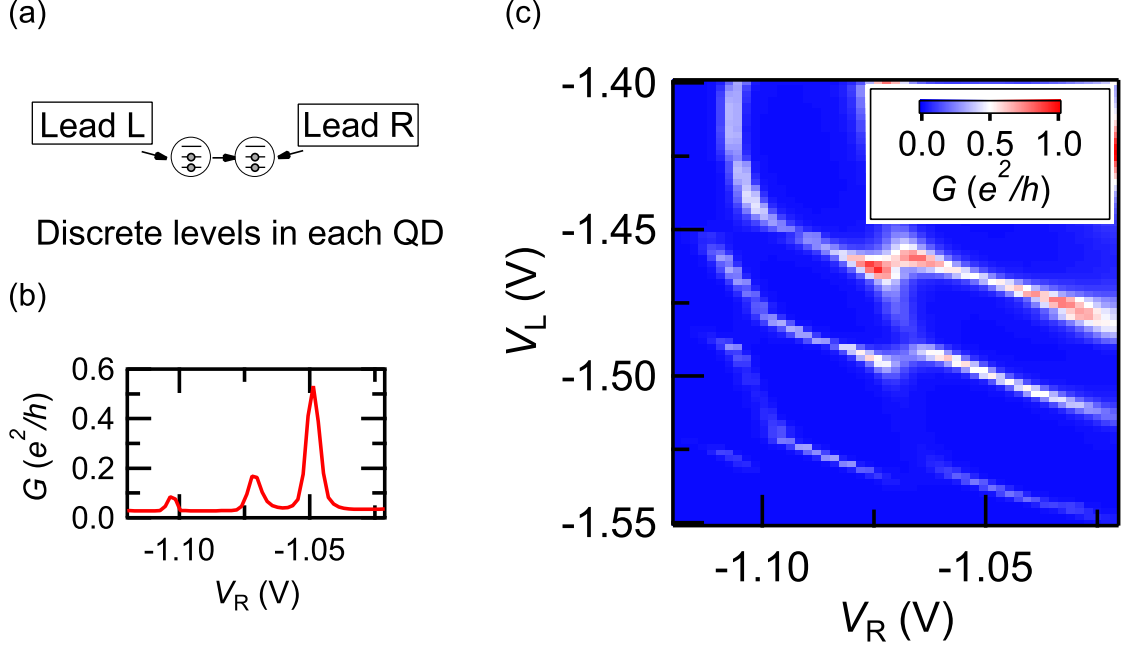
Figure 3.3: Transport of conventional DQD. (a) Schematic figure of a conventional DQD regime, which corresponds to the situation shown in (b) and (c). (b) The conductance as a function of V_R at $V_L = -1.5$ V. (c) The intensity plot as functions of V_R and V_L.

3.5 Double quantum dot in Fano regime

We discuss Fano transport regime, which is the main topic of this section. Figure 3.4 (a) schematicaly shows the situation of Figs. 3.4 (b) and (c), namely DQD in Fano regime. Figures 3.4 (b) and (c) are intensity plot of conductance as functions of V_L and V_R and the corresponding line profile at $V_L = -1.35$ V. Fano regime appears by applying the weaker negative gate voltage to V_L, V_C and V_R which indicates the emergence of the continuum in DQD. Actually, Fano effect is observed when V_L and V_L are weaker than ones in conventional DQD, and V_C is -0.7 V as I will explain later. Although the intensity plot of Fig. 3.4 (c) has honeycomb lattice similar to Fig. 3.3 (c), it has different features from one of the conventional DQD. First, charge transition lines are consist of asymmetric lines caused by Fano resonance. Second, in Fig. 3.4 (c), the regions inside honeycomb lattices are conductive, unlike the Coulomb blockade region in Fig. 3.3. These differences are clearly shown in Fig. 3.3 (b) and Fig. 3.4 (b). This situation, namely high conductance and symmetric lines, are consistent with the transport of single QD in Fano region.

All the above observations strongly indicate that the Fano effect emerges in our DQD system. Indeed each asymmetric line is nicely expressed by the following Fano formula [45, 63].

$$G(\varepsilon) = A\frac{(\tilde{\varepsilon} + q)^2}{\tilde{\varepsilon}^2 + 1} + G_0, \quad \text{where} \quad \tilde{\varepsilon} = \frac{\alpha(V_R - V_R)}{\Gamma/2} \tag{3.3}$$

Here, A, V_{res} and Γ are the amplitude, the gate voltage where resonance occurs, and the width of the resonance level, respectively. α is lever arm -gate voltage to energy conversion rate-, and

(a)

Discrete levels in each QD

(b)

(c)
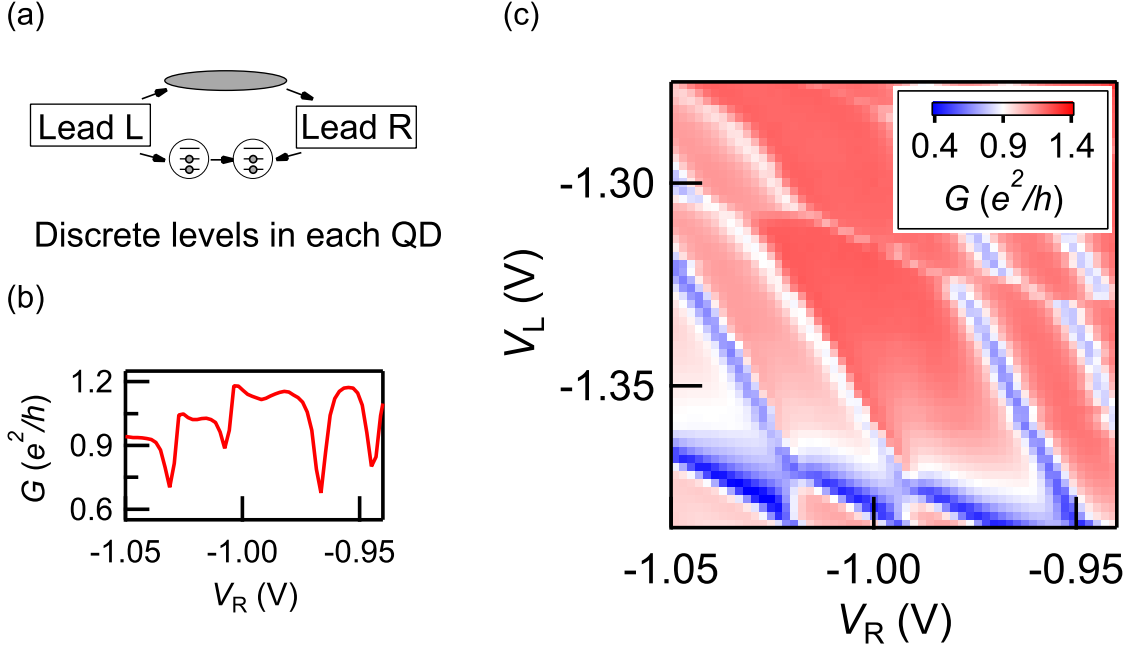
Figure 3.4: Transport of DQD in Fano regime. (a) Schematic figure of the DQD in the Fano region, which corresponds to the situation shown in (b) and (c). (b) The conductance as function of V_R at $V_L = -1.35\,\text{V}$. (c) The intensity plot as functions of V_R and V_L.

G_0 represents the background contribution. As introduced at the beginning of this Chapter, q is Fano's asymmetric parameter which characterizes the line shape. $|q|$ shows the ratio of the amplitude peak and dip, which is modulated by coupling strength between the discrete level and the energy continuum. For instance, for $|q| \to \infty$, the line shape goes to Lorentzian peak which means a usual discrete level without the energy continuum. On the other hand, for $|q| << 1$, only a dip structure emerges, signaling strong coupling between the discrete level and the continuum. The sign of q corresponds to the order of the interference as a function of ε, namely, destructive interference followed by constructive interference or vice versa.

We also measured V_{SD} dependence on the conductance in DQD in Fano regime. Sweeping axis should have been parallel to the tilted charge transition line or across triple points in order to evaluate lever arm precisely but, in our experiment, as the gate voltage seep was performed for the fixed V_L, the precise lever arm was difficult to obtain. We come back to this point just later. Figure 3.5 shows transport at $V_L = -1.36\,\text{V}$ and $V_C = -0.7\,\text{V}$. Figure 3.5 (a) is line profile of Fig. 3.5 (b) at zero bias. The asymmetric structures are fitted by Eq. (3.3), and the Fano's asymmetric parameter q and resonance with Γ are deduced. Since an unit of Γ is acquired as gate voltage, you have to convert from gate voltage to energy with lever arm estimated by Coulomb diamonds of Fig. 3.5 (b). Each resonance has its own q and Γ which are characterized by two-dimensionality of the wave function of discrete level. In this regime, $|q|$ is always smaller than one, which means that the discrete level and the continuum couple strongly. The sign of q is inverted around $-1.04\,\text{V}$, which suggests the phase of the energy continuum is shifted by π around this structure [55].

Three remarks are made here regarding the above treatment. First, Eq. (3.3) assumes that
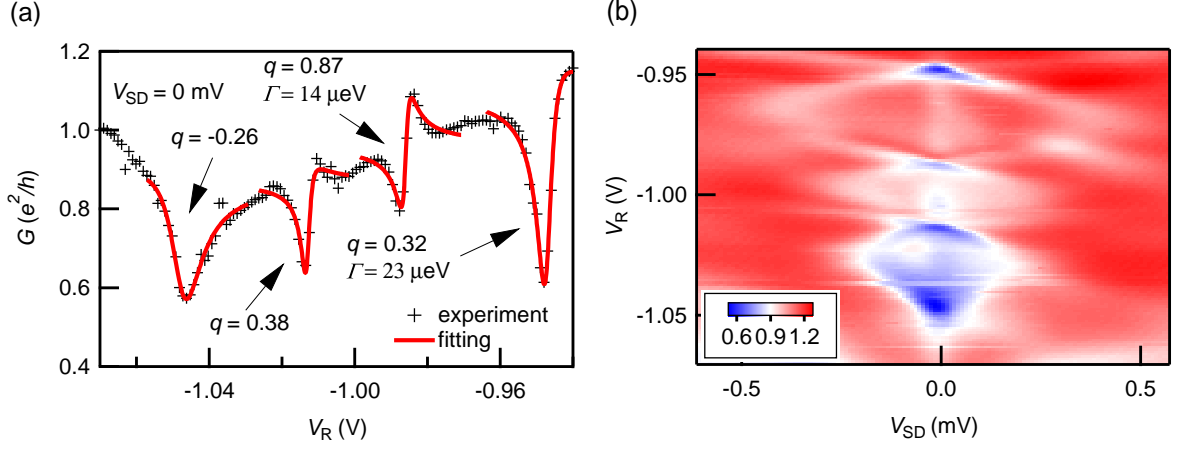
Figure 3.5: (a) V_R dependence of the conductance shows Fano's asymmetric line shape at $V_L = -1.36\,\text{V}$ and $V_C = -0.7\,\text{V}$. Each structure is fitted by Eq. (3.3). (b) Intensity plot of the differential conductance as a functions of V_{SD} and V_R at $V_L = -1.36\,\text{V}$ and $V_C = -0.7\,\text{V}$. Coulomb diamond-like structures with a zero-bias dip are observed.
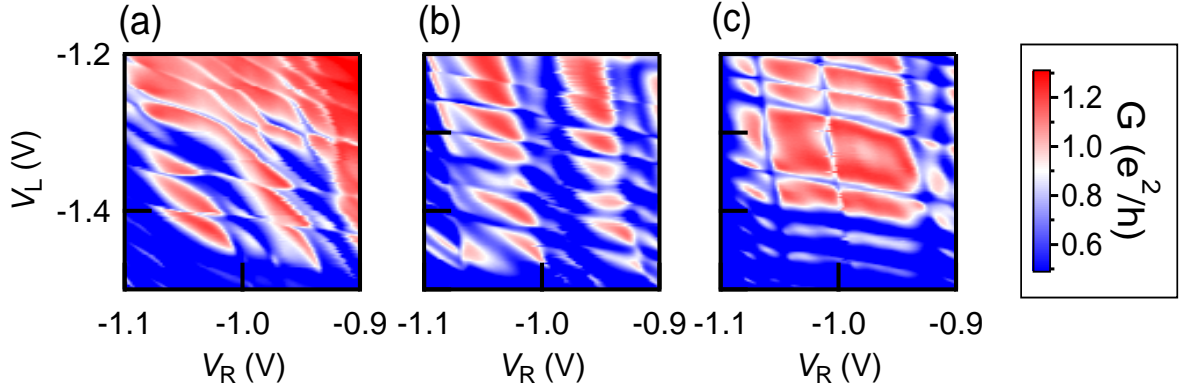
Figure 3.6: V_C dependence of intensity plot of conductance as functions of V_R and V_L. V_C controls Coulomb interaction between QDL and QDR. (a) The strong inter-dot coupling regime at $V_C = 0.7\,\text{V}$. (b) The medium inter-dot coupling regime at $V_C = 0.8\,\text{V}$ (c)The weak inter-dot coupling regime at $V_C = 0.9\,\text{V}$.

there is only a single level embedded in the continuum. Therefore, the fitting is valid only away from the crossing point of the levels of QDR and QDL. We will treat the crossing in the model calculation below. Second, as discussed before [44, 57, 64], the asymmetry parameter q is generally a complex number rather than a real one. However, the present experiment is performed at zero magnetic field, so q can be treated as real if the decoherence is negligible [64]. The third point is a technical one; the above q and Γ values are obtained for a fixed V_L, whereas V_R is swept. This procedure is justified only when V_L (V_R) controls the energy levels of only QDL (QDR). However, in experiments, cross-talk exists between the two; that is, V_L (V_R) affects the levels inside QDR (QDL) slightly, as clearly shown in Fig. 3.4 (c). Therefore, the above values of q and Γ may not be perfectly precise. Nevertheless, they are sufficient to prove that the Fano effect occurs in our device. We will include this cross-talk effect in the model calculation below. We measured the bias voltage dependence of the differential conductance of the system. Figure 3.5 (b) shows the V_{SD} and V_R dependence of the differential conductance at $V_L = -1.36$ V and $V_C = -0.7$ V. Although Coulomb diamonds appear, as expected, every diamond possesses dip structures at zero bias. These zero-bias structures have nothing to do with the Kondo effect because they do not show the even–odd parity effect, which should appear for the Kondo effect [6, 7, 65]. Similar structures associated with the Fano effect were observed in previous work [43, 53, 55, 66]. By analyzing the diamond, we found that the gate-voltage-to-energy conversion rate (α) is around 10 μeV/mV.

Finally, we control the coupling between QDL and QDR by modulating V_C. Figures 3.6 (a), (b), and (c) represent the charge stability diagrams at $V_C = -0.70$ V, $V_C = -0.80$ V, and $V_C = -0.90$ V, respectively. The coupling between the two QDs becomes weaker as $|V_C|$ increases. The peculiar asymmetric lineshapes are observed in all three diagrams, indicating that coherent transport occurs there. In Fig. 3.6 (a), the Coulomb repulsion between QDL and QDR significantly affects the transport, as honeycomb lattice structures appear. On the other hand, in Fig. 3.6 (c), where rectangular structures are observed, the interdot interaction is small. It was established that a similar variation of the charge stability diagram appears in the conventional DQD system [34, 67]. The present observation of this variation implies that the interaction between QDs is tunable even in a DQD in the Fano transport regime. Coupling between DQs dependence of charge stability diagram of conventional DQD is shown in Chapter 4.

3.6 Origin of the energy continuum

The Fano effect always emerges when the discrete levels and the energy continuum coexist, although it is not obvious why and where the energy continuum exists in the DQD geometry shown in Fig. 3.1. Previously, this effect was reported to occur in a single-QD system [53, 54, 55] and was theoretically analyzed [68]. These works suggested that a level that strongly couples to the leads acts as the continuum. Because an actual QD is not a zero-dimensional object but a two-dimensional one with a finite size, the coupling strength to the leads depends sensitively on the energy levels, reflecting the distribution of the wave functions inside the QD [68, 69, 70, 71]. As a result, there appear resonant states with sufficiently large resonance widths that can be regarded as the energy continuum. In a similar way, the present experimental observation evidently suggests that strongly coupled states between Leads L and R exist in the system, as shown schematically in Fig. 3.4 (a). This is the most natural assumption to explain the present observation.

   The Fano effect was reported before in the DQD system [66]. In that work, however, QDs situated in separate quantum wells are coupled vertically, and interference occurs through a resonant state in one well and a continuum state in the other well, which is a very different situation from our case. In our case, the continuum naturally arises in certain ranges of the gate voltages used to define the DQD. More importantly, the resulting Fano transport regime appears under a wide range of experimental conditions, as we saw in Figs. 3.6 (a), (b), and (c). It is indeed an interesting experimental finding that such a state can exist robustly, spreading over the entire DQD system to couple the two leads.

3.7 Model calculation

In the previous section, we showed experimentally that transport properties due to the Fano effect are observed under a certain condition of the gate electrode in DQD. We propose that the Fano effect requires the energy continuum originating from the strong coupling between leads. It is also observed that modulation the coupling between QDL and QDR varies the charge stability diagram which is similar to that in a conventional DQD system.

3.7.1 Model and Hamiltonian

Then, we tried to confirm these experimental observations by a calculation based on a simple model. Figure 3.7 shows a schematic of our model. For simplicity, we assumed that (i) only
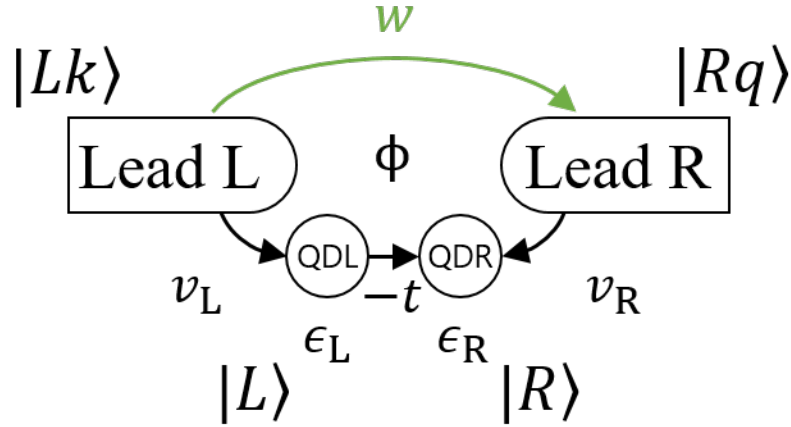

Figure 3.7: The system we considered. It consists of the lateral series of QDs and a direct transition between leads L and R.

single levels in each QD contribute to the transport, and (ii) Coulomb interactions between

QDL and QDR, and inside QDs are negligible. Spin degree of freedom is also neglected. The Hamiltonian of this system $\hat{H}$ is expressed with bra-ket notation as follow.

$$\hat{H} = \hat{H}_0 + \hat{H}_{\mathrm{T}}, \tag{3.4}$$

$$\hat{H}_0 = \hat{H}_{\mathrm{leads}} + \hat{H}_{\mathrm{dots}} \text{ (Hamiltonian of leads and dots without hopping)}, \tag{3.5}$$

$$\hat{H}_{\mathrm{T}} = \hat{H}_{\mathrm{TDL}} + \hat{H}_{\mathrm{TLL}} \text{ (hopping term)}, \tag{3.6}$$

$$\hat{H}_{\mathrm{dots}} = \varepsilon_{\mathrm{L}} |\mathrm{L}\rangle\langle\mathrm{L}| + \varepsilon_{\mathrm{R}} |\mathrm{R}\rangle\langle\mathrm{R}| - t(|\mathrm{R}\rangle\langle\mathrm{L}| + |\mathrm{L}\rangle\langle\mathrm{R}|), \tag{3.7}$$

$$\hat{H}_{\mathrm{leads}} = \Sigma_k \varepsilon_{\mathrm{L}k} |\mathrm{L}k\rangle\langle\mathrm{L}k| + \Sigma_k \varepsilon_{\mathrm{R}q} |\mathrm{R}q\rangle\langle\mathrm{R}q|, \tag{3.8}$$

$$\hat{H}_{\mathrm{TDL}} = \Sigma_{kq} (w |\mathrm{R}q\rangle\langle\mathrm{L}k| + w^* |\mathrm{L}k\rangle\langle\mathrm{R}q|), \tag{3.9}$$

$$\hat{H}_{\mathrm{TLL}} = \Sigma_k (v_{\mathrm{L}} |\mathrm{L}\rangle\langle\mathrm{L}k| + v_{\mathrm{L}}^* |\mathrm{L}k\rangle\langle\mathrm{L}|) + \Sigma_q (v_{\mathrm{R}} |\mathrm{R}\rangle\langle\mathrm{R}q| + v_{\mathrm{R}^*} |\mathrm{R}q\rangle\langle\mathrm{R}|). \tag{3.10}$$

$\hat{H}_0$ consist of the Hamiltonians of the isolated DQD ($\hat{H}_{\mathrm{dots}}$) and the isolated leads ($\hat{H}_{\mathrm{leads}}$). First and second term of $\hat{H}_{\mathrm{dots}}$ describe the energy of isolated QDL and QDR. $\varepsilon_{\mathrm{L(R)}}$ is the eigenvalue of the ground state in QDL(R) $|\mathrm{L(R)}\rangle$. Last term of $\hat{H}_{\mathrm{dots}}$ connects QDL and QDR with hopping integral $-t$. $\hat{H}_{\mathrm{leads}}$ describes the kinetic energy of noninteracting electrons in leads L and R. $\varepsilon_{\mathrm{L}k}$ and $\varepsilon_{\mathrm{R}q}$ are the eigenvalue of state whose wave vector is k and q in Lead L and R, respectively. $\hat{H}_{\mathrm{T}}$ represents the tunneling between leads and DQD ($H_{\mathrm{TDL}}^{\hat{}}$) and direct tunneling between lead L and lead R ($\hat{H}_{\mathrm{TLL}}$). v_{L}, v_{R} and w are the hopping integrals to allow electrons transmit through DQD (v_{L}, v_{R}) and directly (w). The introduction of $\hat{H}_{\mathrm{TDL}}$ has an important role in this model to include the contribution of the strongly coupled state phenomenologically. By defining t as a positive number, we can define the phase ϕ that an elecron acquires while traveling in a circle as

$$w v_{\mathrm{R}} v_{\mathrm{L}}^* = |w| \, |v_{\mathrm{R}}| \, |v_{\mathrm{L}}| \, e^{i\phi}. \tag{3.11}$$

Here, ϕ is 0 or π at zero magnetic field.

3.7.2 What to be calculated

We define retarded and advanced Green functions $\hat{G}_{\pm}(\varepsilon)$ operators as follow.

$$\hat{G}_{\pm}(\varepsilon) = \frac{1}{\varepsilon - \hat{H} \pm i\delta} = \frac{1}{\varepsilon - \hat{H}_0 \pm i\delta - \hat{H}_T}. \tag{3.12}$$

We regard $\hat{H}_T$ as a Hamiltonian representing weak physical perturbation. Let us define retarded and advanced Green functions by non-perturbation Hamiltonian $\hat{H}_0$, $\hat{G}_{\pm}^0(\varepsilon)$ and $\hat{A}$ as

$$\hat{G}_{\pm}^0(\varepsilon) = \frac{1}{\varepsilon - \hat{H}_0 \pm i\delta}, \tag{3.13}$$

$$\hat{A} = \hat{G}_{\pm}(\varepsilon) - \hat{G}_{\pm}^0(\varepsilon). \tag{3.14}$$

$\hat{A}$ can be expressed by $\hat{G}_\pm(\varepsilon)$, $\hat{G}^0_\pm(\varepsilon)$ and $\hat{H}_\mathrm{T}$ as shown below.

$$\hat{G}_\pm(\varepsilon)\left(\varepsilon - \hat{H} \pm i\delta\right) = 1$$

$$\Leftrightarrow \left(\hat{G}^0_\pm(\varepsilon) + \hat{A}\right)\left(\varepsilon - \hat{H} \pm i\delta\right) = 1$$

$$\Leftrightarrow \hat{G}^0_\pm(\varepsilon)\left(\varepsilon - \hat{H}_0 \pm i\delta - \hat{H}_\mathrm{T}\right) + \hat{A}\left(\varepsilon - \hat{H} \pm i\delta\right) = 1$$

$$\Leftrightarrow 1 - \hat{G}^0_\pm(\varepsilon)\hat{H}_\mathrm{T} + \hat{A}\left(\varepsilon - \hat{H} \pm i\delta\right) = 1$$

$$\therefore \quad \hat{A} = \frac{\hat{G}^0_\pm(\varepsilon)\hat{H}_\mathrm{T}}{\left(\varepsilon - \hat{H} \pm i\delta\right)} = \hat{G}^0_\pm(\varepsilon)\hat{H}_T\hat{G}_\pm(\varepsilon). \tag{3.15}$$

Therefore, Green functions $\hat{G}_\pm(\varepsilon)$ can be expanded as

$$\begin{aligned}
\hat{G}_\pm(\varepsilon) &= \hat{G}^0_\pm(\varepsilon) + \hat{A} = \hat{G}^0_\pm(\varepsilon) + \hat{G}^0_\pm(\varepsilon)\hat{H}_\mathrm{T}\hat{G}_\pm(\varepsilon) \\
&= \hat{G}^0_\pm(\varepsilon) + \hat{G}^0_\pm(\varepsilon)\hat{H}_\mathrm{T}\left(\hat{G}^0_\pm(\varepsilon) + \hat{G}^0_\pm(\varepsilon)\hat{H}_\mathrm{T}\hat{G}_\pm(\varepsilon)\right) \\
&= \hat{G}^0_\pm(\varepsilon) + \hat{G}^0_\pm(\varepsilon)\hat{H}_\mathrm{T}\hat{G}^0_\pm(\varepsilon) + \hat{G}^0_\pm(\varepsilon)\hat{H}_\mathrm{T}\hat{G}^0_\pm(\varepsilon)\hat{H}_\mathrm{T}\hat{G}^0_\pm(\varepsilon) + \cdots.
\end{aligned} \tag{3.16}$$

If we introduce T matrix $\hat{T}_\pm(\varepsilon)$

$$\begin{aligned}
\hat{T}_\pm(\varepsilon) &= \hat{H}_\mathrm{T} + \hat{H}_\mathrm{T}\hat{G}^0_\pm(\varepsilon)\hat{H}_\mathrm{T} + \hat{H}_\mathrm{T}\hat{G}^0_\pm(\varepsilon)\hat{H}_\mathrm{T} + \cdots \\
&= \hat{H}_\mathrm{T} + \hat{H}_\mathrm{T}\hat{G}_\pm(\varepsilon)\hat{H}_\mathrm{T},
\end{aligned} \tag{3.17}$$

Green functions can be described as shown.

$$\hat{G}_\pm(\varepsilon) = \hat{G}^0_\pm(\varepsilon) + \hat{G}^0_\pm(\varepsilon)\hat{T}_\pm(\varepsilon)\hat{G}^0_\pm(\varepsilon). \tag{3.18}$$

Equation (3.18) says that even though perturbation expansion Eq. (3.16) is approximated at first order of $\hat{H}_\mathrm{T}$, precise formula is obtained by replacing $\hat{H}_\mathrm{T}$ with $\hat{T}_\pm(\varepsilon)$.

Then let us calculate the transition probability per unit time from $|\mathrm{L}k\rangle$ to $|\mathrm{R}q\rangle$. As discuss above, we calculate the transition probability under the first order approximation and replace $\hat{H}_\mathrm{T}$ with T matrix, and thus get precise formula of the conductance. In this case, T matrix should be $\hat{T}_+(\varepsilon)$ due to the causality. According to Fermi's golden rule, the transition probability $P^{(FG)}_{\mathrm{R}q\leftarrow\mathrm{L}k}$ is expressed as

$$P^{(FG)}_{\mathrm{R}q\leftarrow\mathrm{L}k} = \frac{2\pi}{\hbar}\left|\langle\mathrm{R}q|\hat{H}_\mathrm{T}|\mathrm{L}k\rangle\right|^2 \delta\left(\varepsilon - \varepsilon_{\mathrm{L}k}\right)\delta\left(\varepsilon - \varepsilon_{\mathrm{R}q}\right). \tag{3.19}$$

Then precise formula is

$$P_{\mathrm{R}q\leftarrow\mathrm{L}k} = \int d\varepsilon \frac{2\pi}{\hbar}\left|\langle\mathrm{R}q|\hat{T}_+(\varepsilon)|\mathrm{L}k\rangle\right|^2 \delta\left(\varepsilon - \varepsilon_{\mathrm{L}k}\right)\delta\left(\varepsilon - \varepsilon_{\mathrm{R}q}\right). \tag{3.20}$$

We can also calculate the transition probability per unit time from $|\mathrm{R}q\rangle$ to $|\mathrm{L}k\rangle$ with the same way. These results and the electron charge $-e$ give us the tunnel current from lead L to lead

R I as

$$
\begin{aligned}
I &= (\text{spins}) \times (-e) \times \Sigma_{k,q}\Big(P_{\mathrm{R}q\leftarrow\mathrm{L}k}f_{\mathrm{L}}(\varepsilon_{\mathrm{L}k})\left(1 - f_{\mathrm{R}}(\varepsilon_{\mathrm{R}q})\right) - P_{\mathrm{L}k\leftarrow\mathrm{R}q}f_{\mathrm{R}}(\varepsilon_{\mathrm{R}q})\left(1 - f_{\mathrm{L}}(\varepsilon_{\mathrm{L}k})\right)\Big) \\
&= -2e\Sigma_{k,q}\int d\varepsilon \frac{(2\pi)^2}{h}\delta\left(\varepsilon - \varepsilon_{\mathrm{L}k}\right)\delta\left(\varepsilon - \varepsilon_{\mathrm{R}q}\right) \\
&\quad \times \Big(\left|\langle \mathrm{R}q|\hat{T}_+(\varepsilon)|\mathrm{L}k\rangle\right|^2 f_{\mathrm{L}}(\varepsilon_{\mathrm{L}k})\left(1 - f_{\mathrm{R}}(\varepsilon_{\mathrm{R}q})\right) - \left|\langle \mathrm{L}k|\hat{T}_+(\varepsilon)|\mathrm{R}q\rangle\right|^2 f_{\mathrm{R}}(\varepsilon_{\mathrm{R}q})(1 - f_{\mathrm{L}}(\varepsilon_{\mathrm{L}k}))\Big) \\
&= -\frac{2e}{h}\int d\varepsilon\Big(\Big(\Sigma_{k,q}\left|\langle \mathrm{R}q|\hat{T}_+(\varepsilon)|\mathrm{L}k\rangle\right|^2 2\pi\delta\left(\varepsilon - \varepsilon_{\mathrm{L}k}\right)2\pi\delta\left(\varepsilon - \varepsilon_{\mathrm{R}q}\right)f_{\mathrm{L}}(\varepsilon)\left(1 - f_{\mathrm{R}}(\varepsilon)\right)\Big) \\
&\quad - \Big(\Sigma_{k,q}\left|\langle \mathrm{L}k|\hat{T}_+(\varepsilon)|\mathrm{R}q\rangle\right|^2 2\pi\delta\left(\varepsilon - \varepsilon_{\mathrm{L}k}\right)2\pi\delta\left(\varepsilon - \varepsilon_{\mathrm{R}q}\right)f_{\mathrm{R}}(\varepsilon)(1 - f_{\mathrm{L}}(\varepsilon))\Big)\Big) \\
&= -\frac{2e}{h}\int d\varepsilon\big(\mathcal{T}_{\mathrm{RL}}(\varepsilon)f_{\mathrm{L}}(\varepsilon)\left(1 - f_{\mathrm{R}}(\varepsilon)\right) - \mathcal{T}_{\mathrm{LR}}(\varepsilon)f_{\mathrm{R}}(\varepsilon)(1 - f_{\mathrm{L}}(\varepsilon))\big), \quad\quad (3.21)
\end{aligned}
$$

$$
\text{where} \quad \mathcal{T}_{\mathrm{RL}}(\varepsilon) = \Sigma_{k,q}\left|\langle \mathrm{R}q|\hat{T}_+(\varepsilon)|\mathrm{L}k\rangle\right|^2 2\pi\delta\left(\varepsilon - \varepsilon_{\mathrm{L}k}\right)2\pi\delta\left(\varepsilon - \varepsilon_{\mathrm{R}q}\right). \quad\quad (3.22)
$$

$\mathcal{T}_{\mathrm{RL}}(\varepsilon)$ is transmission probability of electron whose energy is equal to ε from the state $|\mathrm{L}k\rangle$ to the state $|\mathrm{R}q\rangle$. $f_{\mathrm{L(R)}}(\varepsilon_{k(q)})$ is the probability that the state which has the wave vector $k(q)$ and the energy $\varepsilon_{k(q)}$ in lead L (R) is occupied. In this case, it is equal to Fermi distribution function in lead L (R) $f_{\mathrm{L\ (R)}}(\epsilon)$. Fermi distribution function in each lead is defined as

$$
f_{\mathrm{L}}(\varepsilon) = \frac{1}{e^{\beta(\varepsilon - \mu_{\mathrm{L}})} + 1}, f_{\mathrm{R}}(\varepsilon) = \frac{1}{e^{\beta(\varepsilon - \mu_{\mathrm{R}})} + 1}. \quad\quad (3.23)
$$

$\beta = 1/k_B T$ and $\mu_{\mathrm{L\ (R)}}$ are inverse temperature and chemical potential in lead L (R), respectively. In equilibrium ($f_{\mathrm{L}}(\varepsilon) = f_{\mathrm{R}}(\varepsilon)$), the current I must be zero which leads $\mathcal{T}_{\mathrm{RL}}(\varepsilon) = \mathcal{T}_{\mathrm{LR}}(\varepsilon)$. Therefore, the tunnel current I can be simplified as follow.

$$
I = -\frac{2e}{h}\int d\varepsilon\,\mathcal{T}_{\mathrm{RL}}(\varepsilon)\left(f_{\mathrm{L}}(\varepsilon) - f_{\mathrm{R}}(\varepsilon)\right). \quad\quad (3.24)
$$

If I define conventional coefficients and function applied voltage V, chemical potential μ, Fermi distribution function $f(\varepsilon)$ as

$$
-eV = \mu_{\mathrm{L}} - \mu_{\mathrm{R}}, \mu = \frac{\mu_{\mathrm{L}} - \mu_{\mathrm{R}}}{2}, \ \ f(\varepsilon) = \frac{1}{e^{\beta(\varepsilon - \mu)} + 1}, \quad\quad (3.25)
$$

the conductance G can be described as

$$
G(\mu) = \lim_{V\to 0} I/V = \frac{2e^2}{h}\int d\varepsilon\,\mathcal{T}_{\mathrm{RL}}(\varepsilon)\left(-\frac{df}{d\varepsilon}\right). \quad\quad (3.26)
$$

At zero temperature, because $\left(-\frac{df}{d\varepsilon}\right)$ goes delta function $\delta(\varepsilon - \varepsilon_f)$ (ε_f is Fermi energy), the conductance G goes to

$$
G(\varepsilon_f) = \frac{2e}{h}\mathcal{T}_{\mathrm{RL}}(\varepsilon_f), \qu\quad\quad (3.27)
$$

which is the same to spin less Landauer formula.

3.7.3 Green functions

In order to calculate Eq. (3.22), let us calculate Green functions. Green functions are calculated by solving

$$(\varepsilon - \hat{H} \pm i\delta)\hat{G}_\pm(\varepsilon) = 1. \tag{3.28}$$

The way to solve this is the production of $|\alpha\rangle$ ($\alpha =$L or R) from right and insert completeness

$$|L\rangle\langle L| + |R\rangle\langle R| + \Sigma_k |Lk\rangle\langle Lk| + \Sigma_q |Rq\rangle\langle Rq| = 1 \tag{3.29}$$

between $(\varepsilon - \hat{H} \pm i\delta)$ and $\hat{G}_\pm(\varepsilon)$. We get

$$(\varepsilon - \hat{H} \pm i\delta)\left(|L\rangle\langle L| + |R\rangle\langle R| + \Sigma_k |Lk\rangle\langle Lk| + \Sigma_q |Rq\rangle\langle Rq|\right)\hat{G}_\pm(\varepsilon)|\alpha\rangle = |\alpha\rangle. \tag{3.30}$$

Production of $\langle L|$, $\langle R|$, $\langle Lk|$, and $\langle Rq|$ from left give us

$$(\varepsilon - \varepsilon_\mathrm{L} \pm i\delta)\langle L|\hat{G}_\pm(\varepsilon)|\alpha\rangle + t\langle R|\hat{G}_\pm(\varepsilon)|\alpha\rangle - v_\mathrm{L}\Sigma_k \langle Lk|\hat{G}_\pm(\varepsilon)|\alpha\rangle = \delta_{\mathrm{L}\alpha}, \tag{3.31}$$

$$(\varepsilon - \varepsilon_\mathrm{R} \pm i\delta)\langle R|\hat{G}_\pm(\varepsilon)|\alpha\rangle + t\langle L|\hat{G}_\pm(\varepsilon)|\alpha\rangle - v_\mathrm{R}\Sigma_q \langle Rq|\hat{G}_\pm(\varepsilon)|\alpha\rangle = \delta_{\mathrm{R}\alpha}, \tag{3.32}$$

$$(\varepsilon - \varepsilon_{\mathrm{L}k} \pm i\delta)\langle Lk|\hat{G}_\pm(\varepsilon)|\alpha\rangle - w^*\Sigma_q \langle Rq|\hat{G}_\pm(\varepsilon)|\alpha\rangle - v_\mathrm{L}^* \langle L|\hat{G}_\pm(\varepsilon)|\alpha\rangle = 0, \tag{3.33}$$

$$(\varepsilon - \varepsilon_{\mathrm{R}q} \pm i\delta)\langle Rq|\hat{G}_\pm(\varepsilon)|\alpha\rangle - w\Sigma_k \langle Lk|\hat{G}_\pm(\varepsilon)|\alpha\rangle - v_\mathrm{R}^* \langle R|\hat{G}_\pm(\varepsilon)|\alpha\rangle = 0. \tag{3.34}$$

Here, density of states in each lead are approximated by constants

$$D_\mathrm{L}(\varepsilon) = \Sigma_k\delta(\varepsilon - \varepsilon_{\mathrm{L}k}) \simeq D_\mathrm{L}, \quad D_\mathrm{R}(\varepsilon) = \Sigma_q\delta(\varepsilon - \varepsilon_{\mathrm{R}q}) \simeq D_\mathrm{R}. \tag{3.35}$$

Thanks to this approximation, some summations are estimated as follow.

$$\begin{aligned}
\Sigma_k\frac{1}{\varepsilon - \varepsilon_{\mathrm{L}k} \pm i\delta} &= \int_{\text{all bands}} d\varepsilon'\frac{D(\varepsilon')}{\varepsilon - \varepsilon' \pm i\delta} \simeq D_\mathrm{L} \int_{\text{all bands}} d\epsilon'\left(\frac{\varepsilon - \varepsilon'}{(\varepsilon - \varepsilon')^2 + \delta^2} \mp i\frac{\delta}{(\varepsilon - \varepsilon')^2 + \delta^2}\right) \\
&\simeq D_\mathrm{L} \int_{-\infty}^{+\infty} d\epsilon'\left(\frac{\varepsilon - \varepsilon'}{(\varepsilon - \varepsilon')^2 + \delta^2} \mp i\frac{\delta}{(\varepsilon - \varepsilon')^2 + \delta^2}\right) = \mp i\pi D_\mathrm{L}, \tag{3.36}
\end{aligned}$$

$$\Sigma_q\frac{1}{\varepsilon - \varepsilon_{\mathrm{R}q} \pm i\delta} \simeq \mp i\pi D_\mathrm{R}. \tag{3.37}$$

Equation (3.33) and Eq. (3.34) can be transformed by

$$\Sigma_k \langle Lk|\hat{G}_\pm(\varepsilon)|\alpha\rangle \pm i\pi D_\mathrm{L}w^*\Sigma_q \langle Rq|\hat{G}_\pm(\varepsilon)|\alpha\rangle \pm i\pi D_\mathrm{L}v_\mathrm{L} \langle L|\hat{G}_\pm(\varepsilon)|\alpha\rangle = 0, \text{and} \tag{3.38}$$

$$\Sigma_q \langle Rq|\hat{G}_\pm(\varepsilon)|\alpha\rangle \pm i\pi D_\mathrm{R}w\Sigma_k \langle Lk|\hat{G}_\pm(\varepsilon)|\alpha\rangle \pm i\pi D_\mathrm{R}v_\mathrm{R} \langle R|\hat{G}_\pm(\varepsilon)|\alpha\rangle = 0. \tag{3.39}$$

Solving this simultaneous equation yields the following.

$$\begin{aligned}
v_\mathrm{L}\Sigma_k \langle Lk|\hat{G}_\pm(\varepsilon)|\alpha\rangle &= \frac{\mp i\pi D_\mathrm{L}|v_\mathrm{L}|^2 \langle L|\hat{G}_\pm(\varepsilon)|\alpha\rangle - \pi^2 D_\mathrm{L}D_\mathrm{R}w^*v_\mathrm{L}v_\mathrm{R}^* \langle R|\hat{G}_\pm(\varepsilon)|\alpha\rangle}{1 + \pi^2 D_\mathrm{L}D_\mathrm{R}|w|^2} \\
&= \mp i\tilde{\Gamma}_\mathrm{L} \langle L|\hat{G}_\pm(\varepsilon)|\alpha\rangle - \lambda\tilde{\Gamma}_\mathrm{LR}e^{-i\phi} \langle R|\hat{G}_\pm(\varepsilon)|\alpha\rangle \text{ and} \tag{3.40} \\
v_\mathrm{R}\Sigma_q \langle Rq|\hat{G}_\pm(\varepsilon)|\alpha\rangle &= \frac{-\pi^2 D_\mathrm{L}D_\mathrm{R}wv_\mathrm{L}^*v_\mathrm{R} \langle L|\hat{G}_\pm(\varepsilon)|\alpha\rangle \mp i\pi D_\mathrm{R}|v_\mathrm{R}|^2 \langle R|\hat{G}_\pm(\varepsilon)|\alpha\rangle}{1 + \pi^2 D_\mathrm{L}D_\mathrm{R}|w|^2} \\
&= -\lambda\tilde{\Gamma}_\mathrm{LR}e^{+i\phi} \langle L|\hat{G}_\pm(\varepsilon)|\alpha\rangle \mp i\tilde{\Gamma}_\mathrm{R} \langle R|\hat{G}_\pm(\varepsilon)|\alpha\rangle. \tag{3.41}
\end{aligned}$$

Here we defined several convenient coefficient as

$$\Gamma_\alpha = \pi D_\alpha |v_\alpha|^2, \Gamma_{\text{LR}} = \sqrt{\Gamma_L \Gamma_R}, \lambda = \pi \sqrt{D_L D_R} |w|, \tilde{\Gamma}_\alpha = \frac{\Gamma_\alpha}{1 + \lambda^2}, \tilde{\Gamma}_{\text{LR}} = \frac{\Gamma_{\text{LR}}}{1 + \lambda^2}. \quad (3.42)$$

Let us introduce Green functions projected into $|L\rangle$ and $|R\rangle$ space $\hat{g}_\pm(\varepsilon)$, and self-energy $\hat{\Sigma}_\pm$ taking Hamiltonian of leads into $|L\rangle$ and $|R\rangle$ space as follow.

$$\hat{g}_\pm(\varepsilon) = \hat{P}\hat{G}_\pm(\varepsilon)\hat{P}, \qquad \text{where } \hat{P} = |L\rangle\langle L| + |R\rangle\langle R|. \quad (3.43)$$

$$\left(\varepsilon - \hat{H}_{\text{dots}} \pm i\delta - \hat{\Sigma}_\pm\right)\hat{g}_\pm(\varepsilon) = \hat{P}. \quad (3.44)$$

To satisfy Eq. (3.31), Eq. (3.32), Eq. (3.40), and Eq. (3.41), $\hat{\Sigma}_\pm$ must be

$$\hat{\Sigma}_\pm = \mp i\tilde{\Gamma}_L |L\rangle\langle L| - \lambda\tilde{\Gamma}_{\text{LR}} e^{-i\phi} |L\rangle\langle R| - \lambda\tilde{\Gamma}_{\text{LR}} e^{+i\phi} |R\rangle\langle L| \mp i\tilde{\Gamma}_R |R\rangle\langle R| \quad (3.45)$$

Since imaginary part of Eq. (3.45) is large enough, we can neglect δ in Eq. (3.44). The projected Green function $\hat{g}_\pm(\varepsilon)$ is expressed by 2×2 matrix which $|L\rangle$ and $|R\rangle$ correspond to $\begin{pmatrix} 1 \\ 0 \end{pmatrix}$ and $\begin{pmatrix} 0 \\ 1 \end{pmatrix}$, respectively. It is calculated as

$$
\begin{aligned}
\hat{g}_\pm(\varepsilon) &= \left(\varepsilon - \hat{H}_{\text{dots}} - \hat{\Sigma}_\pm\right)^{-1} = \begin{pmatrix} \varepsilon - \varepsilon_L \pm i\tilde{\Gamma}_L & t + \lambda\tilde{\Gamma}_{\text{LR}} e^{-i\phi} \\ t + \lambda\tilde{\Gamma}_{\text{LR}} e^{+i\phi} & \varepsilon - \varepsilon_R \pm i\tilde{\Gamma}_R \end{pmatrix}^{-1} \\
&= \frac{1}{M_\pm(\varepsilon)} \begin{pmatrix} \varepsilon - \varepsilon_R \pm i\tilde{\Gamma}_R & -t - \lambda\tilde{\Gamma}_{\text{LR}} e^{-i\phi} \\ -t - \lambda\tilde{\Gamma}_{\text{LR}} e^{+i\phi} & \varepsilon - \varepsilon_L \pm i\tilde{\Gamma}_L \end{pmatrix}, \quad (3.46)
\end{aligned}
$$

$$
\begin{aligned}
\text{where} \quad M_\pm &= det(\varepsilon - \hat{H}_{\text{dots}} - \hat{\Sigma}_\pm) \\
&= (\varepsilon - \varepsilon_L \pm i\tilde{\Gamma}_L)(\varepsilon - \varepsilon_R \pm i\tilde{\Gamma}_R) - t^2 - \lambda^2\tilde{\Gamma}_{\text{LR}}^2 - 2t\tilde{\Gamma}_{\text{LR}} \cos\phi. \quad (3.47)
\end{aligned}
$$

Let us calculate $\langle L|\hat{\Sigma}_\pm \hat{g}_\pm(\varepsilon)|\alpha\rangle$ and $\langle R|\hat{\Sigma}_\pm \hat{g}_\pm(\varepsilon)|\alpha\rangle$ for the predicted calculations.

$$
\begin{aligned}
\langle L|\hat{\Sigma}_\pm \hat{g}_\pm(\varepsilon)|\alpha\rangle &= \langle L|\hat{\Sigma}_\pm \hat{P}\hat{G}_\pm(\varepsilon)\hat{P}|\alpha\rangle = \mp i\tilde{\Gamma}_L \langle L|\tilde{G}_\pm(\varepsilon)|\alpha\rangle - \lambda\tilde{\Gamma}_{\text{LR}} e^{-i\phi} \langle R|\tilde{G}_\pm|\alpha\rangle \\
&= v_L \Sigma_k \langle Lk|\hat{G}_\pm(\varepsilon)|\alpha\rangle. \quad (3.48)
\end{aligned}
$$

$$\langle R|\hat{\Sigma}_\pm \hat{g}_\pm(\varepsilon)|\alpha\rangle = v_R \Sigma_q \langle Rq|\hat{G}_\pm(\varepsilon)|\alpha\rangle. \quad (3.49)$$

The complex conjugate of them leads (note that $\hat{G}_\pm^\dagger = \hat{G}_\mp$ and $\hat{\Sigma}_\pm^\dagger = \hat{\Sigma}_\mp$)

$$\langle L|\hat{\Sigma}_\pm \hat{g}_\pm(\varepsilon)|\alpha\rangle = v_L^* \Sigma_k \langle \alpha|\hat{G}_\pm(\varepsilon)|Lk\rangle, \langle \alpha|\hat{\Sigma}_\pm \hat{g}_\pm(\varepsilon)|R\rangle = v_R^* \Sigma_q \langle \alpha|\hat{G}_\pm(\varepsilon)|Rq\rangle. \quad (3.50)$$

Then, let us product $|Lk\rangle$ from right and $\langle Rq|$ from left, insert completeness [Eq. (3.29)] between $(\varepsilon - \hat{H} \pm i\delta)$ and $\hat{G}_\pm$, and summation with k for Eq. (3.28). We obtain

$$(\varepsilon - \varepsilon_R \pm i\delta)\Sigma_k \langle R|\hat{G}_\pm(\varepsilon)|Lk\rangle + t\Sigma_k \langle L|\hat{G}_\pm(\varepsilon)|Lk\rangle - v_R \Sigma_{k,q} \langle Rq|\hat{G}_\pm(\varepsilon)|Lk\rangle = 0. \quad (3.51)$$

The complex conjugate of Eq. (3.51) yields

$$
\begin{aligned}
\Sigma_{k,q}\,\langle \mathrm{L}k|\hat{G}_{\pm}(\varepsilon)|\mathrm{R}q\rangle
&= \frac{1}{v_{\mathrm{L}}v_{\mathrm{R}}^{*}}\left(v_{\mathrm{L}}\Sigma_{k}\,\langle \mathrm{L}|\hat{G}_{\pm}(\varepsilon)|\mathrm{R}\rangle\,(\varepsilon-\varepsilon_{\mathrm{R}}\pm i\delta)+v_{\_}\mathrm{L}\Sigma_{k}\,\langle \mathrm{L}k|\hat{G}_{\pm}|\mathrm{L}\rangle\,t\right) \\
&= \frac{1}{v_{\mathrm{L}}v_{\mathrm{R}}^{*}}\left(\langle \mathrm{L}|\hat{\Sigma}_{\pm}\hat{g}_{\pm}(\varepsilon)(\varepsilon-\varepsilon_{\mathrm{R}}\pm i\delta)|\mathrm{R}\rangle+\langle \mathrm{L}|\hat{\Sigma}_{\pm}\hat{g}_{\pm}(\varepsilon)t|\mathrm{L}\rangle\right) \qquad [\cdots\text{Eq. (3.48)}] \\
&= \frac{1}{v_{\mathrm{L}}v_{\mathrm{R}}^{*}}\left(\langle \mathrm{L}|\hat{\Sigma}_{\pm}\hat{g}_{\pm}(\varepsilon)(\varepsilon-\hat{H}_{\mathrm{dots}}\pm i\delta)|\mathrm{R}\rangle\right) \\
&= \frac{1}{v_{\mathrm{L}}v_{\mathrm{R}}^{*}}\left(\langle \mathrm{L}|\hat{\Sigma}_{\pm}\hat{g}_{\pm}(\varepsilon)\left(\hat{g}_{\pm}^{-1}(\varepsilon)+\hat{\Sigma}_{\pm}\right)|\mathrm{R}\rangle\right) \qquad [\cdots\text{Eq. (3.43)}] \\
&= \frac{1}{v_{\mathrm{L}}v_{\mathrm{R}}^{*}}\,\langle \mathrm{L}|\hat{\Sigma}_{\pm}+\hat{\Sigma}_{\pm}\hat{g}_{\pm}(\epsilon)\hat{\Sigma}_{\pm}|\mathrm{R}\rangle\,.
\end{aligned}
\tag{3.52}
$$

3.7.4 T matrix

Finally, we calculate the transmission probability [Eq. (3.22)]. According to Eq. (3.18), $\langle \mathrm{R}q|\hat{T}_{+}(\varepsilon)|\mathrm{L}k\rangle$ of Eq. (3.22) is extracted by

$$
\begin{aligned}
\langle \mathrm{R}q|\hat{T}_{+}(\varepsilon)|\mathrm{L}k\rangle
&= \langle \mathrm{R}q|\hat{H}_{\mathrm{T}}+\hat{H}_{\mathrm{T}}\hat{G}_{+}(\varepsilon)\hat{H}_{\mathrm{T}}|\mathrm{L}k\rangle \\
&= w+w^{2}\Sigma_{k,q}\,\langle \mathrm{L}k|\hat{G}_{+}(\varepsilon)|\mathrm{R}q\rangle+wv_{\mathrm{L}}\Sigma_{k}\,\langle \mathrm{L}k|\hat{G}_{+}(\varepsilon)|\mathrm{L}\rangle \\
&\quad +v_{\mathrm{R}}^{*}w\Sigma_{k}\,\langle \mathrm{R}|\hat{G}_{+}(\varepsilon)|\mathrm{R}q\rangle+v_{\mathrm{R}}^{*}v_{\mathrm{L}}\,\langle \mathrm{R}|\hat{G}_{+}(\varepsilon)|\mathrm{R}\rangle\,.
\end{aligned}
\tag{3.53}
$$

Using Eq. (3.52), Eq. (3.48), Eq. (3.49), Eq. (3.50),

$$
v_{\mathrm{R}}^{*}v_{\mathrm{L}}=w\frac{1+\lambda^{2}}{\lambda}\tilde{\Gamma}_{\mathrm{LR}}e^{-i\phi}=-w\frac{1+\lambda^{2}}{\lambda^{2}}\,\langle \mathrm{L}|\hat{\Sigma}_{+}|\mathrm{R}\rangle
\tag{3.54}
$$

$$
\text{and}\ \langle \mathrm{L}|\hat{\Sigma}_{+}|\mathrm{L}\rangle\,\langle \mathrm{R}|\hat{\Sigma}_{+}|\mathrm{R}\rangle=-\frac{1}{\lambda^{2}}\,\langle \mathrm{L}|\hat{\Sigma}_{+}|\mathrm{R}\rangle\,\langle \mathrm{R}|\hat{\Sigma}_{+}|\mathrm{L}\rangle\,,
\tag{3.55}
$$

let us calculate each term of Eq. (3.53).

$$
\begin{aligned}
w^{2}\Sigma_{k,q}\,\langle \mathrm{L}k|\hat{G}_{+}(\varepsilon)|\mathrm{R}q\rangle
&= \frac{w^{2}}{v_{\mathrm{L}}v_{\mathrm{R}}^{*}}\,\langle \mathrm{L}|\hat{\Sigma}_{\pm}+\hat{\Sigma}_{\pm}\hat{g}_{\pm}(\epsilon)\hat{\Sigma}_{\pm}|\mathrm{R}\rangle=-\frac{\lambda^{2}w}{1+\lambda^{2}}\frac{\langle \mathrm{L}|\hat{\Sigma}_{+}|\mathrm{R}\rangle+\langle \mathrm{L}|\hat{\Sigma}_{+}\hat{g}_{+}\hat{\Sigma}_{+}|\mathrm{R}\rangle}{\langle \mathrm{L}|\hat{\Sigma}_{+}|\mathrm{R}\rangle} \\
&= -\frac{\lambda^{2}w}{1+\lambda^{2}}\left(1+\frac{\langle \mathrm{L}|\hat{\Sigma}_{+}\left(|\mathrm{L}\rangle\langle \mathrm{L}|+|\mathrm{R}\rangle\langle \mathrm{R}|+\Sigma_{k}|\mathrm{L}k\rangle\langle \mathrm{L}k|+\Sigma_{q}|\mathrm{R}q\rangle\langle \mathrm{R}q|\right)\hat{g}_{+}\hat{\Sigma}_{+}|\mathrm{R}\rangle}{\langle \mathrm{L}|\hat{\Sigma}_{+}|\mathrm{R}\rangle}\right) \\
&= -\frac{\lambda^{2}w}{1+\lambda^{2}}\left(1+\langle \mathrm{R}|\hat{g}_{\pm}(\epsilon)\hat{\Sigma}_{\pm}|\mathrm{R}\rangle+\frac{\langle \mathrm{L}|\hat{\Sigma}_{+}|\mathrm{L}\rangle\,\langle \mathrm{L}|\hat{g}_{+}(\varepsilon)\left(|\mathrm{L}\rangle\langle \mathrm{L}|+|\mathrm{R}\rangle\langle \mathrm{R}|\right)\hat{\Sigma}_{+}|\mathrm{R}\rangle}{\langle \mathrm{L}|\hat{\Sigma}_{+}|\mathrm{R}\rangle}\right) \\
&= -\frac{\lambda^{2}w}{1+\lambda^{2}}\left(1+\langle \mathrm{R}|\hat{g}_{\pm}(\epsilon)\hat{\Sigma}_{\pm}|\mathrm{R}\rangle+\langle \mathrm{L}|\hat{\Sigma}_{+}|\mathrm{L}\rangle\,\langle \mathrm{L}|\hat{g}_{+}(\varepsilon)|\mathrm{L}\rangle+\frac{\langle \mathrm{L}|\hat{\Sigma}_{+}|\mathrm{L}\rangle\,\langle \mathrm{R}|\hat{\Sigma}_{+}|\mathrm{R}\rangle\,\langle \mathrm{L}|\hat{g}_{+}(\varepsilon)|\mathrm{R}\rangle}{\langle \mathrm{L}|\hat{\Sigma}_{+}|\mathrm{R}\rangle}\right) \\
&= -\frac{\lambda^{2}w}{1+\lambda^{2}}\left(1+\langle \mathrm{R}|\hat{g}_{\pm}(\epsilon)\hat{\Sigma}_{\pm}|\mathrm{R}\rangle+\langle \mathrm{L}|\hat{\Sigma}_{+}|\mathrm{L}\rangle\,\langle \mathrm{L}|\hat{g}_{+}(\varepsilon)|\mathrm{L}\rangle\right)+\frac{w}{1+\lambda^{2}}\,\langle \mathrm{L}|\hat{g}_{+}(\varepsilon)|\mathrm{R}\rangle\,\langle \mathrm{R}|\hat{\Sigma}_{+}|\mathrm{L}\rangle\,,
\end{aligned}
\tag{3.56}
$$

$$wv_{\mathrm{L}}\Sigma_k \langle \mathrm{L}k|\hat{G}_+(\varepsilon)|\mathrm{L}\rangle = w\langle \mathrm{L}|\hat{\Sigma}_+\hat{g}_+(\varepsilon)|\mathrm{L}\rangle$$
$$= w\big(\langle \mathrm{L}|\hat{\Sigma}_+|\mathrm{L}\rangle \langle \mathrm{L}|\hat{g}_+(\varepsilon)|\mathrm{L}\rangle + \langle \mathrm{L}|\hat{\Sigma}_+|\mathrm{R}\rangle \langle \mathrm{R}|\hat{g}_+(\varepsilon)|\mathrm{L}\rangle\big), \quad (3.57)$$

$$v_{\mathrm{R}}^* w\Sigma_k \langle \mathrm{R}|\hat{G}_+(\varepsilon)|\mathrm{R}q\rangle = w\langle \mathrm{R}|\hat{g}_+(\varepsilon)\hat{\Sigma}_+|\mathrm{R}\rangle, \quad (3.58)$$

$$v_{\mathrm{R}}^* v_{\mathrm{L}} \langle \mathrm{R}|\hat{G}_+(\varepsilon)|\mathrm{R}\rangle = v_{\mathrm{R}}^* v_{\mathrm{L}} \langle \mathrm{R}|\hat{g}_+(\varepsilon)|\mathrm{L}\rangle = \frac{v_{\mathrm{R}}^* v_{\mathrm{L}}}{1+\lambda^2} \langle \mathrm{R}|\hat{g}_+(\varepsilon)|\mathrm{L}\rangle + \frac{\lambda^2 v_{\mathrm{R}}^* v_{\mathrm{L}}}{1+\lambda^2} \langle \mathrm{R}|\hat{g}_+(\varepsilon)|\mathrm{L}\rangle$$
$$= \frac{w\tilde{\Gamma}_{\mathrm{LR}}e^{-i\phi}}{\lambda} \langle \mathrm{R}|\hat{g}_+(\varepsilon)|\mathrm{L}\rangle - w\langle \mathrm{L}|\hat{\Sigma}_+|\mathrm{R}\rangle \langle \mathrm{R}|\hat{g}_+(\varepsilon)|\mathrm{L}\rangle. \quad (3.59)$$

Finally, $\langle \mathrm{R}q|\hat{T}_+(\varepsilon)|\mathrm{L}k\rangle$ of Eq. (3.22) is calculated as

$$\langle \mathrm{R}q|\hat{T}_+(\varepsilon)|\mathrm{L}k\rangle = \underline{w} - \frac{\lambda^2 w}{1+\lambda^2}\left(\underline{1} + \underset{\sim\sim\sim\sim}{\langle \mathrm{R}|\hat{g}_+(\epsilon)\hat{\Sigma}_+|\mathrm{R}\rangle} + \underline{\underline{\langle \mathrm{L}|\hat{\Sigma}_+|\mathrm{L}\rangle \langle \mathrm{L}|\hat{g}_+(\varepsilon)|\mathrm{L}\rangle}}\right)$$
$$+ \frac{w}{1+\lambda^2}\langle \mathrm{L}|\hat{g}_+(\varepsilon)|\mathrm{R}\rangle \langle \mathrm{R}|\hat{\Sigma}_+|\mathrm{L}\rangle + \underline{\underline{w\langle \mathrm{L}|\hat{\Sigma}_+|\mathrm{L}\rangle \langle \mathrm{L}|\hat{g}_+(\varepsilon)|\mathrm{L}\rangle}}$$
$$+ w\cancel{\langle \mathrm{L}|\hat{\Sigma}_+|\mathrm{R}\rangle \langle \mathrm{R}|\hat{g}_+(\varepsilon)|\mathrm{L}\rangle} + \underset{\sim\sim\sim\sim}{w\langle \mathrm{R}|\hat{g}_+(\varepsilon)\hat{\Sigma}_+|\mathrm{R}\rangle}$$
$$+ \frac{w\tilde{\Gamma}_{\mathrm{LR}}e^{-i\phi}}{\lambda}\langle \mathrm{R}|\hat{g}_+(\varepsilon)|\mathrm{L}\rangle - w\cancel{\langle \mathrm{L}|\hat{\Sigma}_+|\mathrm{R}\rangle \langle \mathrm{R}|\hat{g}_+(\varepsilon)|\mathrm{L}\rangle}$$
$$= \frac{w}{1+\lambda^2} + \underset{\sim\sim\sim\sim}{\frac{w}{1+\lambda^2}\langle \mathrm{R}|\hat{g}_+(\epsilon)\hat{\Sigma}_+|\mathrm{R}\rangle} + \underline{\underline{\frac{w}{1+\lambda^2}\langle \mathrm{L}|\hat{\Sigma}_+|\mathrm{L}\rangle \langle \mathrm{L}|\hat{g}_+(\varepsilon)|\mathrm{L}\rangle}}$$
$$+ \frac{w}{1+\lambda^2}\langle \mathrm{L}|\hat{g}_+(\varepsilon)|\mathrm{R}\rangle \langle \mathrm{R}|\hat{\Sigma}_+|\mathrm{L}\rangle + \frac{w\Gamma_{\mathrm{LR}}e^{-i\phi}}{\lambda}\langle \mathrm{R}|\hat{g}_+(\varepsilon)|\mathrm{L}\rangle$$
$$= \frac{w}{1+\lambda^2}\left(1 + \mathrm{Tr}\big(\hat{g}_+(\epsilon)\hat{\Sigma}_+\big) + \frac{\Gamma_{\mathrm{LR}}e^{-i\phi}}{\lambda}\langle \mathrm{R}|\hat{g}_+(\varepsilon)|\mathrm{L}\rangle\right). \quad (3.60)$$

Note that $|\mathrm{L}\rangle\langle \mathrm{L}| + |\mathrm{R}\rangle\langle \mathrm{R}| = 1$ since $\hat{\Sigma}_+$ and $\hat{g}_+(\varepsilon)$ are functions in $|\mathrm{L}\rangle$ and $|\mathrm{R}\rangle$ space. Because Eq. (3.60) has no wave vector k, q dependence, the transmission probability $\mathcal{T}_{\mathrm{RL}}(\varepsilon)$ is calculated as

$$\mathcal{T}_{\mathrm{RL}}(\varepsilon) = \Sigma_{k,q}\left|\langle \mathrm{R}q|\hat{T}_+(\varepsilon)|\mathrm{L}k\rangle\right|^2 \cdot 2\pi\delta(\varepsilon - \varepsilon_{\mathrm{L}k}) \cdot 2\pi\delta(\varepsilon - \varepsilon_{\mathrm{R}q})$$
$$= \left|\langle \mathrm{R}q|\hat{T}_+(\varepsilon)|\mathrm{L}k\rangle\right|^2 \cdot 2\pi D_{\mathrm{L}} \cdot 2\pi D_{\mathrm{R}}$$
$$= \frac{4\overbrace{\pi^2 w^2 D_{\mathrm{L}} D_{\mathrm{R}}}^{\lambda^2}}{(1+\lambda^2)^2}\left|1 + \mathrm{Tr}\big(\hat{g}_+(\epsilon)\hat{\Sigma}_+\big) + \frac{\Gamma_{\mathrm{LR}}e^{-i\phi}}{\lambda}\langle \mathrm{R}|\hat{g}_+(\varepsilon)|\mathrm{L}\rangle\right|^2$$
$$= \frac{4}{(1+\lambda^2)^2}\left|\lambda e^{+i\phi}\big(1 + \mathrm{Tr}\big(\hat{g}_+(\epsilon)\hat{\Sigma}_+\big)\big) + \Gamma_{\mathrm{LR}}\langle \mathrm{R}|\hat{g}_+(\varepsilon)|\mathrm{L}\rangle\right|^2. \quad (3.61)$$

The zero-bias conductance is given by $\frac{2e^2}{h}\mathcal{T}_{RL}(\epsilon_{\mathrm{F}})$, where ϵ_{F} is the Fermi energy. This equation is consistent with Eq. (12) in Ref. [72] when we calculate the conductance of a conventional DQD that has a symmetric dot-lead coupling, namely, $\Gamma_{\mathrm{L}} = \Gamma_{\mathrm{R}}$ and $\lambda = 0$ in Eq. (3.61).
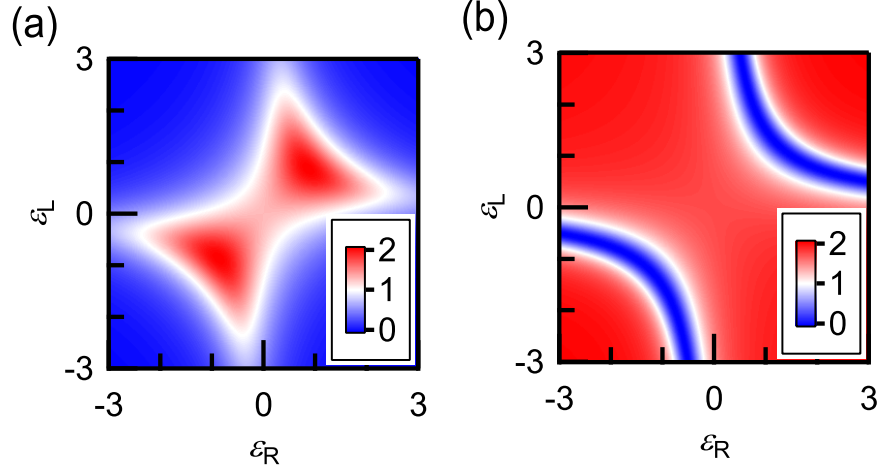
Figure 3.8: ϵ_R and ϵ_L dependence of the conductance G. Unit of energy is t. We set $\Gamma_L = \Gamma_R = 0.5t$ and $\phi = 0$. (a) The esult for $\lambda = 0$, that is, for a conventional DQD system. The triple point, which is characteristic of the DQD system, is reproduced. (b) The esult for $\lambda = 1$, that is, for a DQD system showing the Fano effect. Anti-crossing lines appear as a dip in the conductance.

Figures 3.8 (a) and 3.8(b) show intensity plots of the conductance as functions of ϵ_L and ϵ_R for $\Gamma_L = \Gamma_R = 0.5t$ and $\phi = 0$. We take t as the unit of energy, and the energy ϵ_L and ϵ_R are taken to originate from the Fermi energy. Figure 3.8 (a) is the result for $\lambda = 0$, which corresponds to the conventional DQD case, where the charge transition lines appear as the conductance peak, and the so-called triple points peculiar to the DQD are reproduced. Figure 3.8 (b) shows the calculated transport in the DQD system for $\lambda = 1$, where, in contrast to the former case, the Fano effect is observed. As shown in this plot, the anticrossing lines appear as a dip in the conductance, the signature of this effect. Thus, we developed a minimum model that can simulate our experimental result; the derived formula can reproduce both conventional DQD transport and Fano transport.

The charge transition lines correspond to the bonding and antibonding states formed by a discrete level in QDL and QDR. The energies of the bonding state, ϵ_B, and the anti-bonding state, ϵ_A, are calculated from the condition $M_+(\epsilon) = 0$ in Eq. (3.47). The minimum energy difference $\Delta\epsilon$ between these two states is

$$\Delta\epsilon = \sqrt{(1 + 4\lambda^2)\tilde{\Gamma}_{LR}^2 + 4|t|^2 + 8t\lambda\tilde{\Gamma}_{LR}\cos\phi}, \tag{3.62}$$

where ϵ_L and ϵ_R are equal to the Fermi energy, $\epsilon_L = \epsilon_R = 0$. When $\Gamma_L = \Gamma_R = 0$ and $\lambda = 0$, $\Delta\epsilon$ equals $2|t|$, which is consistent with Eq. (22) in Ref. [34] at $\epsilon_L = \epsilon_R = 0$. For a finite λ, $\Delta\epsilon$ depends on how the energy continuum couples to the discrete levels.

Because we could not derive Fano's asymmetric parameter by deformation of Eq. (3.61), we tried to understand the calculation result Eq. (3.61) by changing various parameters. Figure 3.9 shows various parameters dependence of the conductance as a function of ϵ_R at $\epsilon_L = 2t$.
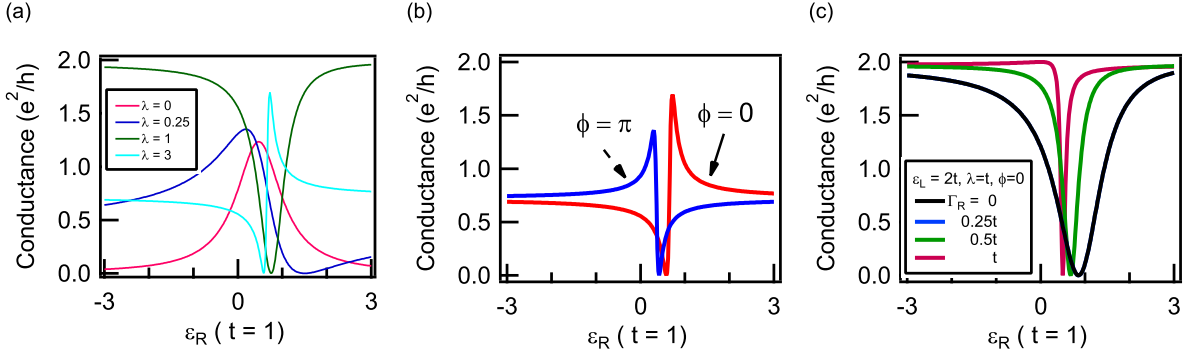
Figure 3.9: Parameters dependence of the conductance as a function of ϵ_R at $\epsilon_L = 2t$. (a) The strength of the direct transition between leads λ dependence of the conductance as a function of ϵ_R when Γ_L and Γ_R equal to $0.5t$. (b) The phase dependence of the conductance as a function of ϵ_R when Γ_L and Γ_R equal to $0.5t$ at $\lambda = 3$. (c) Γ_R dependence of the conductance as a function of ϵ_R when λ and ϕ are 1 and 0, respectively.

Figure 3.9 (a) shows the strength of the direct transition between leads λ dependence of the conductance as a function of ϵ_R when Γ_L and Γ_R equal to 0.5t. Each lines of ϵ_R dependence of the conductance in Fig. 3.9 (a) has a different direct transition probability between leads λ each other. When λ equals to 0, the system is conventional DQD whose Fano's asymmetric parameter equals to ∞. Therefore, there is no dip caused by the Fano effect. The asymmetric structures are observed at $\lambda \neq 0$ due to the Fano effect. It is found that the Fano's asymmetric parameter of the line shape at $\lambda = 1$ is equal to 0. This result shows the Fano's asymmetric parameter of Eq. (3.61) is controlled by λ. Figure 3.9 (b) shows the phase dependence of the conductance as a function of ϵ_R when Γ_L and Γ_R equal to $0.5t$ at $\lambda = 3$. It is found that the phase shift of π changes the intensity of the peak and the order of the peak and dip. The phase ϕ inverts the sign of q and its absolute value. Figure 3.9 (c) shows Γ_R dependence of the conductance as a function of ϵ_R when λ and ϕ are 1 and 0, respectively. It found that $\Gamma_{L\ (R)}$ controls the width along $\epsilon_{L\ (R)}$ axis of the Fano's asymmetric parameter, namely, energy width of resonance. The strength of the direct transition between leads λ is important to describe Fano effect in DQD as discussed above. The line shapes along ϵ_R are considered here. However how to define the Fano's asymmetric parameter q should be considered because the system has two axes of the energy ϵ_R and ϵ_L.

3.8 Comparison between experiment and simulation

Let us compare our experimental data with those obtained using Eq. (3.18). Here, we note the following three points. (i) Although the energy levels in the QD, ϵ_R (ϵ_L), are determined mainly by V_R (V_L), they are slightly affected by V_L (V_R), (ii) because only a single level is assumed to exist in each QD, the formula can be applied only near the triple points, and (iii) the formula is valid only when the hopping matrix of the strongly coupled state (w) can be regarded as constant. We have 12 free parameters to simulate the experimental results: the gate-voltage-to-energy conversion rates (lever arms) α_L and α_R, the offsets of the gate voltage c_L and c_R, the energy bandwidths Γ_L and Γ_R, the coupling constant between the energy continuum and the discrete levels λ, and the phase ϕ, which is either 0 or π. We also take the amplitude of

the interference contribution G_0 and the background G_1. Regarding point (i) above, we include the cross-talk contribution of the gate voltage L (R) affecting the energy level of QDR (QDL), δ_L (δ_R). Finally, the conductance can be expressed as

$$G = G_0 \mathcal{T}_{LR}(\epsilon_L, \epsilon_R, \Gamma_L, \Gamma_R, \lambda, \phi) + G_1, \quad (3.63)$$

where

$$\epsilon_L = \alpha_L((V_L - c_L) + \delta_R(V_R - c_R)), \quad (3.64)$$
$$\epsilon_R = \alpha_R(\delta_L(V_L - c_L) + (V_R - c_R)). \quad (3.65)$$
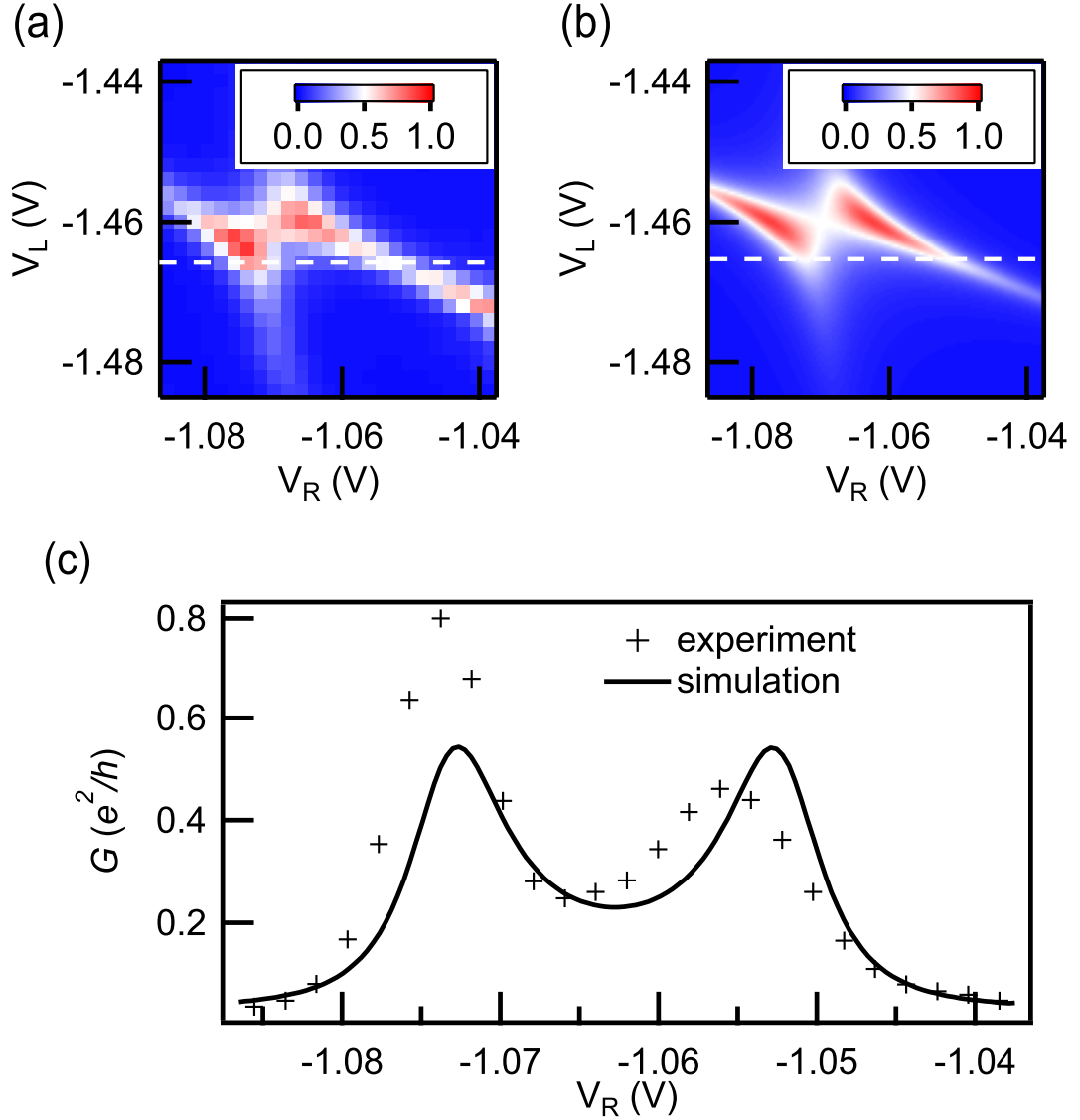
Figure 3.10: V_R and V_L dependence of the differential conductance at $V_C = -0.70$ V. (a) Experimental data. (b) Result of numerical simulation. (c) Line profiles at $V_L = -1.465$ V along white dashed lines in (a) and (b).

First, we show the result of the simulation for a region in a conventional DQD system by

setting $\lambda = 0$. The experimental data and simulated data obtained using least square fitting are plotted in Figs. 3.10 (a) and 3.10 (b), respectively. Figure 3.10 (c) shows the line profiles of Figs. 3.10 (a) and 3.10 (b) at $V_R = -1.465$ V. Anti-crossing line of charge transition lines and two triple points are reproduced.

(a)

(b)

(c)
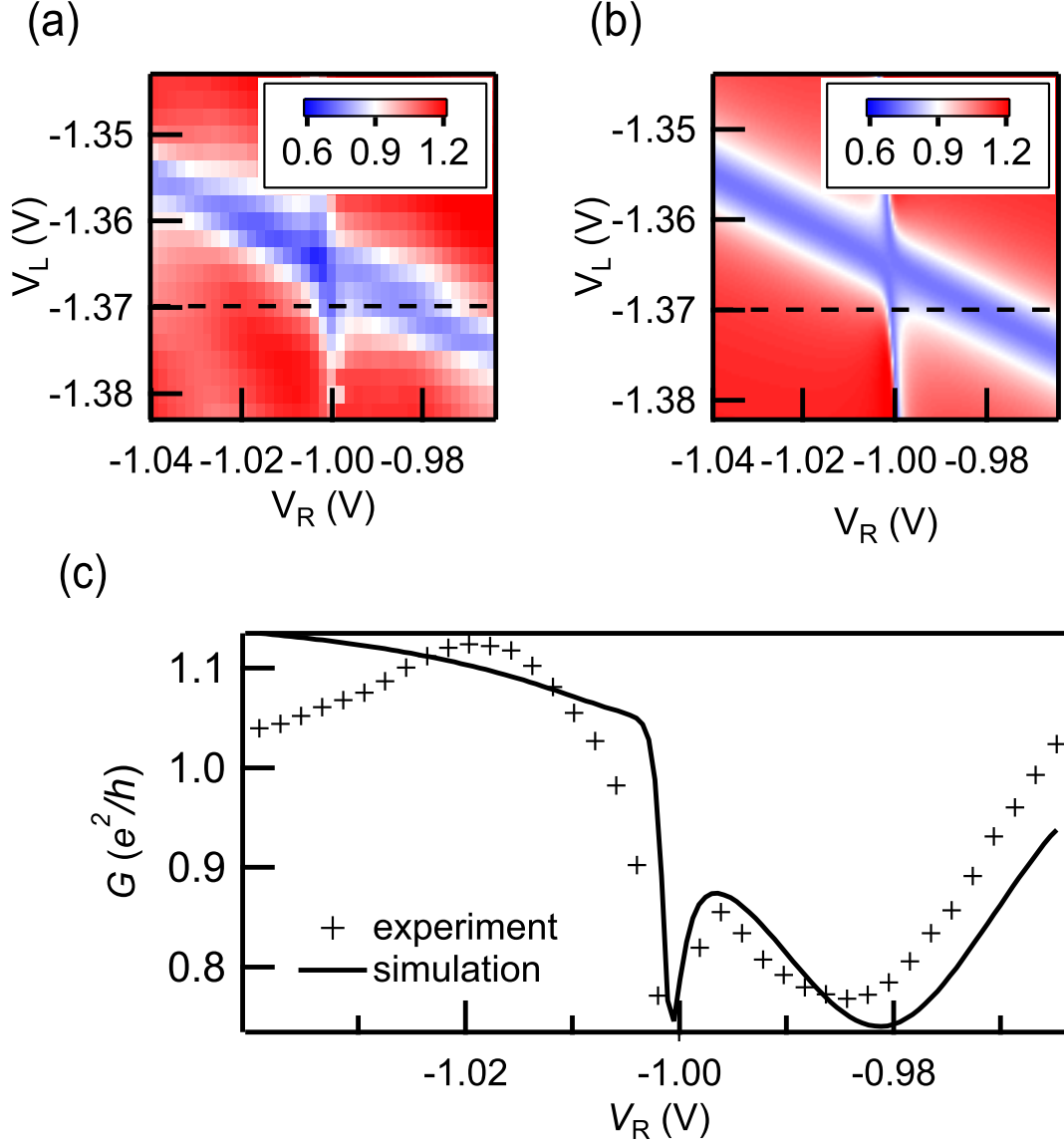
Figure 3.11: V_R and V_L dependence of the differential conductance at $V_C = -0.90$ V. (a) Experimental data. (b) Result of numerical simulation. λ value for this case is 0.71. (c) Line profiles at $V_L = -1.370$ V along black dashed lines in (a) and (b).

Next, we compare the numerical result with the experimental differential conductance shown in Fig. 3.11 (a), where the Fano effect is significant, namely, $\lambda \neq 0$. Figure 3.11 (b) shows the result of the model calculation with $\phi = \pi$, and Fig. 3.11 (c) plots the line profiles of Figs. 3.11 (a) and 3.11 (b) at $V_C = -0.90$ V and $V_L = -1.370$ V. As shown in the figures, the conductance dip caused by the Fano effect and anticrossing lines are nicely reproduced. Here, λ is set to be 0.71, being of the order of unity, which can be easily understood within our model. As we

discussed above, if λ is close to 0, the system behaves as a conventional DQD, while, for $\lambda \gg 1$, the conductance of background should be large. Peculiar Fano effect distinctly appears when λ is around 1. Thus, we successfully simulated the experimental data qualitatively using a simple model; both conventional DQD transport and Fano transport are explained within a simple theoretical framework.

We note, however, that the model does not perfectly reproduce the experimental result quantitatively, for several reasons. First, we assumed that the energy continuum that directly connects Leads L and R has a constant coupling w to the discrete levels in QDL and QDR. However, this is not necessarily the case, as we easily imagine that V_R and V_L modulate w. Second, the phase ϕ is not uniquely determined. Although we assumed $\phi = \pi$ in Figs. 3.11 (b) and 3.11 (c), a similar plot with different c_L and c_R is obtained when $\phi = 0$ is assumed. To determine the phase, we have to investigate the hopping integral between the QDs further. Finally, in the simulation, the Coulomb interaction is neglected. Experimentally, it was reported that it is surely relevant in the Fano transport regime in the side-coupled QD geometry [58]. In the present DQD geometry, the Coulomb repulsion may also affect the interference pattern.

3.9 Conclusion

To conclude, we considered the Fano effect in the DQD system and showed that a simple model reproduces the experimental observation qualitatively. The origin of the energy continuum that is necessary for this effect to occur is most probably the strongly coupled state between the two leads. Fano transport appears under a wide range of conditions even in the DQD geometry, which constitutes a clear example of the ubiquitous nature of this effect in mesoscopic transport. This work shows that the strongly coupled state emerges naturally and remains robust in the system, which might provide a clue for solving the long-standing phase measurement problem [37, 38, 39, 40, 41, 42, 43, 44, 55, 59, 62, 68, 69, 70, 71]. In addition, by further examining this effect, for example, by introducing a well-defined energy continuum [43, 44], it may become possible to directly measure the phase difference between the bonding and anti-bonding states in an artificial molecule system.

4 Charge sensing with RF SECD for current standard

In order to realize the current standard by using the single electron pumping in a quantum dot (QD), fast detection of the charge state is necessary. In this Chapter, the fast charge sensing using the reflection of the radio frequency (RF) from a single electron charge detector made of a quantum point contact (QPC) and a QD is demonstrated experimentally. Along with this direction, the error correction of the electron pump will be possible by feedback operation.

4.1 Introduction

As mention in Chapter 1, the present electric current standard is derived through Ohm's law by voltage standard and resistance standard even though Ampere is the fundamental unit of Système International d'unités (SI). The uncertainty of the present electric current standard is the order of sub-ppm (10^{-7})[15]. Definition of the current with pumping devices has a long history and various methods were developed [17, 73, 74]. Although measurement experts have been making a lot of efforts, the uncertainty of the current does not reach the level to revise the present electric current standard [19, 20]. The uncertainty of the current generated by single electron sources comes from operation errors of the single electron because the uncertainty of frequency provided in National Metrology Institute of Japan (NMIJ), National Institute of Advanced Industrial Science and Technology (AIST) reaches 10^{-12} [75].

In order to eliminate the errors of single electron pumping, error detection with a single electron charge detector (SECD) [76] whose resistance changes due to the presence of neighbor electrons is proposed and demonstrated in double quantum dot (DQD) [16, 77]. In this method, the single electron is manipulated from source to drain through the two QDs with its charge state detected by SECD. If the errors are detected, the correction signal is sent to maintain a constant current. Because the present detection time resolution is the order of ms, operation frequency must be lower than $1\,\mathrm{kHz}$. The current generated by $1\,\mathrm{kHz}$ is around $0.1\,\mathrm{fA}$, which is too small to be measured precisely. The detection time resolution is limited by the measurement speed of the SECD. The speed-up of measurement improves the detection time resolution and enables to operate pumping devices with higher frequency. Actually, it is demonstrated with resonant circuit [78]. It is called RF SECD measured by radio frequency (RF) of $1.7\,\mathrm{GHz}$. Combination of the error detection with RF SECD and the error correction would enable electron pumping with high frequency. Our works described in this Chapter was performed towards the realization of these methods.

Here, the mechanism of single electron charge detection by QPC is introduced. Figure 4.1 (a) is a schematic of the SECD to detect that the number of electrons in the QD is changed by V_p. In our case, the SECD consists of the QPC by using negative gate voltage V_QPC, but the QPC can be replaced by another QD whose sensitivity is better than that of the QPC [79]. Because the SECD is capacitively coupled to the QD, the conductance of the SECD, in this case, the
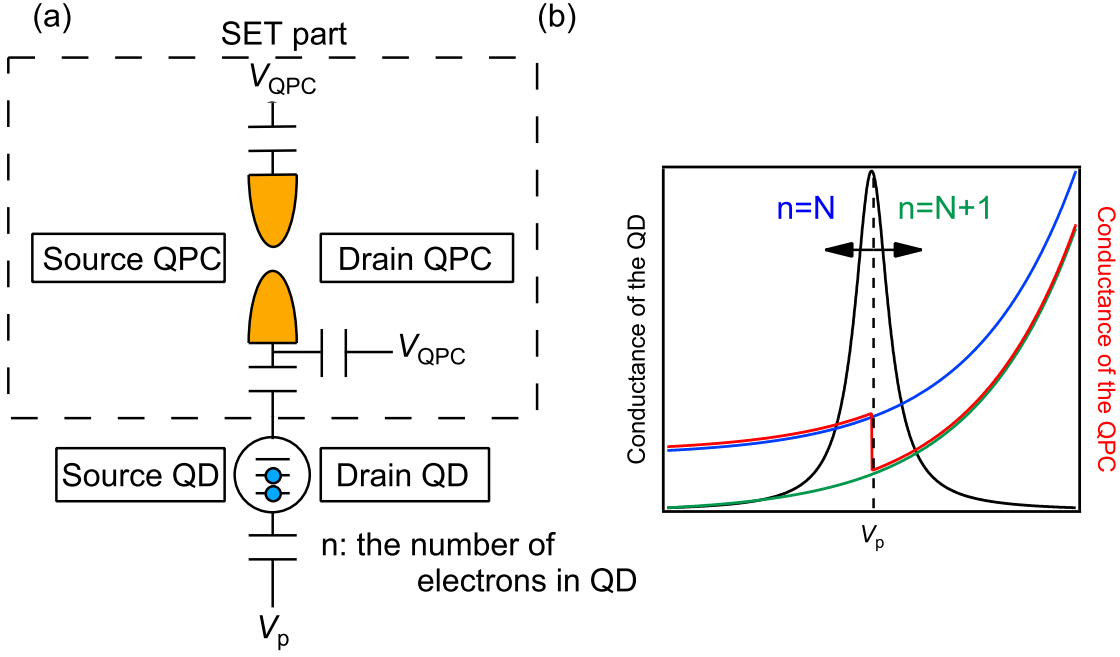
Figure 4.1: (a) Schematics of SECD. The SECD consisting of a QPC is capacitively coupled to the QD. The number of electron in the QD is manipulated by V_p. The QPC can be changed with a QD, which yields a larger signal when the number of the QD changes. (b) A diagram of the conductance of the QD and QPC (SECD). The black line represents V_p dependence of the QD's conductance. The conductance of the QPC is shown by red line. Blue and green lines express V_p dependence of the QPC when the number of electrons in the QD are N and $N+1$, respectively.

QPC depends on the number of electrons in the QD and V_p. Figure 4.1 (b) is a schematic of the conductance of the QD and QPC as a function of V_p. Around the Coulomb peak shown by a black curve, the number of electrons in QD changes. The red curve schematically shows the image of the QPC's conductance as function of V_p, which has a step. This step is a signal of detection that the number of electrons in the QD changes. The blue and green curves are a diagram of the QPC's conductance as a function of V_p if the number of electron n is fixed at N and $N+1$, respectively. Because the potential formed by electrons in the QD affects the QPC, decreasing of the number of electrons in the QD raises the conductance of the QPC (see the green line and blue line in Fig. 4.1 (b)). In reality, the step of the conductance of V_p around the Coulomb peak is observed as shown in the red line since the number of electron in the QD changes around the Coulomb peak [69]. This measurement technique is the way to confirm the number of electrons in a QD because there is no conductance when the QD has a few electrons.

Simple wiring is not suitable for fast detection of the signal from SECD. Because the resistance of SECD R and the capacitance of the 1 m coaxial line C are around $10\,\mathrm{k\Omega}$ and $100\,\mathrm{pF}$, respectively. Its low-cut frequency f_C of the measurement line is around $200\,\mathrm{kHz}$. Therefore the maximum time resolution of charge detection with SECD is $5\,\mu\mathrm{s}$ even if RF is applied on the SECD. It is not suitable for the current standard. In order to solve this problem, RF SECD is considered [78]. The RF SECD consists of the SECD's resistance and tank circuit. Thanks to the tank circuit, the signal of RF reaches measuring instruments without filtering. In Ref. [78], the number change of electrons in the QD made of a metallic island is detected by the change

of the reflection signal's intensity. It is possible to detect the change of the resistance with this
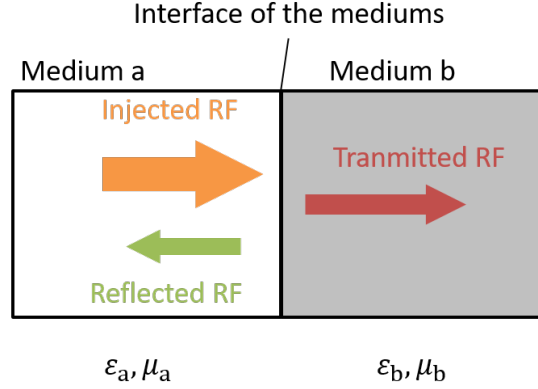
Figure 4.2: A diagram that RF enters from the medium a into the medium b. The RF is reflected at the interface of a and b. The electricity and permeability of medium x (= a, b) are noted ε_x and μ_x.

technique.

The RF, however, has a technical difficulty on impedance mismatching. Figure 4.2 expresses that RF enters from medium a into medium b. The electricity and permeability of medium x are noted ε_x and μ_x. The wave impedance Z_x is defined as

$$Z_x = \sqrt{\frac{\mu_x}{\varepsilon_x}}. \tag{4.1}$$

Z_x is the ratio of the electric field and magnetic field in the medium x (= a, b). If the impedance of a is different from that of b, the injected RF is reflected due to the continuity of the electric field, magnetic field and their derivative, which is called impedance mismatching. In an electric circuit, similar impedance is defined. In the electric circuit, the impedance Z is defined by inductance per unit length L and capacitance per unit length C when there is no energy loss.

$$Z = \sqrt{\frac{L}{C}}. \tag{4.2}$$

Of course, RF propagating electric circuit is reflected when the impedance changes at the interface.

If there is an impedance mismatching at RF SECD, the reflection signal decreases. The impedance mismatching is solved by tuning inductance and capacitance of the circuit. The problem on impedance matching for RF SECD is that the sample exists in the dilution refrigerator. The method to tune the impedance by using a variable capacitance diode is demonstrated [80]. Variable capacitance diode is controlled by the applied voltage which modulates the length of the depletion area of the varactor diode. In this experiment, this technique is used to increase the intensity of the RF signal. Figure 4.4 shows our experiment to tune the impedance of the tank circuit. Figure 4.4 (a) is a circuit diagram to match the impedance by using the variable capacitor. The variable capacitors (V_{cs} and V_{cm}) are controlled by an applied voltage in order to tune the impedance of the tank circuit Eq. (4.2). Figures 4.4 (b) and (c) is the intensity of RF reflection as a function of frequency when the HEMT (ATF-35143, Broadcom Ltd.) is insulating. As shown in Fig. 4.4 (b) and (c), the dip of the RF reflection

as a function of frequency has an optimal voltage applied on V_{cs} and V_{cm}, respectively. The sensitivity of RF SECD is good when the intensity of the dip is large. It is found that variable capacitors raise the intensity of RF reflection from SECD. Variable capacitors, however, do not have a perfect reproducibility from measurement to measurement.
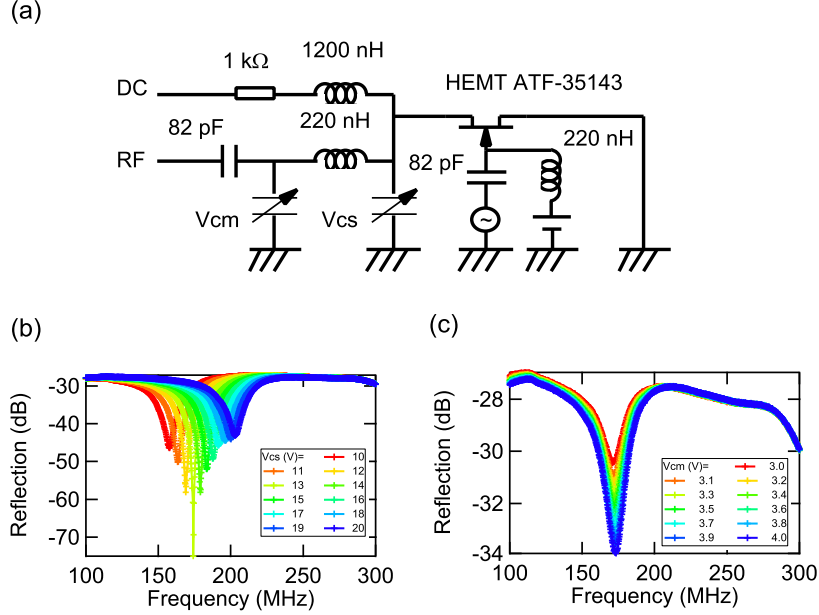
Figure 4.3: (a) A circuit to test impedance matching with variable capacitors controlled by the applied voltage. (b, c) The intensity of reflection signal as a function of frequency when the HEMT is insulating. The color differences correspond to that of applied on each variable capacitor (b) The impedance of the circuit is tuned by V_{cs}. (c) The impedance of the circuit is tuned by V_{cm}.
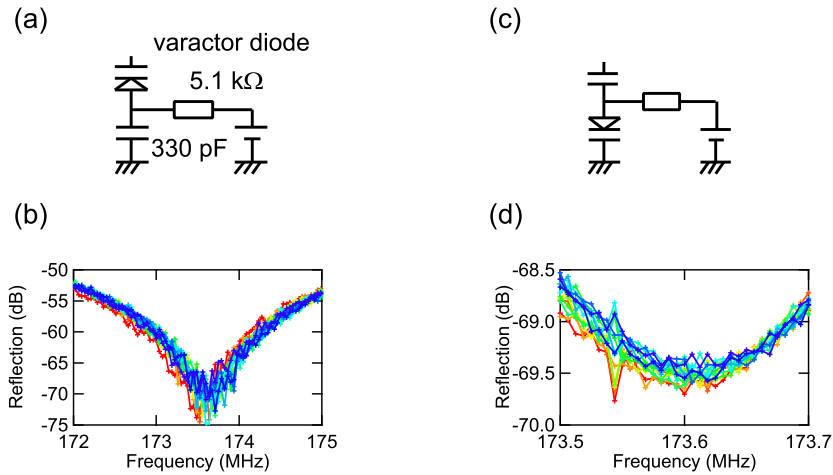
Figure 4.4: The stability of the tank circuit with two variable capacitors. (b) and (d) show frequency dependence of the RF reflection's intensity when the electric circuit of variable capacitor are (a) and (c), respectively.

We confirm the stability of the tank circuit with the same setup to Fig. 4.4. (a) and (c) in Fig. 4.4 show the electric circuit of variable capacitor. The difference between (a) and (c) is the position of the varactor diode (MA46H204-1056, MACOM Technology Solutions Holdings, Inc.). (b) and (d) in Fig. 4.4 show the intensity of the RF reflection as a function of frequency measured every an hour for 13 hours. In case of Fig. 4.4 (a), the intensity of reflection changes by 10 dB. On the other hand, in case of Fig. 4.4 (b), the intensity of reflection changes by 0.5 dB. It is found that the position exchange of the varactor diode improves the stability of the tank circuit. In RF SECD measurement, the circuit diagram of the variable capacitor is Fig. 4.4 (b).

4.2 Sample and sample holder

Figure 4.5 shows our sample which is the same with what we observed the Fano effect described in the previous Chapter. Please note that notations of the gate electrodes and source drain are changed from those of the previous Chapter for the sake of explanation. The notation of each gate electrode and applied voltage on it are Bx (x: number) and V_{Bx}, respectively.
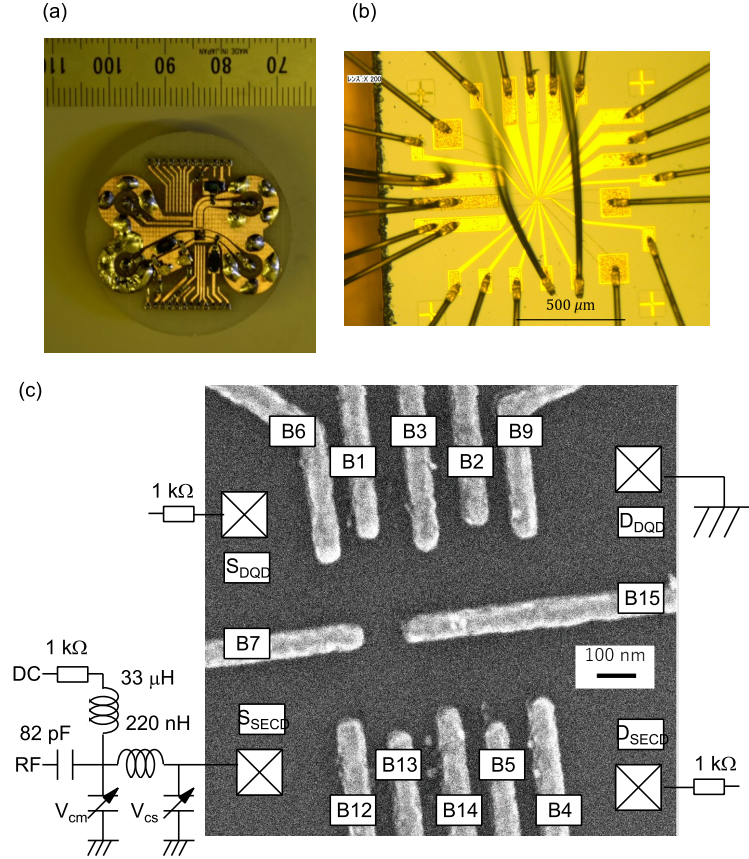
Figure 4.5: (a) A photo of our sample holder which contains the tank circuit for RF measurement and bias tees. (b) An optical microscope image of our sample. (c) A scanning electron microscope (SEM) image of our device with schematic circuits.

As explained in the previous Chapter, the sample is fabricated from a GaAs/AlGaAs two dimensional electron gas (2DEG) system by standard electron beam lithography, deposition

of metallic gate electrodes, and wet etching. The 2DEG is formed at a depth of 70 nm from the surface. The mobility and the electron density of this wafer at 77 K are $2.54 \times 10^5 \, \mathrm{cm^2/Vs}$ and $2.63 \times 10^{11} \, \mathrm{cm^{-2}}$. Several low-pass filters are inserted into the DC lines to avoid electric noise, both in the mixing chamber and at room temperature. The gates B7 and B15 divide the 2DEG into top and bottom electrically. Top five gates (B6, B1, B3, B2 and B9) above the gates B7 and B15 form DQD to transfer electrons one by one. The plunger gates (B1 and B2) of the DQD formed on the top side is connected to the RF lines (RF3 and RF4) in order to transfer a single electron from source to drain. Low-pass filters (VLFX-80, Mini-Circuit, inc.) are inserted into these RF lines (RF3 and RF4) at the mixing chamber to prevent capacitive coupling with the RF line connected to the SECD (RF5). However, these RF lines are not connected with RF generators in this work. On the other hand, the five gates (B12, B13, B14, B5, and B4) form SECD made of a QD and a QPC to sense the charging state of the top DQD. For the RF measurement, a tank circuit is connected with the source of the SECD. A geometrical asymmetry of the gates B7 and B15 differentiates the coupling between SECD and the left QD, and between SECD and the right QD. Otherwise, it is impossible to detect in which QD its charging state is changed.

The distance between the gate electrodes is important to fabricate quantum dot. Figure 4.6 shows the gate voltage dependence of the conductance between RF5 to GND at 8 mK.
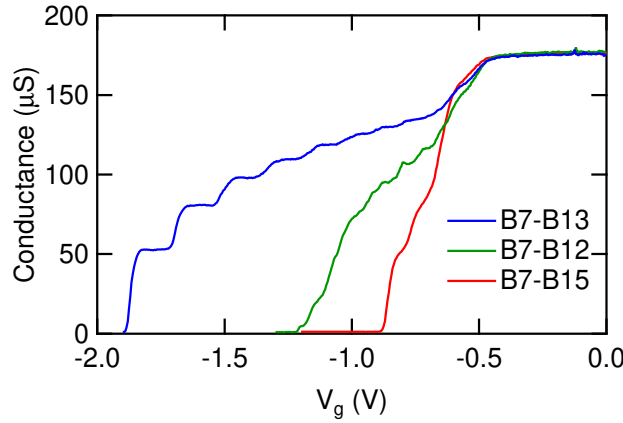
Figure 4.6: The conductance between S_{SECD} to GND as a function of the gate voltage at 8 mK. (red curve) The gate voltage is applied on the gates B7 and B15. (green curve) The gate voltage is applied on the gates B7 and B12. (blue curve) The gate voltage is applied on the gates B7 and B15.

Figure 4.6 shows the gate voltage dependence of the conductance through QPC formed by well separated gate electrodes B7 and B15. It is found that 2DEG under the gate electrodes B7 and B15 is killed around -0.4 V, and top 2DEG and bottom 2DEG are completely separated at -0.9 V. The gate voltage to completely deplete 2DEG under the gate electrodes is almost the same among different gate electrodes but pinch off voltage is different from the gates to gates due to the distance between the gate electrodes, which means B3 and B15 have high adjustability of the QPC conductance. The adjustability of a QPC conductance is important to form a QD since the QD requires sensitive gate modulation. However, too separated gate electrodes cannot pinch 2DEG off.

In the following, I will show the results of single quantum dot, double quantum dot, detection of charging state with SECD, and detection of charging state with RF SECD step by step.

4.3 Single quantum dot

I show the transport of the top left QD formed by B7, B15, B6, B1, and B3. In this Chapter, B7 and B15 are fixed at $-0.9\,\mathrm{V}$ in order to kill the transmission between the top 2DEG and the bottom 2DEG. In order to find a good parameter of the gate voltages, side gates of QD, in this case, gates B3 and B6, the conductance between S_{DQD} and GND was measured with fixing the plunger gate B1 $=-0.5\,\mathrm{V}$. The gate voltage of the plunger gate is decided to kill the 2DEG below the gate electrode. Figure 4.7 (a) is an intensity plot of the conductance as functions of the side gates B3 and B6 with fixing the plunger gate B1 at $-0.5\,\mathrm{V}$. The color of intensity plot corresponds to the conductance between S_{DQD} and GND G_{DQD}. The blue regions indicate insulating regime and the red regions indicate conductive regime. The medium conductance regions are shown as white. As strong negative voltages are applied on the gates B3 and B6, the conductance enters the insulating region, which is shown as blue in the intensity plot. White stripes appear between red regions and blue regions. Black lines are guidelines where the gate voltage condition of the dot-lead coupling is symmetric. The three graphs in Fig. 4.7 (b) show the plunger gate voltage dependence of the conductance at each point on the intensity plot. The color of each point corresponds to that of the curve of each graph. As explained in the previous Chapter, continuous transition from conventional QD into Kondo region and Fano region is observed. Especially, the observation of the Kondo effect proves that our QD is not far from symmetric dot-lead coupling regime.
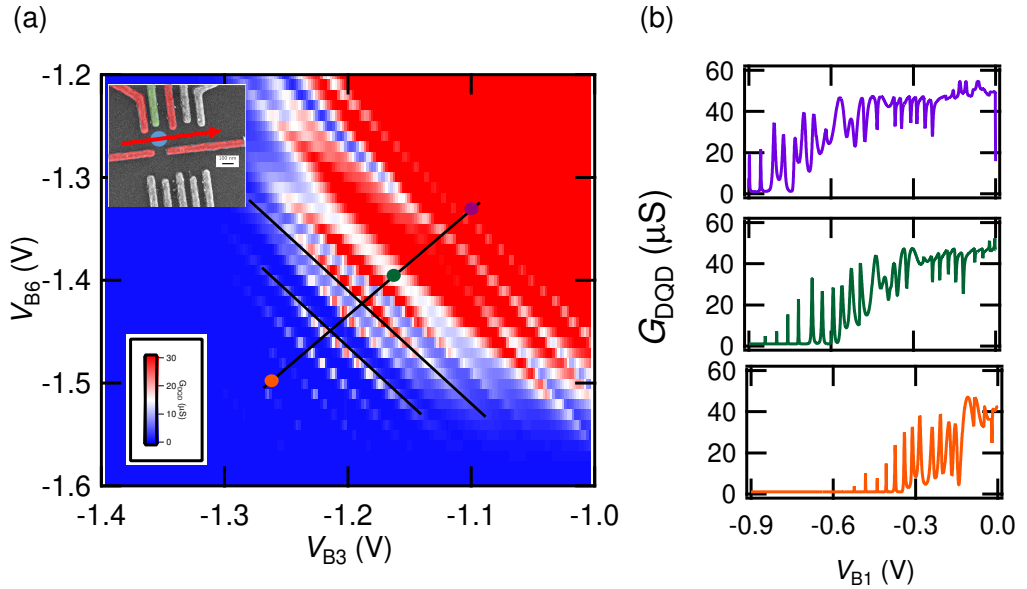
Figure 4.7: Intensity plot of G_{DQD} the conductance between S_{DQD} and GND as functions of B3 and B6 (a) and plunger gate voltage dependence of QD at each point (b). The color of the points in the (a) corresponds to that of the curves in (b).

4.4 Double quantum dot (DQD)

Next, we measured DQD. The guideline for reaching the DQD region is almost the same as in the case of a single DQ. Intensity plot of the conductance as functions of the voltages

applied on the side gates (B9 and B6) was obtained with the voltage applied on inner gates (B1, B3, and B2) fixed. Figure 4.8 shows the resulting intensity plots of the conductance as functions of B9 and B6 when the gate voltages applied on inner gates, $V_{B1} = -0.5\,\text{V}$ and $V_{B2} = -0.25\,\text{V}$. These intensity plots are obtained at four different B3 conditions, namely, $V_{B3} = -0.80\,\text{V}, -0.90\,\text{V}, -1.0\,\text{V}, -0.95\,\text{V}$.
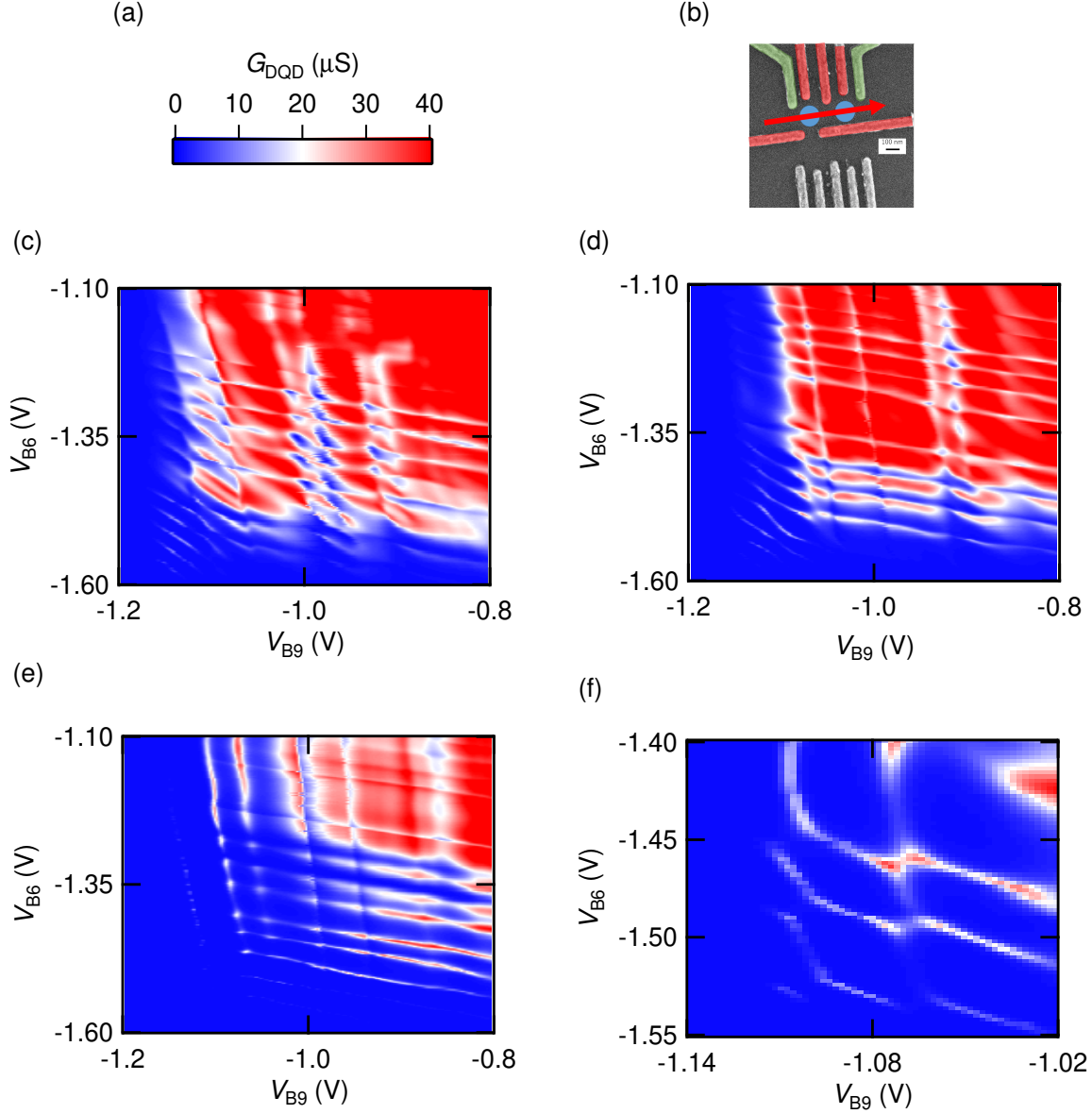
Figure 4.8: The intensity plots of the conductance as functions of B6 and B9 at four different B3 conditions. (a) Color scale of the conductance as functions of V_{B9} and V_{B6} shown in (c) to (f). (b) SEM image of the sample indicates B9 and B6 in green areas. (c) $V_{B3} = -0.80\,\text{V}$. (d) $V_{B3} = -0.90\,\text{V}$. (e) $V_{B3} = -1.00\,\text{V}$. (f) $V_{B3} = -0.95\,\text{V}$.

The regime to be measured is similar to that of a single QD case. It was found that B3 $= -0.95\,\text{V}$ is good because clear behavior that is expected for DQD is observed. Since B9 and B6 control not only discrete levels but also dot-lead coupling, they should be fixed at certain

value. Figure 4.9 is intensity plot of the conductance as functions of the plunger gates (B1 and B2) at $V_{B6} = -1.4400\,\text{V}$, $V_{B3} = -0.95\,\text{V}$, and $V_{B2} = -1.05256\,\text{V}$.
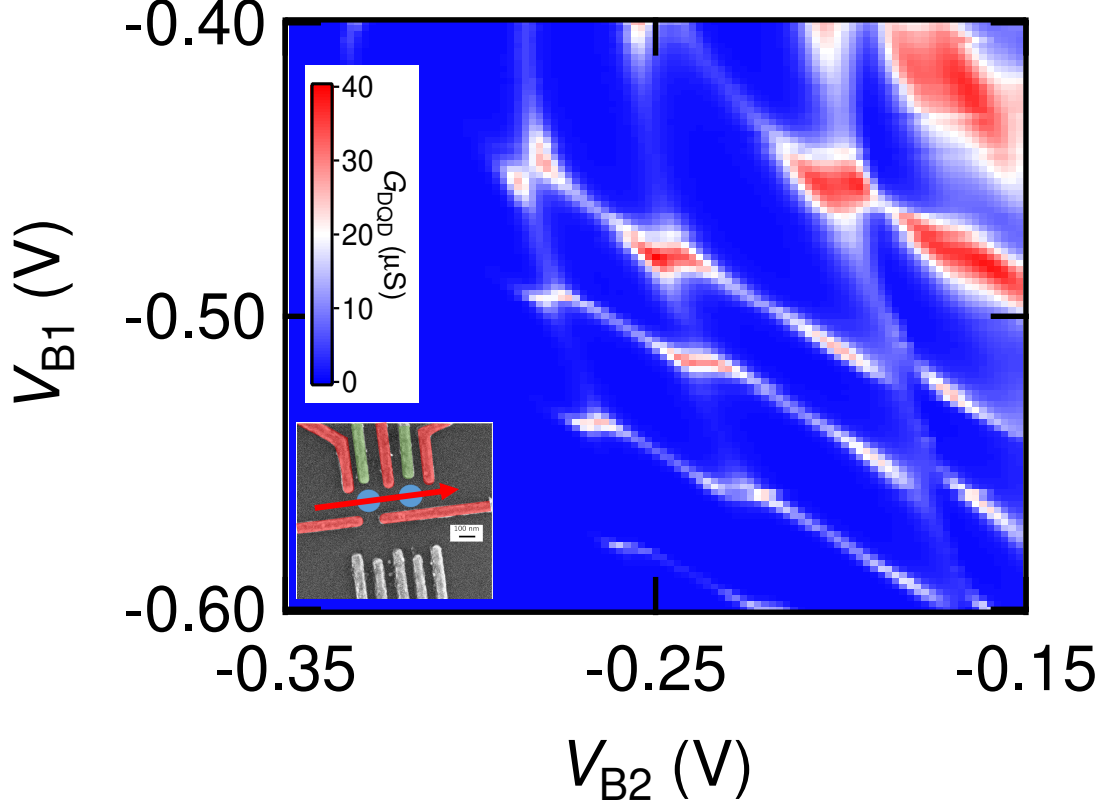
Figure 4.9: The charge stability diagram of top DQD at $V_{B7} = V_{B15} = -0.90\,\text{V}$, $V_{B6} = -1.4400\,\text{V}$, $V_{B3} = -0.95\,\text{V}$, $V_{B9} = -1.05256\,\text{V}$ and the others $= 0\,\text{V}$.

We obtained the intensity plot of the conductance of a conventional DQD called "charge stability diagram", which has Coulomb blockade regions, charge transition lines, and triple points. Figure 4.10 shows how to understand the charge stability diagram. In each panel, the left side expresses the situation when the charge stability diagram shown in the right side is obtained.

The conduction electrons can propagate DQD when its energy is equal to discrete levels which have finite energy width. In case that each gate electrode controls each discrete level, and there is no Coulomb interaction between the QDs, the charge stability diagram is shown in Fig. 4.10 (a) which is an orthogonal lattice pattern. The numbers (charging state) shows the numbers of electrons that left QD and right QD have.
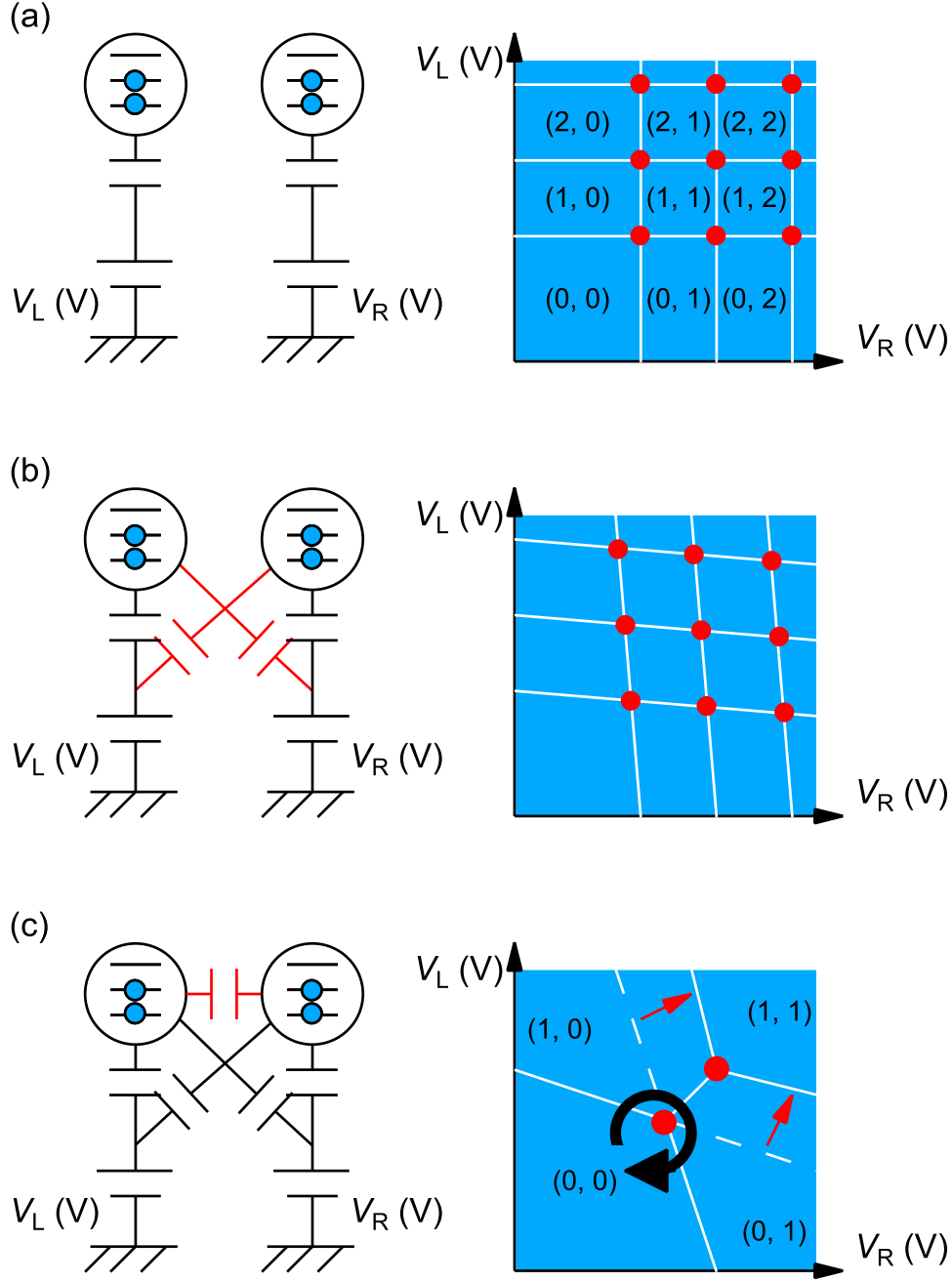
Figure 4.10: Schematics to understand charge stability diagrams. (a) In case that each gate voltage controls each discrete level only. (b) In case that the one gate electrode affects the discrete levels in the other QD. (c) In case that there is Coulomb interaction between The QDs. This corresponds to a realistic situation. The method to generate current with DQD by the gate control is shown by the black line.

In reality, the one plunger gate for a QD affects the other discrete level in the other QD, and therefore charge transition lines should be tilted (Fig. 4.10 (b)). More realistically, the existence of electrons in one QD gives Coulomb potential. The crossing points turns into the triple points (Fig. 4.10 (c)). The distance between split two triple points depends on the coupling between the QDs. This triple point is important because it enables us to generate precise current by

appropriate gate operation. The black line in Fig. 4.10 (c) shows how to transfer a single electron from the left lead to the left QD, the right QD, and the right lead. If this gate operation is done by frequency f, the current of ef is generated.We note that the above discussion is based on the classical picture and the coherent couplings between the discrete levels in the QDs are ignored.

4.5 Charge sensing detected by the conductance of the QPC

When the gate operation to generate the current is performed, it is impossible to measure the conductance to know the charging state of the DQD. A technique to measure the charging state without measuring the conductance of the DQD is charge sensing with SECD. The SECD consists of a QPC and QD. They are sensitive to the electrostatic potential coming from the existence of electron in the more neighbor QD. Because the number of electrons in QD is discrete, the conductance of SECD jumps when the number of electrons in QD changes. Figure 4.11 (a) shows the conductance of the DQD (red curve, left axis) and the conductance of the SECD made of QPC formed at B14 (blue curve, right axis) as a function of V_{B1}.
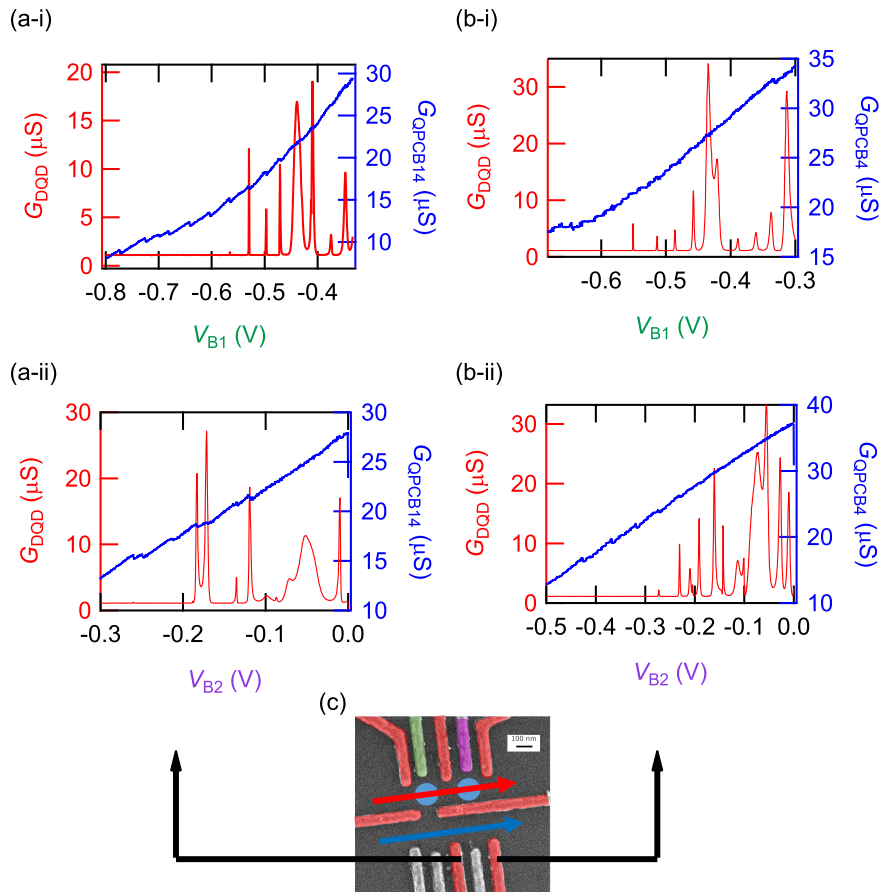
Figure 4.11: (a) and (b) The gate voltage dependence of the conductance of the DQD (red curve, left axis) and the SECD (blue curve, right axis) measured by the QPC formed by B14 and B4, respectively. (i) and (ii) are V_{B1} shown in the green area in (c) and V_{B2} indicated in the purple area in (c) dependence of them. (c) SEM image of the sample to show the geometry.

At each Coulomb peaks in the red curve, the blue curve shows a stepwise behavior. Remarkably, even when there is no detectable conductance of DQD for $V_{B1} < -0.6\,\text{V}$, the blue curve shows the stepwise behaviors. This indicates that SECD enables to detect sensitively changing the number of electron in DQD one by one. Figure 4.11 (b) is obtained by the same measurement of Fig. 4.11 (a) with SECD of QPC formed by B4. Figure 4.11 (c), (d) show V_{B2} dependence of the conductance of DQD and SECD formed by B14 and B4, respectively. In all the graphs in Fig. 4.11, the jumps of the conductance of the SECD are observed at the same gate voltage of Coulomb peaks. These jumps are observed clearly when there is no conductance in the DQD. As can be seen, charge detection with SECD is more sensitive than direct transport measurement. V_{B1} dependence of charge sensing with B4's QPC shows no jump because B4 is too far from left QD of the DQD to sense changing of Coulomb potential. It should be noted that the working position of SECD should be adjusted little by little during charge detection because the gate operation of the DQD affects SECD.

Figure 4.12 shows the intensity plot of the charge stability diagram measured by direct transport (a) and SECD (b). Because the charge transition is detected by jump of SECD's the conductance, the derivative of the SECD's conductance is plotted to enhance clarity.
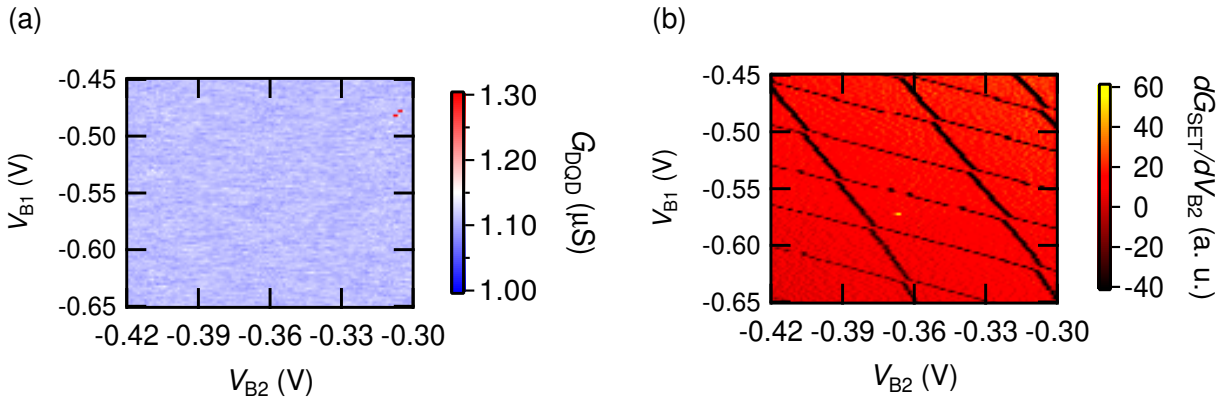
Figure 4.12: The charge stability diagram of the top DQD (a) Measured by direct transport. (b) Measured by the SECD of QPC formed by B14.

As one can see, direct transport of the DQD gives no information but charge stability diagram measured by SECD gives clear transition lines. This regime is adequate for current generation by gate operation because only a small leak current is expected through the DQD but charge detection is still possible by SECD.

Figure 4.13 proves how convenient the SECD is. B3 which controls the coupling between QDs dependence of the charge stability diagram measured by direct transport and SECD. As explained in Fig. 4.10, the distance between neighbor triple points depends on the coupling between QDs. The stronger negative voltage is applied on B3, the shorter the distance between neighbor triple points is. The advantage of SECD lies in that biasing on SECD gives little effect on DQD. So the signal-to-noise (S/N) ratio can be improved by applying higher voltage on SECD.
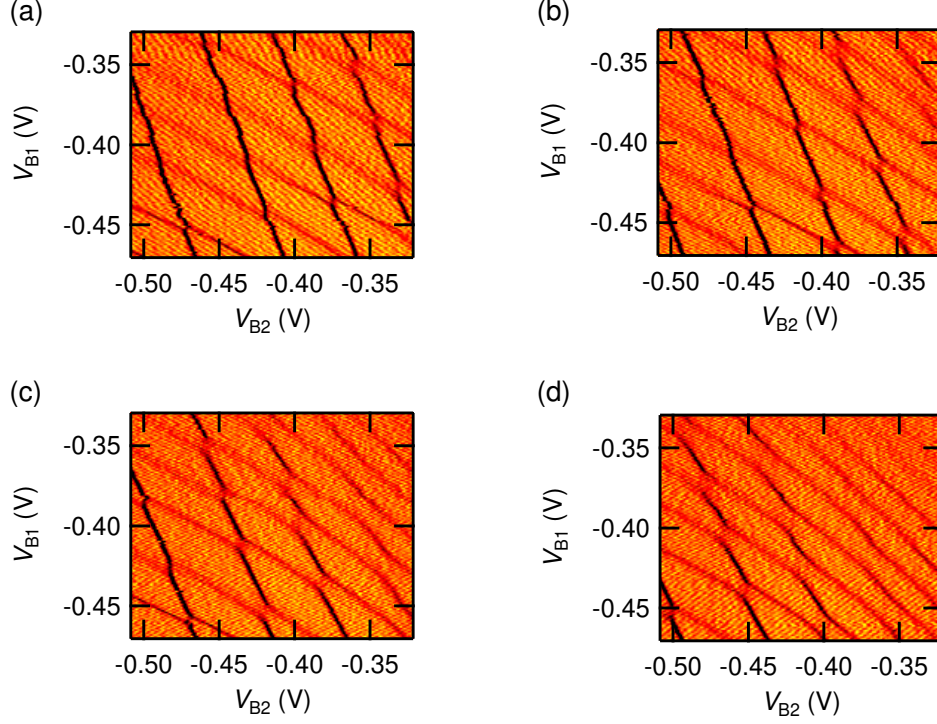
Figure 4.13: V_{B3} dependences of the charge stability diagram of the DQD. (a) $V_{B3} = -0.83\,\text{V}$. (b) $V_{B3} = -0.80\,\text{V}$. (c) $V_{B3} = -0.77\,\text{V}$. (d) $V_{B3} = -0.74\,\text{V}$.

4.6 Single electron transistor detected by the radio frequency reflection

As above discussed, we proved that the transition of the single electron in DQD can be detected by the SECD. However, in order to realize a realistic precise current generation, we have to improve the measurement speed. In this subsection, the RF detection and the corresponding experimental setup are described.

The conductance measurement by lock-in technique requires integration time around 300 ms, which is too slow to correct gate operation. Therefore charging state is measured by radio frequency. Figure 4.14 shows the setup to detect the charging state by using RF reflection. Except for the sample in the mixing chamber of the dilution fridge, the setup is the same to that of AM radio. The setup is explained below. The propagation wave of RF is injected into RF splitter. One output is connected to the coaxial line connected to the device under test (DUT), the other one is connected to LO port of RF mixer (ZFM-3-S+, Mini-Cicuits, Inc.) through the delay lines to tune the electric wavelength. Figure 4.14 shows the measurement setup to measure the radio frequency reflected at the SECD.The coaxial lines between RF input and the DUT have several RF components, attenuates, directional coupler, and DC cut. The attenuators (XMA Corp.) have great two roles. First, the attenuators cool down the measurement line because it connects the outer metal of the coaxial line and inner conductor through the resistance.
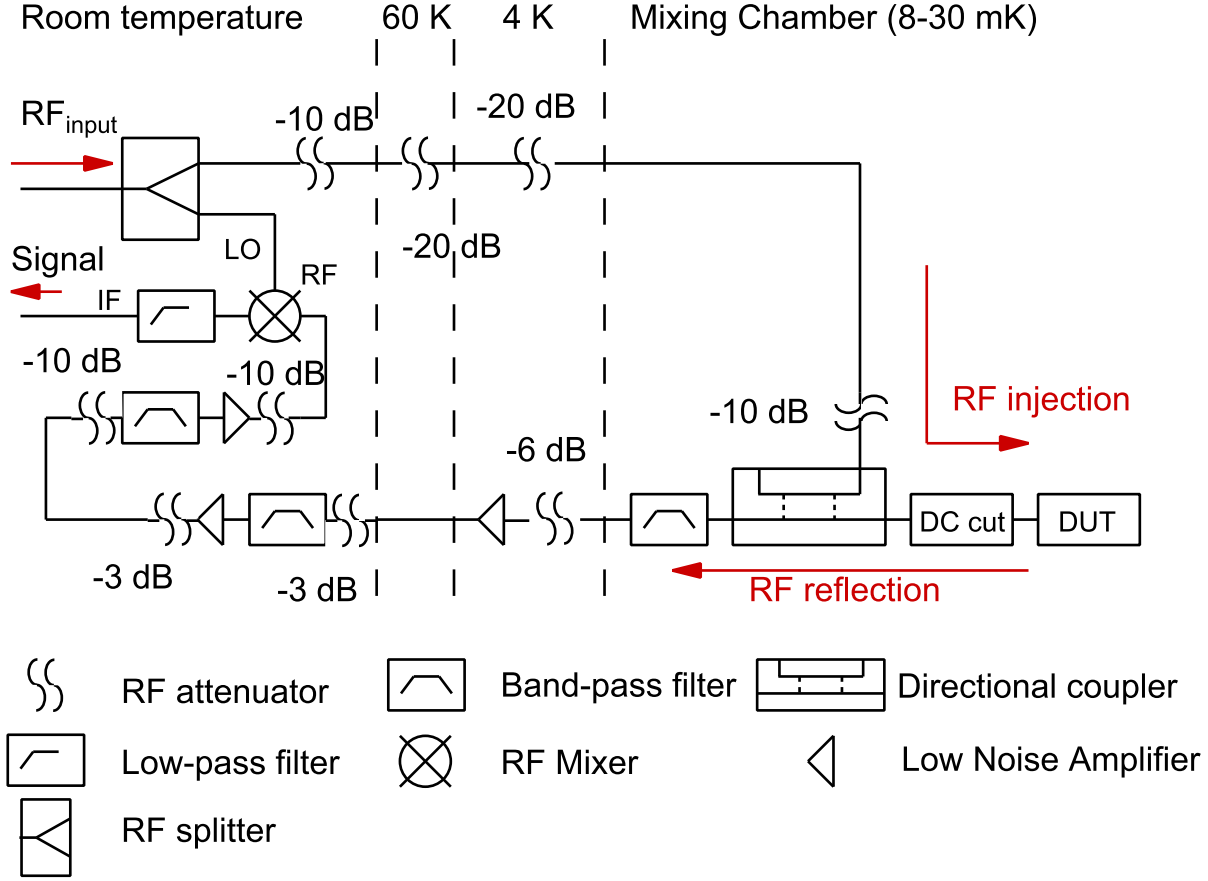
Figure 4.14: The wiring for RF detection.

Second, the attenuators decrease noise signal caused by thermal fluctuation. Therefore attenuators should be inserted in the measurement line at each stage of the dilution fridge. The directional coupler (ZEDC-15-2B, Mini-Circuits Inc.) is important to measure the reflection signal from the device selectively. The DC cut (BLK-18-S+, Mini-Circuit, Inc.) is installed because the quality of measurement was improved in the preliminary experiment. The reflected signal which contains the information of the SECD reaches the RF port of the RF mixer for homodyne conversion through the low noise amplifiers (LNA), band-pass filters and attenuators. S/N ratio depends on the first amplifier since successive amplifiers also amplify the signal including noise generated by the previous amplifier. In order to improve measurement quality, the LNA CITLF2, SiGe HBT fabricated in California Technology University which generates ultra low noise is used at 4 K stage. The latter LNAs at room temperature are PE15A1012, Pasternack Enterprises, Inc. Attenuators are inserted into input and output of each amplifier to protect against being broken by a pulse generated by electrostatics and the reflection from the successive amplifiers. The bandpass filters 50-250 MHz which consists of a low-pass filter SLP-250+ and high-pass filter SHP-50+ (Mini-Circuits, Inc.) are important to cut undesired noise which affects the homodyne signal. The homodyne signal is measured by a digital multimeter (DMM) through the low-pass filter SLP-1.9+, Mini-Circuits Inc.

It is important to check if each component works or not. After this work, it was found that DC cut (BLK-18-S+) was strong attenuator at low temperature. In this experiment, a phase shifter and coaxial cables are used for homodyne conversion to change the path length, but the phase shift by coaxial cables takes a long time to adjust the phase of RF and harmful for the

LNAs. IQ measurement and the phase measurement is better because they require no phase adjustment of RF [81, 82].

The intensity of reflection signal from the tank circuit's reflection signal depends on the chip inductor, chip capacitors, and resistance of SECD. The values of discrete parts (inductor and capacitors) is fixed, and so the intensity of reflection signal depends only on the resistance of SECD. Figure 4.15 shows V_{B14} dependence of QPC's conductance and reflection signal measured simultaneously. The resonant frequency is around $140\,\mathrm{MHz}$ when V_{cm} and V_{cm} are fixed at $12\,\mathrm{V}$ and $0\,\mathrm{V}$, respectively.
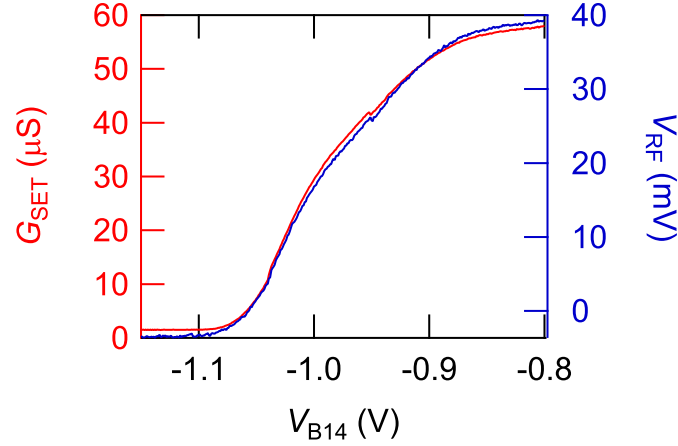
Figure 4.15: The conductance and reflection signal of QPC formed by B14 as a function of V_{B14}.

The left graph in Fig. 4.15 shows the conductance of the QPC formed by B14 (red curve, left axis) G_{SECD} and the homodyned signal of radio frequency at $140426800\,\mathrm{Hz}$ reflected by the tank circuit including the resistance of the QPC (blue curve, right axis) V_{RF} as a function of V_{B14}. Obviously the intensity of the reflection signal depends on the conductance of the QPC. This result indicates that the charging state of the top DQD can be detected by RF. When $\left|\frac{dG_{\mathrm{SECD}}}{dV_{B14}}\right|$ is the largest, the QPC has the highest sensitivity as a charge sensor. Figure 4.16 shows V_{B2} dependence of the conductance of SECD and the intensity of the reflection signal.
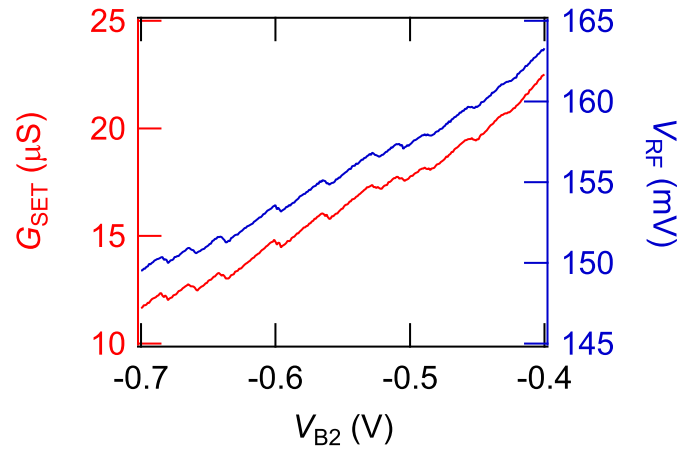
Figure 4.16: V_{B2} dependence of SECD's the conductance and the intensity of the RF reflection.

The line shapes of the conductance and the intensity of the reflection signal is almost the same, which clearly indicates that RF SECD works and is available to detect the charging state of DQD. Figure 4.17 is the intensity plot of the DQD's charge stability digram measured by conductance of the SECD and reflection signal.
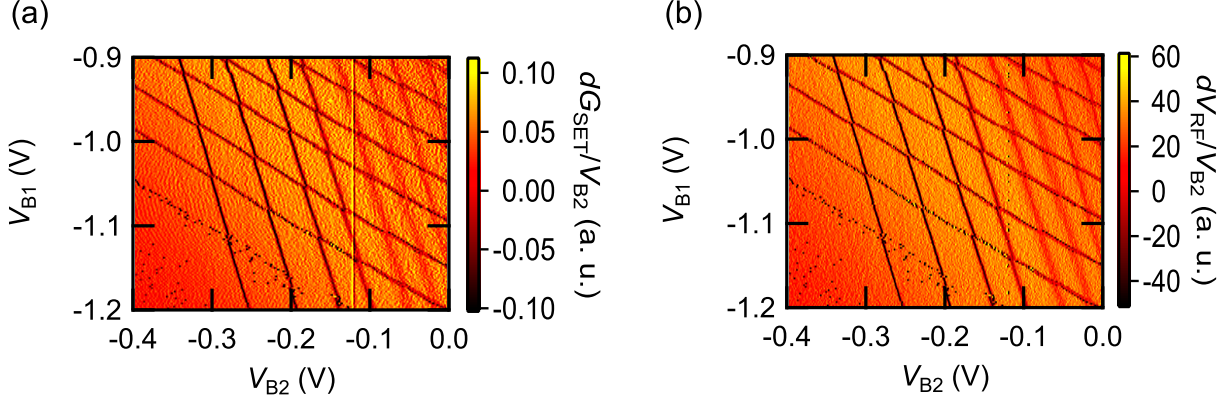

Figure 4.17: The DQD's charge stability diagram (a) measured by the conductance measurement (b) measured by the intensity of reflection signal.

Since the change of charging state is observed as a jump, their derivatives are plotted. It is found that the charge detection with RF is successful. There is a small difference between these two. As a technical comment, there is a yellow line at $V_{B2} = -0.12\,\mathrm{V}$ in the left graph. This value corresponds to range change of the voltage supplier (GS200, Yokogawa Test & Measurement, Corp.). The charge detection by RF SECD is so fast that the yellow line is less obvious in the right.

4.7 Conclusion and perspective

We have developed RF measurement setup and succeeded in the measurement of charge stability diagram of DQD with RF SECD. Since RF reflection was measured by DMM whose integration time is $10\,\mathrm{PLC}=1/6\,\mathrm{s}$, it is required to measure the reflection signal in a short time. If the operation frequency is $10\,\mathrm{MHz}$ which can generate the current of around $1.6\,\mathrm{pA}$, measurement time must be shorter than $100\,\mathrm{ns}$. Therefore the realization of current standard with single electron operation requires improvement of S/N ratio in order to complete measurement of the charging state in a short time. Changing the frequency band is a good solution because the bandwidth is wider at higher frequencies, and black body radiation is absent at low temperature. In this sense, techniques of circuit quantum electrodynamics are suitable because stray inductance and capacitance dominate the resonant circuit at higher frequency bands [81, 82].

New current standard based single electron operation which is exactly relevant to new definition of current has the potential to establish new measurement techniques. The new techniques may improve the precision of measurement and will serve to find new phenomena [83].

4.8 Appendix

4.8.1 RF SECD of a QD

As mention before, a QD can be an SECD, which has better sensitivity than that of a QPC. Figure 4.18 (c) is a SEM image to show the SECD to measure Fig. 4.18 (a) and (b). Figure 4.18 (a) and (b) are the raw data to take the charge stability diagram measured by the left bottom QD (the orange area in Fig. 4.18 (c)) and QPC B14 (the purple area in Fig. 4.18 (c)), respectively. A coulomb peak with steps are observed in V_{B2} dependence of the RF reflection measured by the SECD of the QD (Fig. 4.18 (a)). These jumps are of the order of mV. On the other hand, a slope with steps are observed in V_{B2} dependence of the RF reflection measured by the SECD of the QPC (Fig. 4.18 (b)). These jumps are less than $1\,\mathrm{mV}$. SECD of a QD has not only high sensitivity but also a short range which the SECD can work. It is better to tune the working position of SECD by modulation of the plunger gate of the QD.
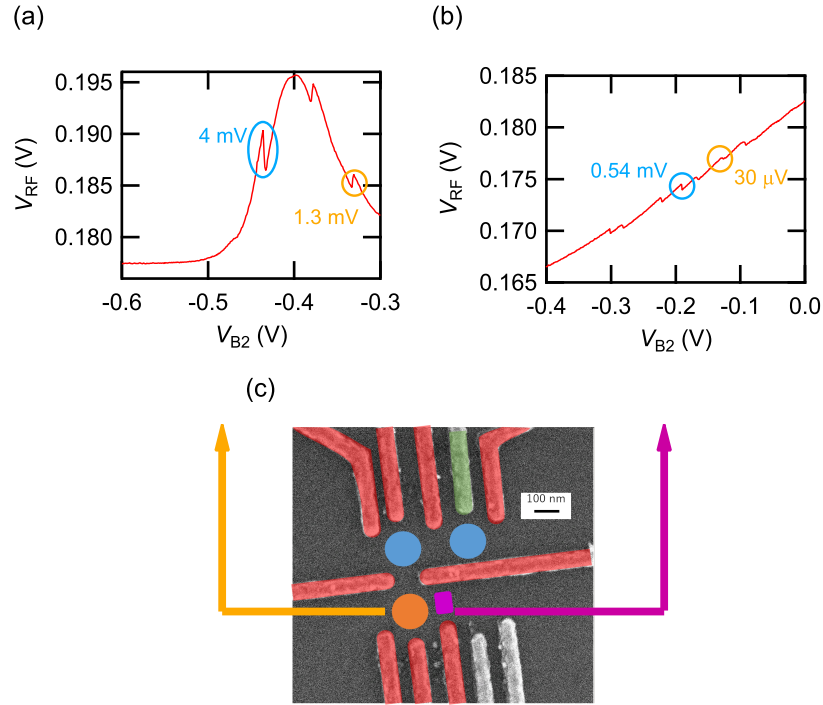
Figure 4.18: Raw data to take the charge stability diagram. (a) Measured by the left bottom QD. (b) Measured by the QPC B4. (c) The SEM image of the sample to show the SECD. The red areas indicate used gate electrodes. The green electrode indicates B2 which controls the number of electron in the top DQD. The orange circle indicates the bottom left QD used to measure (a). The purple area is the QPC formed by B4 which is used to yield (b).

5 Single electron pumping

To generate current by using clock controlled single electron sources is a key technology to investigate dynamics in a quantum system and to realize the electric current standard. A tunable barrier tunneling device is a promising single-electron pump. In this Chapter, the Experiment to operate tunable barrier tunneling device is described.

5.1 Introduction

Single electron sources are studied for a long time to establish an electric current standard [73][84][85]. In addition, recently, single electron sources get attention as coherent electron sources "flying quantum bits" which transfer quantum information owing to the extensibility of the devices [86, 87, 88, 89, 90]. Single electron pumping devices for quantum optics are fabricated on GaAs/AlGaAs 2DEG[21, 90]. There are several methods to realize single electron pumping, and each single electron sources has its own advantage and disadvantages[86, 87, 88, 90]. As a typical example of such a device, tunable barrier tunneling device excites hot electrons with exciting electrons inside a QD around hundred meV above Fermi surface[25, 86]. Because the transmission channel is completely pinched off, no leakage current is expected, which is a big advantage for the realization of the current standard. The disadvantage is that the sample is heated up by high power operation radio frequency. As a second example, the mesoscopic capacitor is a successful pumping device which enables to observe two-particle interference[21, 87]. It excites single electrons from QD around tens μeV above Fermi surface, which is good to study quantum phenomenon whose energy scale is very low compared to the Fermi energy. The disadvantage is that it excites single electrons and single holes due to the loading electron into QD. Because of this, the mesoscopic capacitor is not suitable as the current standard. Thirdly surface acoustic wave which generates propagating potential barrier can transfer a single electron in a QD into the other QD[89]. The result is read out with a single electron transistor (SET) as shown in the previous chapter. It preserves with spin operation in QD because surface acoustic wave transfers only a single electron. The disadvantage is that high engineering RF techniques are required. Finally, Leviton excitation is a successful pumping device in quantum optics[90]. Levitons are excited by applying Lorentzian shape RF pulse on Ohmic contacts, which generates minimal excitation of the electron. The disadvantage is that the non-Lorentzian shape of RF pulse generates not only electrons but also holes. Although all pumps have advantage and disadvantage, they require both nano-fabrication techniques and RF measurement technique to drive the pumping devices.

As mention in the Chapter 1, real-time measurement with pump-probe technique is possible with the single electron sources. However, electron dynamics in the mesoscopic conductor is unexplored field. Our final target is the real-time measurement of the evolution of Kondo cloud. We, however, had no knowledge of measurement with RF and single electron sources. Therefore we decided to establish the techniques of single electron sources. We chose tunable barrier tunneling device as a single electron source because

- I had measured it in Dr. Masaya Kataoka group in National Physical Laboratory, England (strongest reason).
- It requires common techniques to fabricate single electron sources such as fine structure etching and to measure as small current as several to several hundred pA.
- It requires simple setup, function generator, current measurement system, and ^{4}He dipping station, all of which are available in my group in Osaka University.

Compared with tunable barrier tunneling device, mesoscopic capacitor and Leviton excitation requires expensive measurement system. Because mesoscopic capacitor always emits the same number of holes after emission of electrons, accumulation card to measure the real-time response is required. On the other hand, Leviton excitation requires arbitrary wave generator to emit Lorentzian pulse, otherwise additional electrons and holes are excited.

In this Chapter, I show how tunable barrier tunneling device works and how to find working conditions. The detail of the fabrication process of the devices is described in Chapter 2.

5.2 Measurement setup

Measurements were done with ^{4}He dipping station at 4.2 K. Detail of the dipping station, for example, line filtering, homemade current-voltage converter etc., are explained in Appendix of this Chapter. The setup of the current pumping is shown in Fig. 5.1.
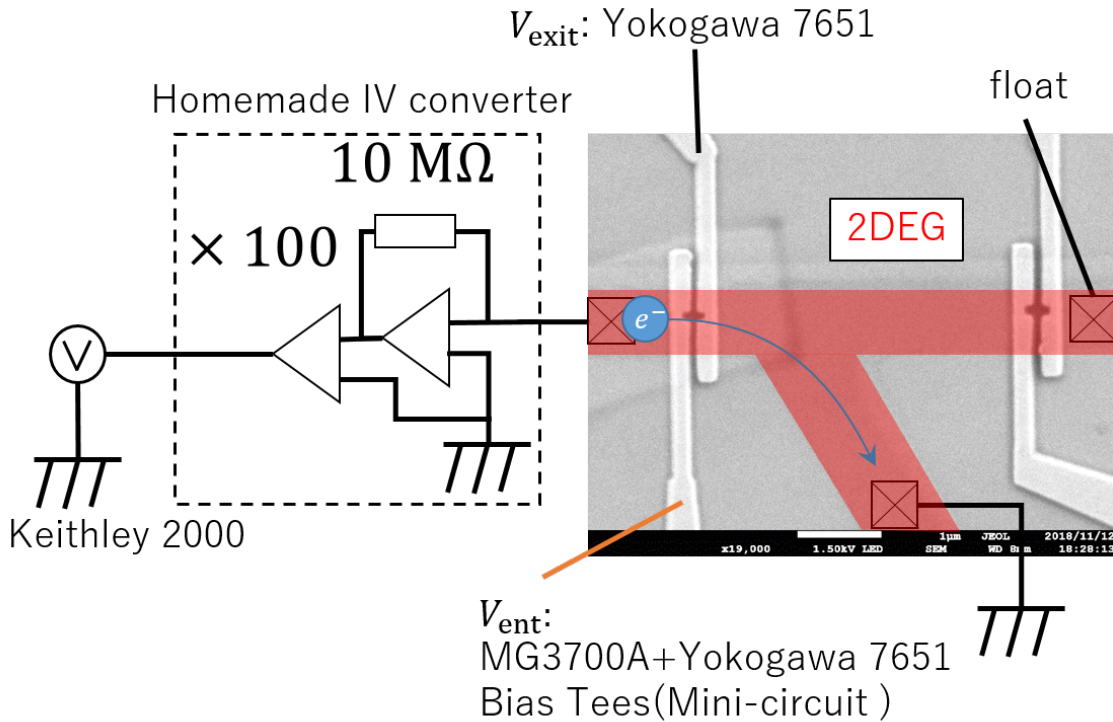
Figure 5.1: Measurement setup for the pumping device. A scanning electron microscope (SEM) image of a typical device is also shown in the right. The area of 2DEG is shown in red. White regions show gate electrodes made of Ti and Au. The device with a wider slit between the entrance gate and exit gate is used in the experiment described here. Measurement line is grounded at room temperature.
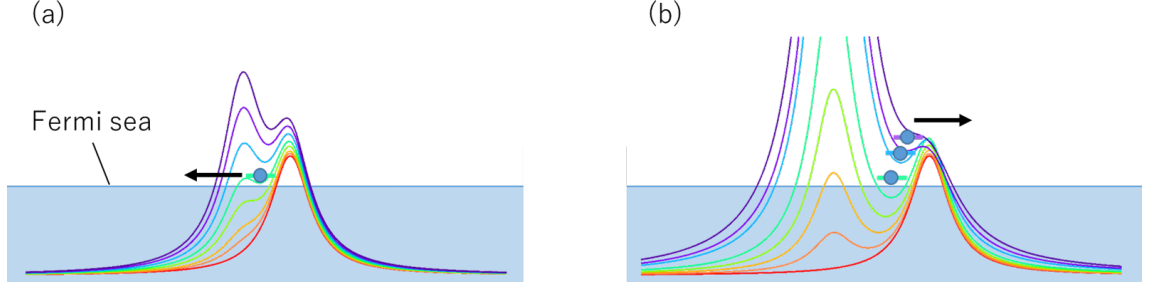
Figure 5.2: Schematic image of working tunable barrier tunneling device. Left potential peak and right potential peak are generated by V_{ent} and V_{exit}, respectively. (a) The potential development as time in case of distance between the entrance gate and the exit gate is too short for proper pumping operation. (b) The potential development as time in case of distance between the entrance gate and the exit gate is well designed.

The device is fabricated by using lithography techniques shown in Chapter 2. The key elements of tunable barrier tunneling device are narrow 2DEG wire which prevents an existence of unintentional QD, exit gate electrode applied V_{exit} which stops electron and squeezing entrance gate electrode applied V_{ent} with radio frequency (Fig. 5.1). The right electrodes are also pumping device, which has a wider slit than the left one. This sample was fabricated to check the good distance between V_{ent} and V_{exit}.

Figure 5.2 shows a schematic image of the pumping device [86, 91]. In this figure, color difference expresses time development in $\pi/2$ cycle of radio frequency. The Left potential peak and right potential peak stem from V_{ent} and V_{exit}, respectively. The distance between the entrance gate and exit gate is an important parameter for good pumping devices. If these electrodes are too close, the captured electron goes back to the original place before squeezing out for the right side (Fig. 5.2 (a)). To make matters worse, the potential barrier generated by V_{exit} might be opened by V_{ent}. When the distance between two gate electrodes is appropriate, a single electron is pumped across the potential coming from V_{exit} (Fig. 5.2 (b)).

5.3 Results

As a feature of tunable barrier tunneling device, it works when V_{ent} and V_{exit} are high enough to kill the conductance without radio frequency. Figure 5.3 shows the gate voltage dependences of the two terminal conductance with $100\,\mu\mathrm{V}$ excitation.

The conductance measurement has been done with homemade IV converter and lock-in amplifier (SR830, Stanford Research Systems). Since DC lines contain low pass filter made of one $1\,\mathrm{k\Omega}$ and two $1\,\mathrm{nF}$ at the sample holder, the two terminal resistance of $1\,\mu\mathrm{m}$ width and $20\,\mu\mathrm{m}$ length 2DEG including Ohmic contacts and the measurement line is around $5\,\mathrm{k\Omega}$. The gate electrodes consisting of the pumping device pinch the 2DEG off at $-0.45\,\mathrm{V}$. Gate electrodes QDc, QDl, QDr, and QDp define a QPC and QD, and the pinch-off gate voltage is lower than one of the pumping electrodes. It is found that the distance of gate electrode QDc and QDp is suitable to form QD because they have high controllability on the transport.
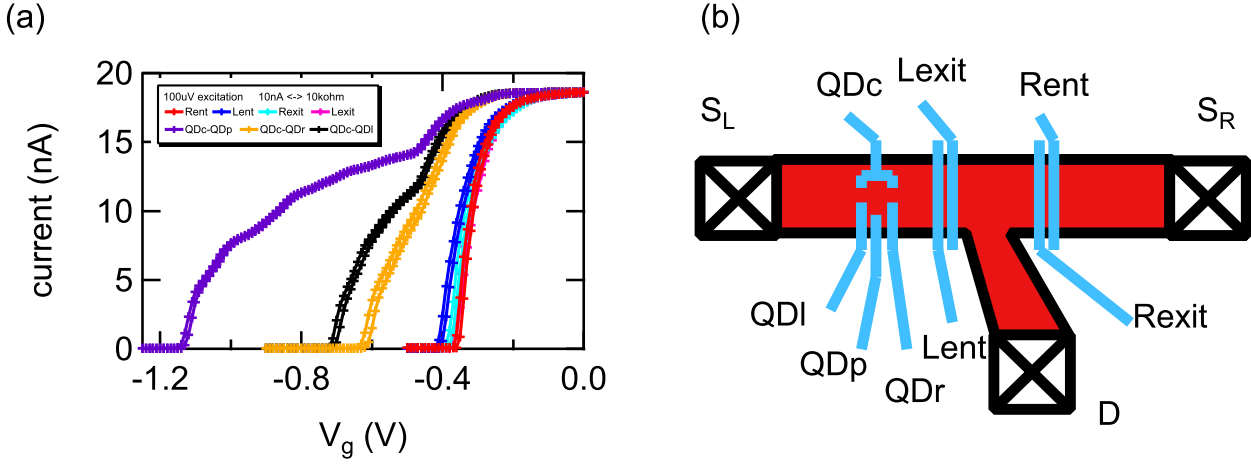
(a)

(b)

Figure 5.3: (a) Gate voltage dependence of the two terminal conductance between S_L and S_R with $100\,\mu$V excitation. (b) Schematic of the sample geometry.

Let us move on electron pumping. The measurement setup is shown in Fig. 5.1 but the actual geometry of gate electrodes is different. The data I show here is taken by QD whose size is
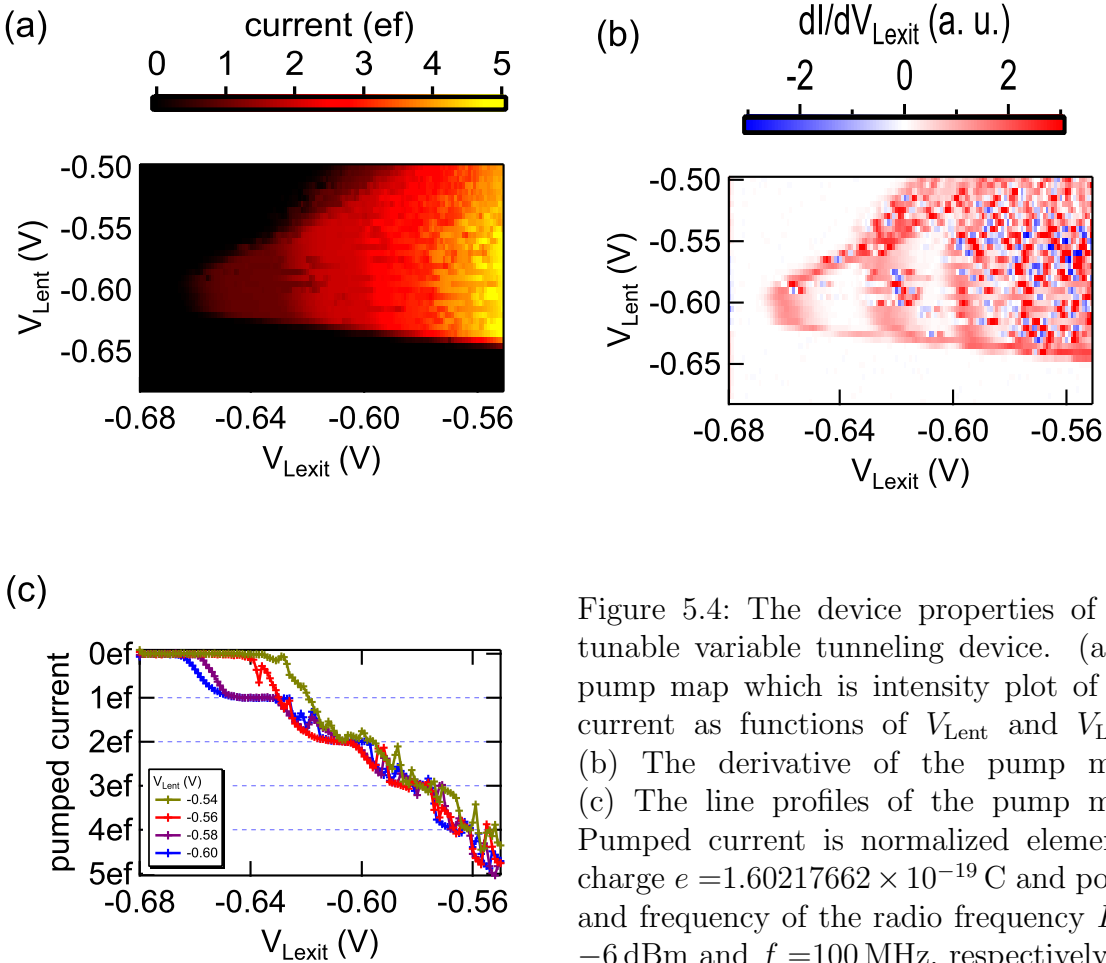

(a)

(b)

(c)

Figure 5.4: The device properties of the tunable variable tunneling device. (a) A pump map which is intensity plot of the current as functions of V_{Lent} and V_{Lexit}. (b) The derivative of the pump map. (c) The line profiles of the pump map. Pumped current is normalized elemental charge $e = 1.60217662 \times 10^{-19}$ C and power and frequency of the radio frequency $P = -6\,$dBm and $f = 100\,$MHz, respectively.

designed to be 140 nm × 140 nm. An actual step to check the device is at first fixing V_{ent} at a certain voltage lower than the pinch-off voltage, in this case, -0.45 V, then sweeping V_{exit} in the range that 2DEG is pinched off with applying 100 MHz radio frequency to V_{ent}. Repeating sweeping at different V_{ent} yields the pumped current as functions of V_{ent} and V_{exit}, so-called "pump map".

Figure 5.4 shows the current as functions of V_{Lent} and V_{Lexit} "pump map" (a), the derivative of pump map dI/dV_{Lexit} (b), and line profiles of the pump map (c) pumped by 100 MHz sine wave whose power is -6 dBm . The Pump map contains all information on the behavior of the pumping device, but the line profiles and the derivative of pump map are more convenient. In order to evaluate pumped current, line profile is suitable. On the other hand, the differential pump map is convenient to check where the plateau is. Schematic figure of an ideal differential pump map is shown in Fig. 5.5. Before forming QD, several electrons go back to the original Fermi sea (Fig. 5.2). The stronger V_{Lexit} is, the less QD have electrons. The vertical lines show the maximum number of electrons that QD can contain. On the other hand, the stronger V_{Lent} is, the more electrons are transferred across the potential barrier. The horizontal lines show the number of electrons left in QD. Strong V_{Lent} gives not only larger pumping current but also no current due to the failure of electron loading. Since V_{Lent} controls the center position of potential barrier which oscillates with frequency f, too large V_{Lent} prevents the potential barrier reaches down to the chemical potential of leads. Therefore no electrons can be loaded into QD.

While the experimentally obtained pump map can be basically understood as explained above, the experimental data shown in Fig. 5.6 show two differences from the expectation in Fig. 5.5. First, there are no plateaus with leaving some electrons in QD at -6, -5 and -4 dBm. It is expected that plateaus with leaving some electrons in QD in the region higher than $V_{ent} = -0.5$ V. However, it is impossible because the 2DEG channel opens when the potential formed by V_{exit} decreases. Some noise is observed in the weak gate voltage region of V_{Lent} and V_{Lexit}, which might be caused by impurity levels. The impurity levels trap and release electrons, which
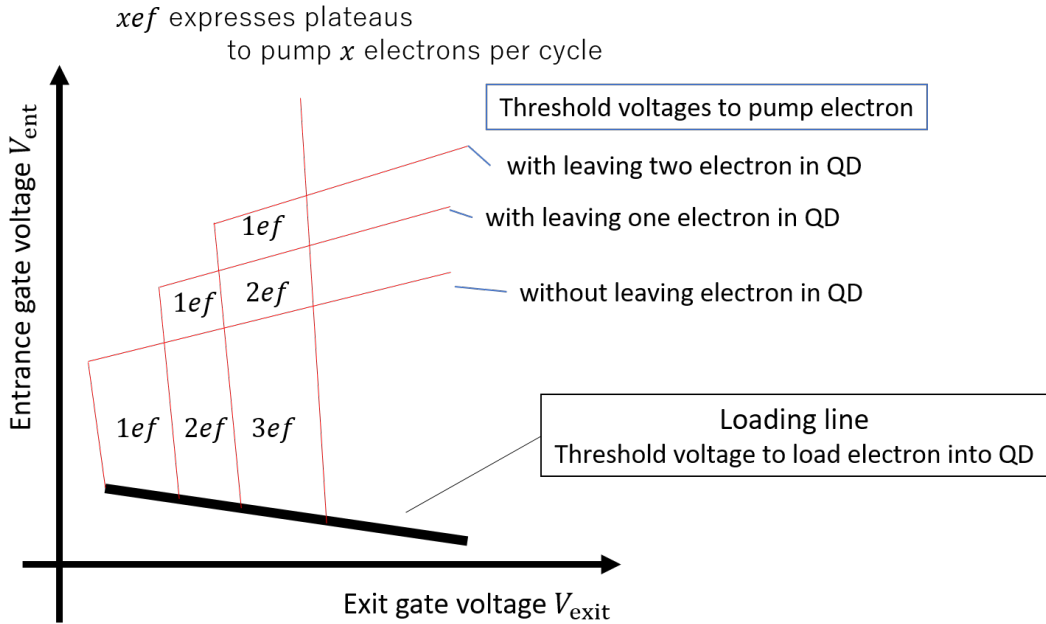

Figure 5.5: Schematic of ideal differential pump map.

generates random telegraph noise. The problem can be improved by expansion of the size of the QD. The farther the distance between the entrance gate and the exit gate is, the stronger the gate voltages of the proper working region are. The device properties might be improved by such optimization.
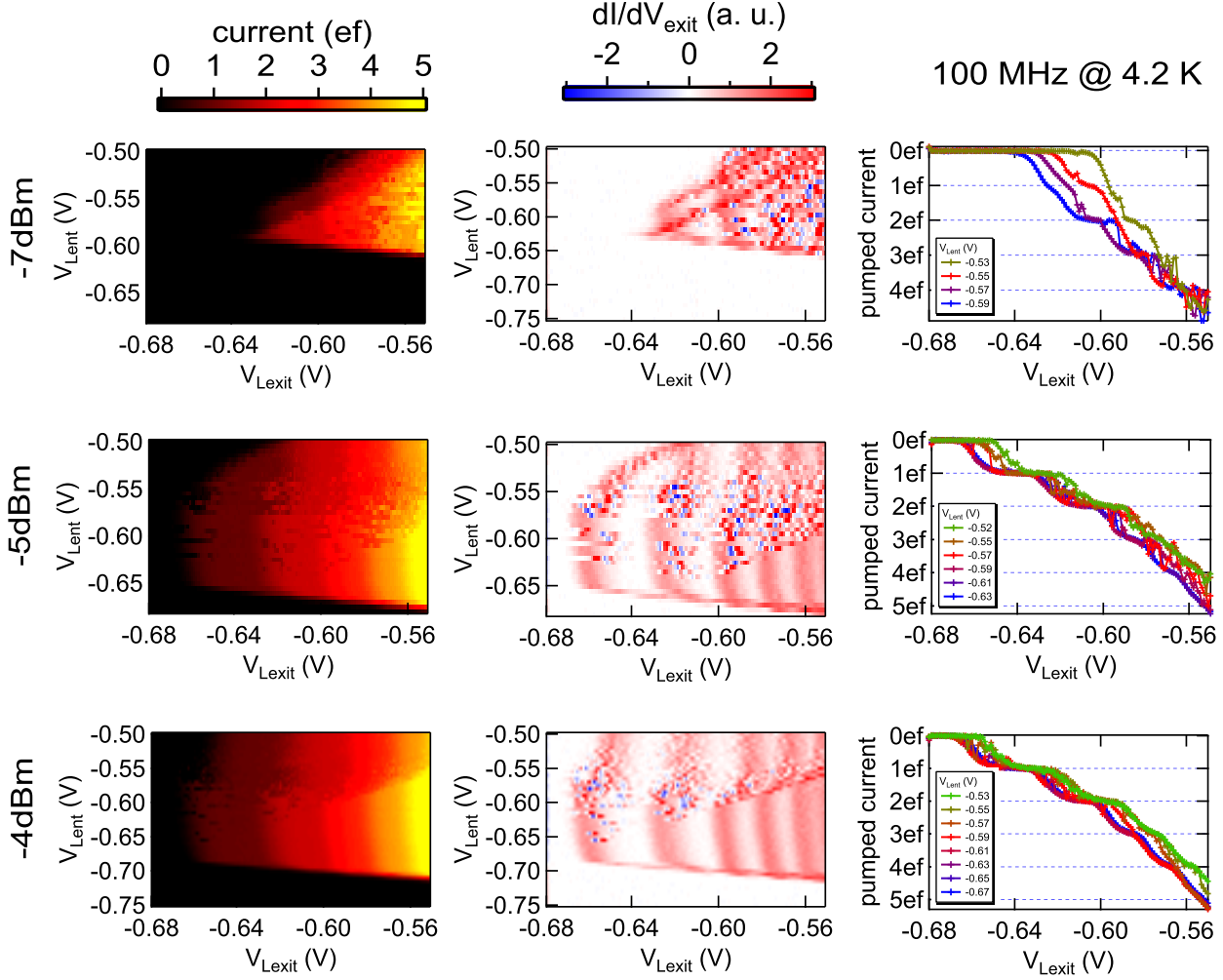

Figure 5.6: The power dependence of the pump maps (left), derivative of the pump maps (center), and line profiles (right). The current pumped by the radio frequency of 100 MHz is normalized as in Fig. 5.4.

Figure 5.7 shows the frequency dependence of the pump maps, line profiles, and derivative of pump maps at -4 dBm. These sets of data indicates that the current steps at xef ($x = 1, 2, 3,$ and 4) are obtained in the wide frequency range between 100 MHz to 400 MHz.
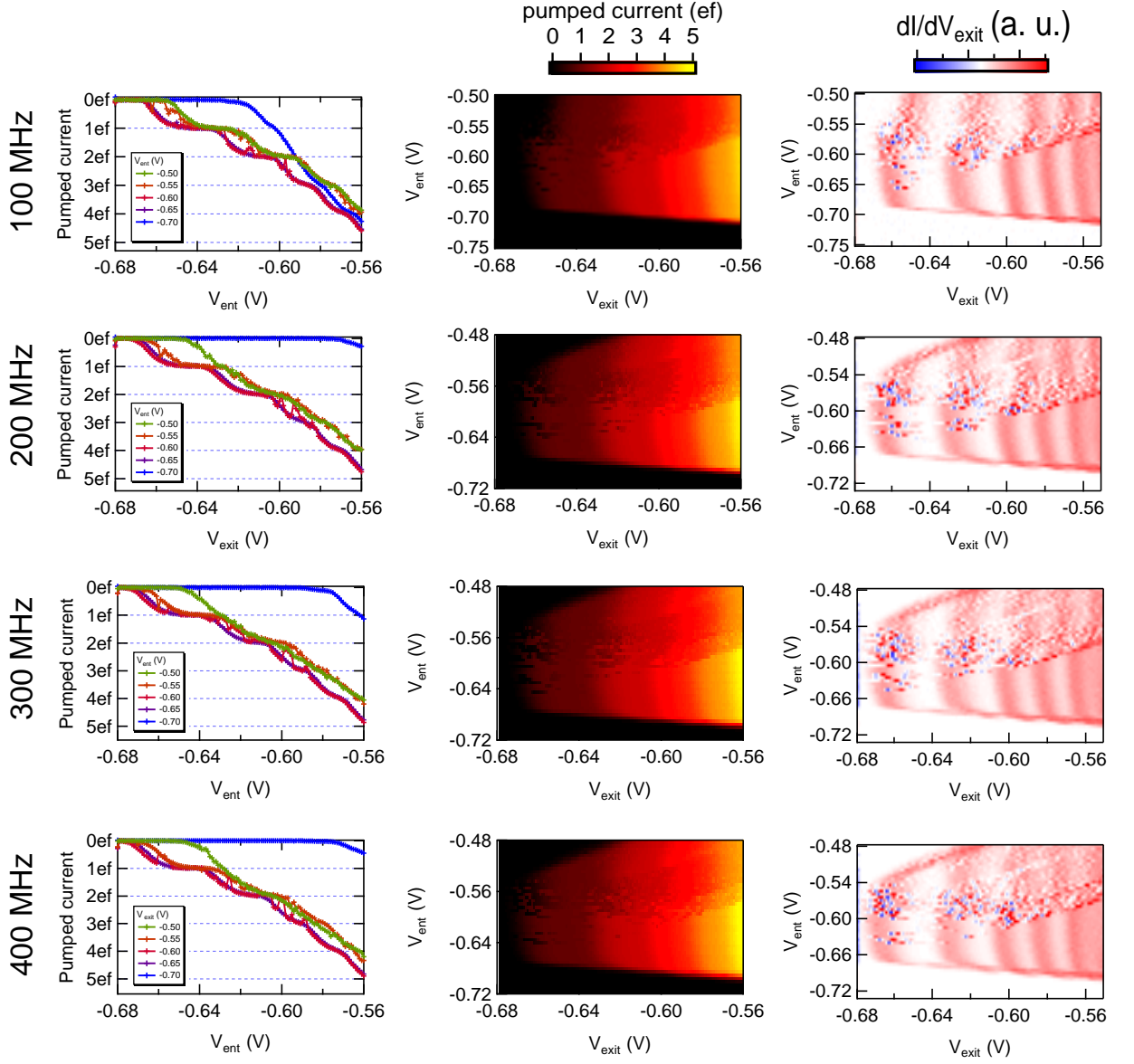
Figure 5.7: Frequency dependence of the pump map, line profile and derivative of the pump map. The current pumped by $-4\,\mathrm{dBm}$ radio frequency is normalized as in Fig. 5.4.

In all of the derivative of the pump map, the areas around the loading line are clear. At each frequency, the values of plateaus are integer multiple of ef (see line profiles of Fig. 5.7). These are clear evidence of success in pumping electron one by one.

5.4 Discussion

The correctness of plateau value is critical for pumping device, especially for application as current standard. The error of plateau value comes from (1) pumping error and (2) measurement error.

(1) The pumping error can be caused by (i) thermal excitation and (ii) loading error. (i) Thermal excitation allows the existence of extra electrons in the excited state in QD which can

lead to additional electron pumping. Thermal excitation can be suppressed by cooling down the sample and strong magnetic field because the energy difference between the discrete levels depends on applied magnetic field. (ii) Loading error is caused by the rise of the potential barrier generated by V_{ent} before loading electrons in QD. This problem is improved by slow down of operation frequency and changing waveform from a sine wave into a square wave. These techniques help the potential barrier being the low energy state for a long time and reduce the loading error rate.

(2) The measurement error can be caused by (i) the error of the resistance, (ii) the short integration time, and (iii) offset voltage of the OP amp. The measurement error is not important for us because we want to utilize pumping device as a tool to investigate physics rather than precise standard research. In this sense, noise measurement suits for evaluation of pumping device because noise measurement of the pumped current is the important tool of quantum optics with Fermion, i. e. electrons. Of course, solving these problems is important to define standard current with pumping devices.

5.5 Conclusion and perspective

To conclude, I studied the tunable barrier tunneling device in the RF regime and proved that single electron pumping is realized in wide parameter ranges.

The sample is useful to establish several techniques for studying dynamics in quantum transport. For example, spectroscopy of pumped electrons in a high magnetic field is good as the next step. In the high magnetic field, pumped electrons propagate along the edge channels due to the Landau level formation. It is unlikely for electrons in the Landau level to lose its energy because wave functions before and after transition are separated spatially. Since single electron works on-demand, pump-probe measurement is available. Time resolution depends on how precise delay control is. For instance, Tektronix AWG70001A Arbitrary Wave Form Generator has 20 ps resolution of delay control, which enables us to study dynamics with 20 ps resolution. Anti-dot formed by a potential island is a good object because electron pumped by tunable barrier tunneling device has at least 100 meV higher energy than Fermi surface. The hot electron is not useful to study quantum phenomenon caused by electrons around Fermi sea, for example, Kondo effect. The mesoscopic capacitor which excites electrons on Fermi sea suits Kondo effect. The disadvantage of the mesoscopic capacitor is the excitation one electron and one hole, which means we cannot make sure whether or not pumping device works or not with simple current measurement. The mesoscopic capacitor was measured by the acquisition of real-time measurement[87]. The technique developed by pump-probe measurement enables us to separate pumped electrons and pumped holes, which can be measured by standard current measurement. Selected electrons pumped by mesoscopic capacitor might allow measurement of real time development of Kondo effect.

5.6 Appendix

5.6.1 Current-voltage converter

Figure 5.8 shows the homemade current-voltage converter which was used to measure pumped current of the order of tens pA.

Figure 5.8: A photo of homemade current-voltage converter.

The first stage of current-voltage converter consists of OPA627au whose non-inverted input is filtered with RC low pass filter. The non-inverted input is applied 1000 times smaller voltage of applied on the BNC connector with a voltage divider. You can choose feedback resistance, $10\,\mathrm{M\Omega}$, $100\,\mathrm{k\Omega}$, and $1\,\mathrm{k\Omega}$. The second stage is an instrumentation amp made of INA118u whose inputs are connected output and the non-inverted input of OPA627au. An amplification of the instrumentation amp is defined by the resistance between two pins. You can select amplification $\times 1$, $\times 10$ and $\times 100$. So switching the connection of the OP amp and instrumentation amp changes output level.

5.6.2 Cooling down of the narrow 2DEG wire

The difficulty of narrow 2DEG is not only fabrication but also measurement. Figure 5.9 shows two terminal conductance of the exact same narrow 2DEG ($1\,\mu\mathrm{m}$ width and $20\,\mu\mathrm{m}$ length). It was measured as the device was being cooled down from the room temperature to $4.2\,\mathrm{K}$.

(a)

(b)
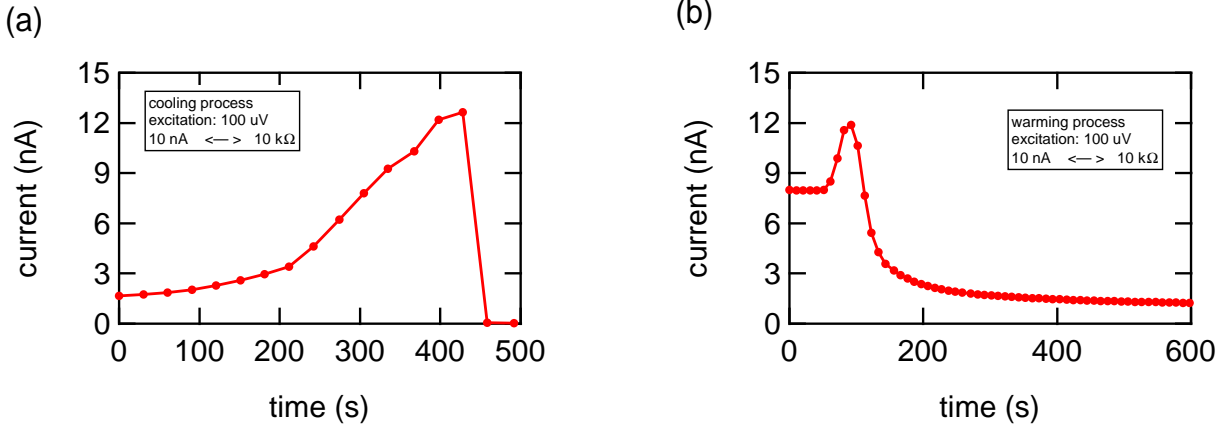
Figure 5.9: Time dependence of the conductance measurement of $1\,\mu$m width and $20\,\mu$m length 2DEG with $100\,\mu$V ~ 1 K excitation. (a) The result of the cooling process. 2DEG was killed at 420 s. (b) The result of the warming process after cooling down with all terminal grounded. Conventional temperature dependence of transport is observed.

The excitation was decided to be lower than 4.2 K $\sim 400\,\mu$eV, and $100\,\mu$V can be negligible perturbation for the sample. 2DEG was suddenly insulating while the conductance measurement of cooling (dipping into liquid helium) process (Fig. 5.9 (a)). It is unclear how the 2DEG was killed by the cooling process. After warming up to the room temperature, the sample was cooled down again with all the terminal grounded. After the sample reached at 4.2 K, all terminals were conductive. Figure 5.9 (b) shows the time dependence of the conductance after pulling the sample up from liquid helium. The peak at 100 s coming from increase of electron density and decrease of phonon scattering rate are observed. This is expected behavior in the transport of 2DEG wafer. Although the reason why 2DEG was killed is unknown, cooling the sample down with all terminal grounded prevents 2DEG from insulating.

5.6.3 Electrical grounding

In order to prevent electrostatic discharge from breaking sample, I connected ground of various lines to the earth through 1 MΩ. 1 MΩ resistance is important to discharge gradually.

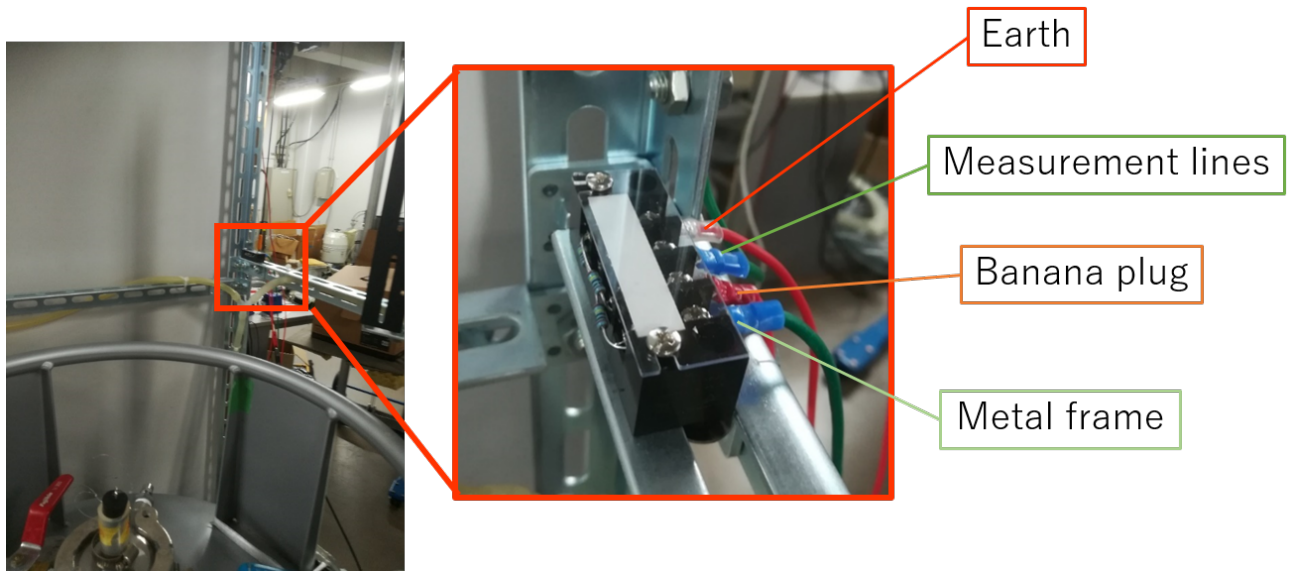Figure 5.10: The wiring of the measurement ground. Each ground lines are connected through the $1\,\mathrm{M\Omega}$ resistance.

5.6.4 Sample holder

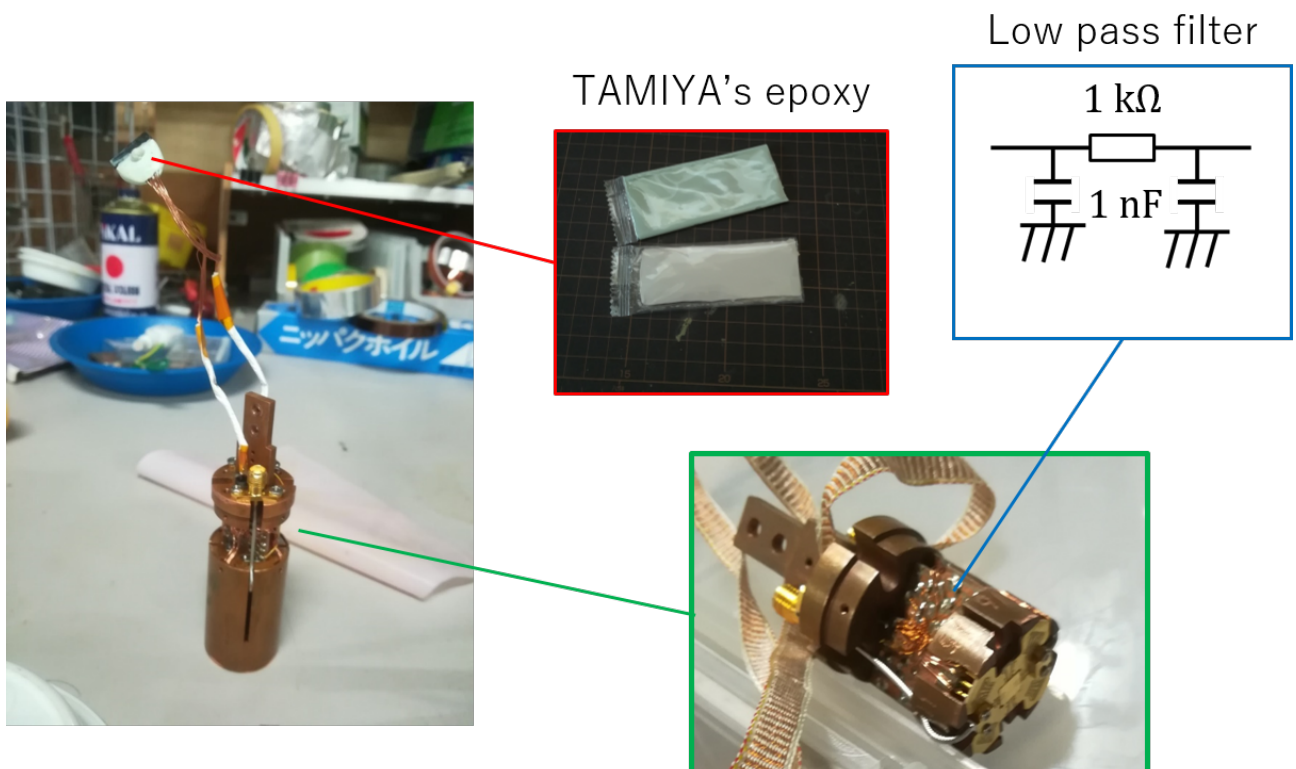Figure 5.11 shows our sample holder which has four RF lines and twenty DC lines.

Figure 5.11: Our sample holder

RF lines are connected by SMA connectors. DC lines are connected pin connectors through

the low pass filters of one $1\,\mathrm{k\Omega}$ resistor and two $1\,\mathrm{nF}$ capacitors which prevent sample breaking caused by electrostatic charge. Solder cups of pin connectors are insulated by epoxy resin provided by Tamiya Inc. It is so hard as to be handled.

Since commercial jig of SMA connector is expensive, I fabricated homemade jigs as shown in Fig. 5.12.

(a)   (b)

Jig for male connector   Jig for female connector

Figure 5.12: Homemade jigs of SMA connector. The Jigs are made of junks. (a) The Jig for male connector. (b) The Jig for female connector.

The Jigs which align the position of the inner and outer connector is made of junk connector whose inner connector is shifted to align. Poles which have a hole in center push the dielectric without scratching the connectors.

6 Conclusion

Mesocopic systems allow us to observe and control various quantum phenomenon. The purpose of this Thesis is to describe what we have done with the purpose to study dynamics in mesoscopic system with a fundamental idea of transmission and reflection of the single electron. Below, we summarize the Thesis.

6.1 Nano-fabrication and single electron pumping

Pump-probe measurement with single electron source is a powerful method to investigate electron dynamics. The fabrication of the single electron source requires etching technique of sub-micron structures in order to eliminate unexpected quantum dot. Sub-micron structure was fabricated by using photoresist exposed by electron beam. Not only fabrication techniques but also measurement techniques are established. By using metallic gates on narrow 2DEG we successfully defined single electron sources, which can be operated by radio frequency. We confirmed that the single electron source worked at several hundreds MHz in the liquid Helium temperature (4.2 K). This will serve as fundamental techniques to investigate electron dynamics with pump-probe measurement.

6.2 Single electron detection with radio frequency

We worked on new current standard based on new definition of electric current in Système International d'unités. The new definition of current standard I is defined by elementary charge e and the number of electron propagating into the conductor per unit time f as $I = ef$, which is based on single electron sources. The uncertainty of current standard is caused by the operation errors of the single electron sources, loading error, and pumping error. In order to erase such errors, we tried to feedback operation of the single electron sources. We tried single electron detection with radio frequency for feedback operation. In order to achieve our purpose, we established

- transport measurement in double quantum dot.

- single electron detection of double quantum dot by utilizing quantum point contact and quantum dot.

- single electron detection of double quantum dot by using radio frequency (around 140 MHz) reflection from quantum point contact and quantum dot.

Single electron detection with radio frequency reflection is an essential technique to establish current standard based on the new definition. Therefore this is an important step for realizing the new current standard.

6.3 Fano effect in the transport of double quantum dot

Fano effect is one of ubiquitous phenomenon caused by interference, which requires discrete level and energy continuum. We observed the Fano effect in the transport of double quantum dot. We theoretically simulated the transport in the double quantum dot with model calculation which consists of two lateral discrete levels and direct transport between leads. That reproduced the experimental result qualitatively.

We reported observation of Fano effect, coherent transport in double quantum dot, in unreported system with the support of the model calculation. That is proof of two dimensionality of the electron in the double quantum dot. Our work is the first observation of the Fano effect in double quantum dot and constitutes a clear example of the ubiquitous nature of the Fano effect in mesoscopic transport.

This study has established the fabrication and high-frequency measurement techniques for single electron source and has clarified the relevance of the coherent transport. The achievement will further promote research on the non-equilibrium region of quantum systems.

Acknowledgment

First, I want to thank my advisor Prof. Kensuke Kobayashi for accepting my belonging to his group. He taught me physics on writing documents, abstract for the conferences, budget, and, of course, this Thesis. Assistant Prof. Tomonori Arakawa and Dr. Meydi Ferrier supervised me on the experiments. I often had conversations on not only experiments but also silly talking. It was nice to stay comfortably in the student's room. Because I remind of "The Incredible Hulk", I write how he was born what I have talked with Meydi-san here. In original comics which Meydi-san read, Hulk was born due to the γ ray. In movie "The Incredible Hulk (2008)" which I watched, Hulk was born due to Super-Soldier serum which generates "Captain America". On the experiment, he taught me "localization of electrons" because his PhD work was a measurement of various characteristic length. I have really enjoyed conversation with him (of course, in English). Arakawa-san taught me measurement techniques and Physics. In the early years of my Kobayashi group life, I worked on the construction of the measurement system with him. This activity does not help to generate paper or to earn good scores, but it was good to stand by myself. His comments and idea helped me. Associate Prof. Yasuhiro Niimi brought a new wave to Kobayashi group. The new wave consist of ideas and measurement techniques. Thanks to him, my barrier to change tradition was erased. Dr. Ryosuke Yoshii helped me to understand theoretical parts of various papers and books. Prof. Kenichi Asano assisted me on the theoretical parts of Chapter 3 and gave comments when I wrote an application form to get a budget. His theoretical support on Fano effect guided me. If there were no help, I went the wrong way and lost a lot of time. I thank the secretaries Ms. Yura and Ms. Sasaki. Ms. Yura gave comments on documents for essay and entry sheet. Ms. Sasaki managed procedures to buy somethings and travel. I have not supervised the specifics. I, however, thank younger students for their patient. I hope I gave good effects on them.

My works in Chapter 3 and Chapter 4 were done in Quantum Electrical Standards group, National Metrology Institute of Japan, National Institute of Advanced Industrial Science and Technology (AIST). First, I want to thank Dr. Nobu-hisa Kaneko, the group leader when I was there, for his welcoming me. I really enjoyed staying in AIST for five months. Dr. Shuji Nakamura supervised me in AIST. He taught me how to operate all apparatus and physics in a transport of quantum dot. He also gave a lot of comments on many papers and presentations, of course, daily conversation. I want to thank him for his patient, and his funding of staying in AIST for two months. Dr. Yuma Okazaki gave me convenient stuff and comments on the experiments. I felt sometimes different culture grown in NTT. I sometimes entered into the other experimental room. I have learned many ideas different from Kobayashi group. The resistance calibration room in which Dr. Takehiko Oe work is one of them. I thank him for his patient for my intruding and daily conversation. I enjoyed climbing Mt. Tsukuba and bathhouse with him and Nakamura-san. I want to thank the other members in A227, for example, secretary Ms. Oyama, and the members of Dr. Chiharu Urano group who often meet, Urano-san, Iida-san, Misawa-san, and Saito-san.

The measurement techniques in Chapter 5 is educated in National Physical Laboratory (NPL), England. First, I say thank to Dr. Masaya Kataoka the group leader of quantum detec-

Various events including something bad and good on my doctor life construct my personality. It is good to be doctor course student if you have support on funding.

References

[1] S. Norimoto, S. Nakamura, Y. Okazaki, T. Arakawa, K. Asano, K. Onomitsu, K. Kobayashi, and N.-h. Kaneko, Phys. Rev. B, **97**, 195313 (2018).

[2] S. Datta, Electronic Transport in Mesoscopic Systems (Cambridge University Press, 1997) ISBN 978-0-521-59943-6.

[3] E. Akkermans and G. Montambaux, Mesoscopic Physics of Electrons and Photons, 1st ed. (Cambridge University Press, 2007) ISBN 978-0-51-34947-5.

[4] R. A. Webb, S. Washburn, C. P. Umbach, and R. B. Laibowitz, Phys. Rev. Lett., **54**, 2696 (1985).

[5] Y. Aharonov and D. Bohm, Phys. Rev., **115**, 485 (1959).

[6] S. M. Cronenwett, T. H. Oosterkamp, and L. P. Kouwenhoven, Science, **281**, 540 (1998), ISSN 1095-9203, arXiv:9804211 [cond-mat] .

[7] D. Goldhaber-Gordon, H. Shtrikman, D. Mahalu, D. Abusch-Magder, U. Meirav, and M. A. Kastner, "bibfield journal "bibinfo journal Nature," "textbf "bibinfo volume 391," "bibinfo pages 156 ("bibinfo year 1998).

[8] W. G. van der Wiel, S. De Franceschi, T. Fujisawa, J. M. Elzerman, S. Tarucha, and L. P. Kouwenhoven, Science, **289**, 2105 (2000).

[9] J. Kondo, Progress of Theoretical Physics, **32**, 37 (1964), ISSN 0033-068X.

[10] W. J. de Haas, J. de Boer, and G. J. van den Berg, Physica, **1**, 1115 (1934), ISSN 0031-8914.

[11] K. v. Klitzing, G. Dorda, and M. Pepper, Phys. Rev. Lett., **45**, 494 (1980).

[12] "National Institute of Standards and Technology NIST: https://www.nist.gov/," .

[13] "National Metrology Institute of Japan: https://www.nmij.jp/," .

[14] "Bureau International des Poids et Mesures, On the revision of the SI: https://www.bipm.org/en/measurement-units/rev-si/," .

[15] Bureau International des Poids et Mesures, The International System of Units (SI Units), 8th ed. (2006) ISBN 978-0-8493-8295-6, arXiv:arXiv:1011.1669v3 .

[16] L. Fricke, M. Wulf, B. Kaestner, F. Hohls, P. Mirovsky, B. Mackrodt, R. Dolata, T. Weimann, K. Pierz, U. Siegner, and H. W. Schumacher, Phys. Rev. Lett., **112**, 226803 (2014).

[17] G. Yamahata, K. Nishiguchi, and A. Fujiwara, Nature communications, **5**, 5038 (2014), ISSN 2041-1723.

[18] N.-h. Kaneko, S. Nakamura, and Y. Okazaki, Measurement Science and Technology, **27**, 032001 (2016).

[19] F. Stein, H. Scherer, T. Gerster, R. Behr, M. Götz, E. Pesel, C. Leicht, N. Ubbelohde, T. Weimann, K. Pierz, H. W. Schumacher, and F. Hohls, Metrologia, **54**, S1 (2017).

[20] S. P. Giblin, Metrologia, **56**, 015014 (2019).

[21] E. Bocquillon, V. Freulon, J.-M. Berroir, P. Degiovanni, B. Plaçais, A. Cavanna, Y. Jin, and G. Fève, Science, **339**, 1054 (2013), ISSN 1095-9203.

[22] S.-i. Tomonaga, Progress of Theoretical Physics, **5**, 544 (1950).

[23] J. M. Luttinger, Journal of Mathematical Physics, **4**, 1154 (1963).

[24] V. Freulon, a. Marguerite, J.-M. Berroir, B. Plaçais, a. Cavanna, Y. Jin, and G. Fève, Nature Communications, **6**, 6854 (2015), ISSN 2041-1723.

[25] J. D. Fletcher, P. See, H. Howe, M. Pepper, S. P. Giblin, J. P. Griffiths, G. a. C. Jones, I. Farrer, D. a. Ritchie, T. J. B. M. Janssen, and M. Kataoka, Physical Review Letters, **111**, 216807 (2013), ISSN 00319007, arXiv:arXiv:1212.4981v2 .

[26] M. Kataoka, N. Johnson, C. Emary, P. See, J. P. Griffiths, G. A. C. Jones, I. Farrer, D. A. Ritchie, M. Pepper, and T. J. B. M. Janssen, Phys. Rev. Lett., **116**, 126803 (2016).

[27] M. J. Madou, Fundamentals of Microfabrication and Nanotechnology, 2nd ed. (CRC Press., 2002).

[28] S. M. Sze and M.-K. Lee, Semiconductor Devices: Physics and Technology, 3rd ed. (Wiley, 2012).

[29] S. Norimoto, "Web page of Shota Norimoto, https://sites.google.com/site/shotanorimoto/photo," .

[30] ALLRESIST, "Resist-Wiki http://www.allresist.com/resist-wiki/," .

[31] C. A. Bozada, J. L. Ebel, D. C. Look, and J. P. Barrette, **143**, 3652 (1996).

[32] L. P. Kouwenhoven, C. M. Marcus, P. L. Mceuen, S. Tarucha, R. M. Westervelt, and N. S. Wingreen, in Electron transport in quantum dots (Springer, Netherlands, 1997) pp. 105–214, ISBN 978-90-481-4906-3, arXiv:9612126 [cond-mat] .

[33] S. Tarucha, D. G. Austing, T. Honda, R. J. van der Hage, and L. P. Kouwenhoven, Phys. Rev. Lett., **77**, 3613 (1996).

[34] W. G. van der Wiel, S. De Franceschi, J. M. Elzerman, T. Fujisawa, S. Tarucha, and L. P. Kouwenhoven, Reviews of Modern Physics, **75**, 1 (2003).

[35] D. Loss and D. P. DiVincenzo, Phys. Rev. A, **57**, 120 (1998).

[36] G. Breit and E. Wigner, Phys. Rev., **49**, 519 (1936).

[37] A. Yacoby, M. Heiblum, D. Mahalu, and H. Shtrikman, Phys. Rev. Lett., **74**, 4047 (1995).

[38] S. Katsumoto and A. Endo, J. Phys. Soc. Jpn., **65**, 4086 (1996).

[39] R. Schuster, E. Buks, M. Heiblum, D. Mahalu, V. Umansky, and H. Shtrikman, Nature, **385**, 417 (1997), ISSN 00280836.

[40] M. Avinun-Kalish, M. Heiblum, O. Zarchin, D. Mahalu, and V. Umansky, Nature, **436**, 529 (2005).

[41] S. Takada, C. Bäuerle, M. Yamamoto, K. Watanabe, S. Hermelin, T. Meunier, A. Alex, A. Weichselbaum, J. von Delft, A. Ludwig, A. D. Wieck, and S. Tarucha, Phys. Rev. Lett., **113**, 126601 (2014).

[42] H. Edlbauer, S. Takada, G. Roussely, M. Yamamoto, S. Tarucha, A. Ludwig, A. D. Wieck, T. Meunier, and C. Bäuerle, Nature Communications, **8**, 1710 (2017), ISSN 2041-1723.

[43] K. Kobayashi, H. Aikawa, S. Katsumoto, and Y. Iye, Physical review letters, **88**, 256806 (2002), ISSN 0031-9007, arXiv:0202006 [cond-mat] .

[44] K. Kobayashi, H. Aikawa, S. Katsumoto, and Y. Iye, Phys. Rev. B, **68**, 235304 (2003).

[45] U. Fano, Physical Review, **124**, 1866 (1961), ISSN 0031899X, arXiv:0611602 [cond-mat] .

[46] A. E. Miroshnichenko, S. Flach, and Y. S. Kivshar, Reviews of Modern Physics, **82**, 2257 (2010).

[47] H. Beutler, Zeitschrift für Physik A, **93**, 177 (1935), ISSN 14346001.

[48] R. K. Adair, C. K. Bockelman, and R. E. Peterson, Phys. Rev., **76**, 308 (1943).

[49] F. Cerdeira, T. A. Fjeldly, and M. Cardona, Phys. Rev. B, **8**, 4734 (1973).

[50] L. Bryja, A. Wójs, K. Ryczko, K. Wójcik, J. Misiewicz, M. Potemski, D. Reuter, and A. Wieck, International Journal of Modern Physics B, **21**, 1429 (2007).

[51] V. Madhavan, W. Chen, T. Jamneala, M. F. Crommie, and N. S. Wingreen, Science, **280**, 567 (1998).

[52] J. Li, W.-d. Schneider, R. Berndt, and B. Delley, Phys. Rev. Lett., **80**, 2893 (1998).

[53] J. Göres, D. Goldhaber-Gordon, S. Heemeyer, and M. A. Kastner, Phys. Rev. B, **62**, 2188 (2000).

[54] I. G. Zacharia, D. Goldhaber-Gordon, G. Granger, M. A. Kastner, Y. B. Khavin, H. Shtrikman, D. Mahalu, and U. Meirav, Phys. Rev. B, **64**, 155311 (2001).

[55] H. Aikawa, K. Kkobayashi, A. Sano, S. Katsumoto, and Y. Iye, Journal of the Physical Society of Japan, **73**, 3235 (2004).

[56] C. Fühner, U. F. Keyser, R. J. Haug, D. Reuter, and A. D. Wieck, Physica Status Solidi (C), **0**, 1305 (2003), ISSN 1610-1634.

[57] K. Kobayashi, H. Aikawa, A. Sano, S. Katsumoto, and Y. Iye, Phys. Rev. B, **70**, 035319 (2004).

[58] A. C. Johnson, C. M. Marcus, M. P. Hanson, and A. C. Gossard, Phys. Lett. Lett., **93**, 106803 (2004).

[59] M. Sato, H. Aikawa, K. Kobayashi, S. Katsumoto, and Y. Iye, Phys. Rev. Lett., **95**, 066801 (2005).

[60] S. Sasaki, H. Tamura, T. Akazaki, and T. Fujisawa, Phys. Rev. Lett., **103**, 266806 (2009).

[61] H. Aikawa, K. Kobayashi, A. Sano, S. Katsumoto, and Y. Iye, Phys. Rev. Lett., **92**, 176802 (2004).

[62] S. Takada, M. Yamamoto, C. Bäuerle, A. Ludwig, A. D. Wieck, and S. Tarucha, Phys. Rev. B, **95**, 241301 (2017).

[63] J. U. Nöckel and A. D. Stone, Phys. Rev. B, **50**, 17415 (1994).

[64] A. A. Clerk, P. W. Brouwer, and V. Ambegaokar, Phys. Rev. Lett., **87**, 186801 (2001).

[65] J. Schmid, J. Weis, K. Eberl, and K. v. Klitzing, Physica B: Condensed Matter, **256-258**, 182 (1998), ISSN 09214526.

[66] A. W. Rushforth, C. G. Smith, I. Farrer, D. A. Ritchie, G. A. C. Jones, D. Anderson, and M. Pepper, Phys. Rev. B, **73**, 081305 (2006).

[67] C. Livermore, C. H. Crouch, R. M. Westerwelt, K. L. Champman, and A. C. Gossart, Science, **274**, 1332 (1996).

[68] T. Nakanishi, K. Terakura, and T. Ando, Phys. Rev. B, **69**, 115307 (2004).

[69] H.-W. Lee, Phys. Rev. Lett., **82**, 2358 (1999).

[70] P. G. Silvestrov and Y. Imry, Phys. Rev. Lett., **85**, 2565 (2000).

[71] A. L. Yeyati and M. Büttiker, Phys. Rev. B, **62**, 7307 (2000).

[72] M. L. Ladrón de Guevara, F. Claro, and P. A. Orellana, Phys. Rev. B, **67**, 195335 (2003).

[73] L. P. Kouwenhoven, A. T. Johnson, N. C. van der Vaart, C. J. P. M. Harmans, and C. T. Foxon, Physical Review Letters, **67**, 1626 (1991), ISSN 0031-9007.

[74] J. P. Pekola, J. J. Vartiainen, M. Möttönen, O.-P. Saira, M. Meschke, and D. V. Averin, Nature Physics, **4**, 120 (2008).

[75] "National Metrology Institute of Japan, National Institute of Advanced Indastrial Science and Technology: https://www.nmij.jp/english/org/lab/1/," .

[76] M. Field, C. G. Smith, M. Pepper, D. A. Ritchie, J. E. F. Frost, G. A. C. Jones, and D. G. Hasko, Phys. Rev. Lett., **70**, 1311 (1993), ISSN 1550-5154.

[77] M. Wulf, Phys. Rev. B, **87**, 035312 (2013).

[78] R. J. Schoelkopf, P. Wahlgren, A. A. Kozhevnikov, P. Delsing, and D. E. Prober, Science, **280**, 1238 (1998).

[79] T. Otsuka, S. Amaha, T. Nakajima, M. R. Delbecq, J. Yoneda, K. Takeda, R. Sugawara, G. Allison, A. Ludwig, A. D. Wieck, and S. Tarucha, Scientific reports, **5**, 14616 (2015).

[80] N. Ares, F. J. Schupp, A. Mavalankar, G. Rogers, J. Griffiths, G. A. Jones, I. Farrer, D. A. Ritchie, C. G. Smith, A. Cottet, G. A. D. Briggs, and E. A. Laird, Physical Review Applied, **5**, 034011 (2016), ISSN 23317019, arXiv:1510.06944 .

[81] T. Frey, P. J. Leek, M. Beck, A. Blais, T. Ihn, K. Ensslin, and A. Wallraff, Phys. Rev. Lett., **108**, 046807 (2012).

[82] K. D. Petersson, L. W. McFaul, M. D. Schroer, M. Jung, J. M. Taylor, A. A. Houck, and J. R. Petta, Nature, **490**, 380 (2012), ISSN 00280836, arXiv:1205.6767 .

[83] K. Chida, S. Desai, K. Nishiguchi, and A. Fujiwara, Nature Communications, **8**, 15301 (2017).

[84] M. W. Keller, J. M. Martinis, N. M. Zimmerman, and A. H. Steinbach, Applied Physics Letters, **69**, 1804 (1996).

[85] V. I. Talyanskii, J. M. Shilton, M. Pepper, C. G. Smith, C. J. B. Ford, E. H. Linfield, D. A. Ritchie, and G. A. C. Jones, Phys. Rev. B, **56**, 15180 (1997).

[86] M. D. Blumenthal, B. Kaestner, L. Li, S. Giblin, T. J. B. M. Janssen, M. Pepper, D. Anderson, G. Jones, and D. A. Ritchie, Nature Physics, **3**, 343 (2007).

[87] G. Fève, A. Mahé, J.-M. Berroir, T. Kontos, B. Plaçais, D. C. Glattli, A. Cavanna, B. Etienne, and Y. Jin, Science, **316**, 1169 (2007), ISSN 1095-9203.

[88] G. Haack, M. Moskalets, J. Splettstoesser, and M. Büttiker, Physical Review B, **84**, 2 (2011), ISSN 10980121, arXiv:1103.2260 .

[89] S. Hermelin, S. Takada, M. Yamamoto, S. Tarucha, A. D. Wieck, L. Saminadayar, C. Bäuerle, and T. Meunier, Nature, **477**, 435 (2011), ISSN 1476-4687.

[90] J. Dubois, T. Jullien, F. Portier, P. Roche, a. Cavanna, Y. Jin, W. Wegscheider, P. Roulleau, and D. C. Glattli, Nature, **502**, 659 (2013), ISSN 1476-4687.

[91] M. Kataoka, J. D. Fletcher, P. See, S. P. Giblin, T. J. B. M. Janssen, J. P. Griffiths, G. a. C. Jones, I. Farrer, and D. a. Ritchie, Physical Review Letters, **106**, 126801 (2011), ISSN 00319007.